

**EFFECT OF THINLY-STRATIFIED SANDSTONE ON
TUNNEL ROOF STABILITY**



Surasak Chanpen

**A Thesis Submitted in Partial Fulfillment of the Requirements for the
Degree of Master of Engineering in Civil Transportation and
Geo-resources Engineering
Suranaree University of Technology
Academic Year 2017**

ผลกระทบของชั้นหินทรายบางต่อเสถียรภาพของหลังคาอุโมงค์



นายสุรศักดิ์ จันทร์เพ็ญ

วิทยานิพนธ์นี้เป็นส่วนหนึ่งของการศึกษาตามหลักสูตรปริญญาวิศวกรรมศาสตรมหาบัณฑิต

สาขาวิชาวิศวกรรมโยธา ขนส่ง และทรัพยากรธรณี

มหาวิทยาลัยเทคโนโลยีสุรนารี

ปีการศึกษา 2560

EFFECT OF THINLY-STRATIFIED SANDSTONE ON TUNNEL ROOF STABILITY

Suranaree University of Technology has approved this thesis submitted in partial fulfillment of the requirements for a Master's Degree.

Thesis Examining Committee



(Asst. Prof. Dr. Decho Phueakphum)

Chairperson



(Prof. Dr. Kittitep Fuenkajorn)

Member (Thesis Advisor)



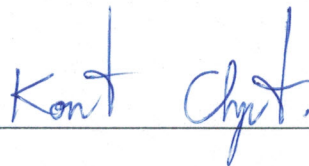
(Assoc. Prof. Dr. Pomkasem Jongpradist)

Member



(Prof. Dr. Santi Maensiri)

Vice Rector for Academic Affairs
and Internationalization



(Assoc. Prof. Flt. Lt. Dr. Kontorn Chamniprasart)

Dean of Institute of Engineering

สุรศักดิ์ จันทร์เพ็ญ : ผลกระทบของชั้นหินทรายบางต่อเสถียรภาพของหลังคาอุโมงค์
(EFFECT OF THINLY-STRATIFIED SANDSTONE ON TUNNEL ROOF
STABILITY) อาจารย์ที่ปรึกษา : ศาสตราจารย์ ดร.กิตติเทพ เพ็ญขจร, 84 หน้า.

วัตถุประสงค์ของงานวิจัยนี้คือ เพื่อศึกษาผลกระทบของชั้นหินทรายบางต่อเสถียรภาพของหลังคาอุโมงค์ การทดสอบแรงดึงแบบกดสามจุดได้ดำเนินการบนตัวอย่างหินรูปทรงสี่เหลี่ยมผืนผ้า (50×50×200 มิลลิเมตร) ของหินทรายชุดภูพาน แผ่นหินทรายบางถูกสร้างขึ้นด้วยการใช้เลื่อยตัดและการให้แรงกดตามแนวยาวของตัวอย่างเพื่อทำให้เกิดรอยแตกแบบคิง อัตรากาให้แรงดึงต่อตัวอย่างหินบริเวณตรงกลางของรอยแตกแบบคิงผันแปรจาก 0.001 ถึง 1 เมกะปาสคาลต่อหน้าที่ความเค้นยึดติดและแรงเสียดทานภายในของตัวอย่างผิวเรียบจากการทดสอบกำลังรับแรงเฉือนมีค่าเท่ากับ 0.13 เมกะปาสคาล และ 25 องศา สำหรับตัวอย่างผิวเรียบ-ลิ้น มีค่าเท่ากับ 0.09 เมกะปาสคาล และ 24 องศา กำลังรับแรงดึงสูงสุดและสัมประสิทธิ์ความยืดหยุ่นที่ตรวจวัดบริเวณรอยแตกแบบคิงมีค่าเพิ่มขึ้นตามอัตรากาให้แรงดึง และไม่ขึ้นกับจำนวนชั้นของแผ่นหินทราย โดยเฉพาะอย่างยิ่งเมื่อจำนวนชั้นของแผ่นหินทรายน้อยกว่า 3 ชั้น ค่าการแอนตัวมีค่าสูงขึ้นเมื่อตัวอย่างหินมีความหนาของแผ่นหินทรายบาง ผลจากการจำลองเชิงตัวเลขโดยใช้โปรแกรม UDEC ระบุว่า ค่ากำลังรับแรงดึงและค่าสัมประสิทธิ์ความยืดหยุ่นไม่ขึ้นกับความเค้นยึดติดและแรงเสียดทานระหว่างชั้นแผ่นหิน ความแกร่งของรอยแตกแบบเลื่อน (K_0) เป็นปัจจัยหลักในการบ่งบอกถึงความแข็ง ความแกร่ง และการแอนตัวของตัวอย่าง ซึ่งเป็นจริงทุกกรณีแม้จะมีจำนวนชั้นที่แตกต่างกัน ผลกระทบของความแกร่งของรอยแตกแบบเลื่อนไม่มีนัยสำคัญเมื่อมีค่าต่ำกว่า 100 เมกะปาสคาลต่อเมตร เมื่อความแกร่งของรอยแตกแบบเลื่อนมีค่ามากกว่า 5,000 เมกะปาสคาลต่อเมตร ค่าความแข็งของตัวอย่างหินจะมีค่าใกล้เคียงตัวอย่างหินที่ไม่มีรอยแตกถึงแม้ตัวอย่างนั้นจะมีรอยแตกก็ตาม ความสัมพันธ์ระหว่างกาการแอนตัวของตัวอย่างและความเครียดดึงได้ถูกพัฒนาขึ้น ค่าความเค้นและความเครียดดึงสามารถนำมาใช้คำนวณพลังงานความเครียดและนำมาเทียบกับเกณฑ์การแตกของพลังงานงานความเครียด เกณฑ์การแตกของพลังงานความเครียดสามารถนำมาใช้ประเมินเสถียรภาพของชั้นหินทรายบางบริเวณหลังคาในสภาวะจริงภายใต้สมมติฐานว่าพลังงานความเครียดสูงสุดที่เกิดขึ้นที่จุดแตกจะต้องไม่ขึ้นกับลักษณะการรับแรง สลักเกลียวอาจนำมาติดตั้งเพื่อเพิ่มอัตราส่วนความหนาต่อความกว้างของอุโมงค์ ซึ่งวิธีนี้จะเป็นการเพิ่มเสถียรภาพของหลังคา

สาขาวิชา เทคโนโลยีธรณี
ปีการศึกษา 2560

ลายมือชื่อนักศึกษา S. Chanpen
ลายมือชื่ออาจารย์ที่ปรึกษา K. Sangsorn

SURASAK CHANPEN : EFFECT OF THINLY-STRATIFIED
SANDSTONE ON TUNNEL ROOF STABILITY. THESIS ADVISOR :
PROF. KITTITEP FUENKAJORN, Ph.D., P.E., 84 PP.

BENDING TEST/ LOADING RATE/ TENSILE STRENGTH/ TENSILE STIFFNESS

The objective of this study is to determine the effect of thinly-stratified sandstone on the roof stability of tunnels. Three-point bending tests have been performed on prismatic specimens (50×50×200 mm) prepared from Phu Phan sandstone. The sandstone beds are artificially made by saw-cutting and by line-loading to induce tensile fracture. The loading rates are varied to obtain the induced tensile stresses at the crack initiation point from 0.001 to 1.0 MPa per minute. The cohesion and basic friction angle of the smooth surface obtained from the direct shear testing are 0.13 MPa and 25°, the smooth-slip surface are 0.09 MPa and 24°. The tensile strengths and elastic moduli measured at the tensile crack initiation point increase with the loading rate, and are insensitive to the number of rock layers, particularly when the number of layer is below three. Larger deflections are obtained for the specimens comprising thinner layers. Results from numerical simulations using UDEC suggest that the specimen tensile strengths and elastic moduli are independent of the cohesion and friction angle between the rock layers. The joint shear stiffness (K_s) is however the main factor governing the strength, stiffness and deflection of the specimens. This holds true for all specimens even with different numbers of rock layers. The K_s effects become insignificant when its values are below 100 MPa/m. When K_s exceeds 5,000 MPa/m, the strengths of the specimens approach that of the intact specimen regardless the number of layers. The relationship between

the rock beam deflection and the induced tensile strain is developed. The induced tensile stresses and strains are used to develop the strain energy to compare with the energy strength criterion. The energy strength criterion can be used to assess the actual stratified roof stability based on an assumption that the induced maximum strain energy at the crack initiation point is independent of the loading configurations. Rock bolts may be installed to increase the thickness-to-span length, and hence increases the stability of the roof beams.



School of Geotechnology

Academic Year 2017

Student's Signature S. Chanpen

Advisor's Signature V. Sornjan

ACKNOWLEDGMENTS

I wish to acknowledge the funding supported by Suranaree University of Technology (SUT). I would like to express my sincere thanks to Prof. Dr. Kittitep Fuenkajorn for his valuable guidance and efficient supervision. I appreciate his strong support, encouragement, suggestions and comments during the research period. My heartiness thanks to Assoc. Prof. Dr. Pornkasem Jongpradist, Asst. Prof. Dr. Decho Phueakphum, and Asst. Prof. Dr. Prachya Tepnarong and Dr. Kiattisak Artkhonghan for their constructive advice, valuable suggestions and comments on my research works as thesis committee members. Grateful thanks are given to all staffs of Geomechanics Research Unit, Institute of Engineering who supported my work.

Finally, I would like to thank beloved parents for their love, support and encouragement.

Surasak Chanpen

มหาวิทยาลัยเทคโนโลยีสุรนารี

TABLE OF CONTENTS

	Page
ABSTRACT (THAI).....	I
ABSTRACT (ENGLISH).....	II
ACKNOWLEDGEMENTS.....	IV
TABLE OF CONTENTS.....	V
LIST OF TABLES.....	IX
LIST OF FIGURES.....	X
SYMBOLS AND ABBREVIATIONS.....	XIV
CHAPTER	
I INTRODUCTION.....	1
1.1 Background and rationale.....	1
1.2 Research objectives.....	1
1.3 Scope and limitations.....	2
1.4 Research methodology.....	2
1.4.1 Literature review.....	2
1.4.2 Sample preparation.....	3
1.4.3 Laboratory testing.....	4
1.4.4 Analysis of test results.....	4
1.4.5 Potential applications.....	5
1.4.6 Discussions and conclusions.....	5

TABLE OF CONTENTS (Continued)

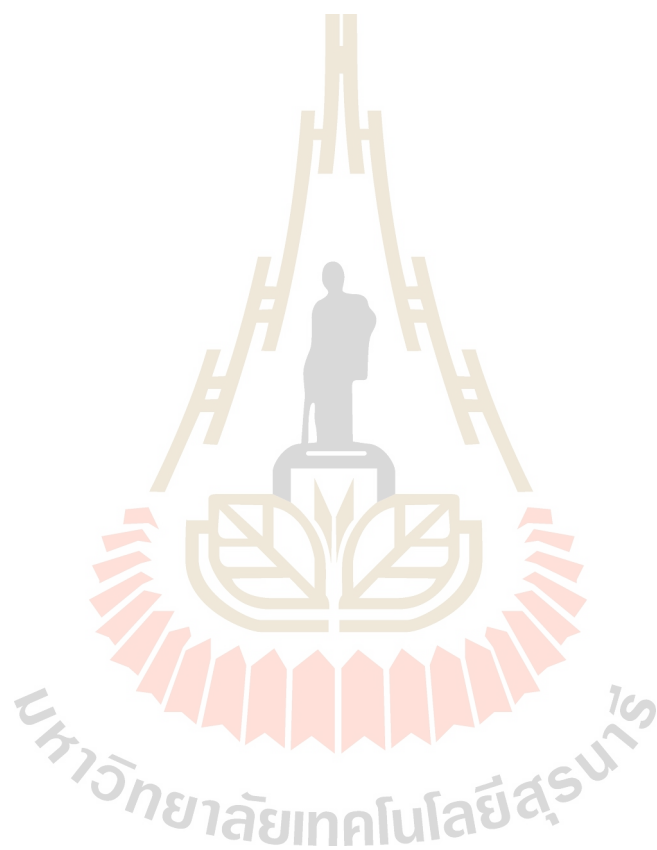
	Page
1.4.7 Thesis writing.....	5
1.5 Thesis content.....	5
II LITERATUREREVIEW.....	7
2.1 Introduction.....	7
2.2 Three-point bending test.....	7
2.3 Four-point bending test.....	8
2.4 Biaxial flexure tensile strength test.....	10
2.5 Stress gradient effect.....	12
2.6 Research on bending test.....	15
2.7 Roof strata stability analysis.....	21
III SAMPLE PREPARETION.....	26
3.1 Introduction.....	26
3.2 Sample preparation.....	26
3.2.1 Direct shear test.....	26
3.2.2 Three-point bending test.....	26
3.2.3 Strain gage installation.....	28
IV LABORATORY TESTING AND RESULTS.....	30
4.1 Introduction.....	30
4.2 Direct shear tests.....	30
4.3 Three-point bending test.....	31
4.4 Test results.....	33

TABLE OF CONTENTS (Continued)

	Page
4.4.1 Direct shear test results.....	33
4.4.2 Three point bending test results.....	35
V ANALYSIS OF TEST RESULTS.....	44
5.1 Introduction.....	44
5.2 Tensile strength criterion.....	44
5.3 Tensile elastic modulus.....	49
5.4 Strain energy density criterion.....	52
5.5 Numerical analysis.....	57
5.5.1 Rock properties for computer modeling.....	57
5.5.2 Numerical Analysis of t/L ratios effects under different surface conditions.....	58
5.5.3 Modelling results.....	64
VI POTENTIAL APPLICATIONS.....	71
6.1 Introduction.....	71
6.2 Deflection vs tensile strain.....	71
6.3 Distortional strain energy density vs mean strain energy.....	76
VII DISCUSSIONS AND CONCLUSIONS.....	81
7.1 Discussions.....	81
7.2 Conclusions.....	82
7.3 Recommendations for future studies.....	84

TABLE OF CONTENTS (Continued)

	Page
REFERENCES.....	85
BIOGRAPHY.....	90



LIST OF TABLES

Table		Page
3.1	Rock sample dimensions with various t/L ratios.....	28
4.1	Summary of test results of smooth surface and smooth-slip surface.....	35
4.2	Some post-test specimens from three point bending testing.....	37
4.3	Test results of three-point bending test on intact rock (t/L=0.25) and tension- induced fractures (t/L=0.13).....	42
4.4	Test results of three-point bending test on smooth and smooth-slip surface....	43
5.1	Empirical constants A and B.....	51
5.2	Elastic moduli, loading rate and t/L ratios for different friction conditions....	54
5.3	Tensile strengths, maximum strains and total strain energy density for all specimens.....	55
5.3	Tensile strengths and maximum strains, total strain energy density for all specimens (cont.).....	56
5.4	Summary of the basic joint properties.....	58
5.5	Summary of model results for joint shear stiffness conditions.....	69
5.5	Summary of model results for joint shear stiffness conditions (cont.).....	70
6.1	Summary of the principal stress deviations and principal strain deviations....	78
6.2	Summary of the distortional and mean strain energy density at failure.....	80

LIST OF FIGURES

Figure	Page
1.1 Research methodology.....	3
2.1 Schematic of a suitable apparatus for flexure test by center-point loading method (ASTM (C293–02)).....	8
2.2 Loading diagram (ASTM (D6272–10)).....	10
2.3 Biaxial flexural tensile strength tests arrangement (Phueakphum et al., 2013).....	11
2.4 Elastic beam with (a) fixed ends and (b) simple (pin) supports (Snyder, 1983).....	19
2.5 Variation of the stresses along the height of a beam (Exadaktylos et al., 2001).....	20
2.6 The relationship between maximum horizontal compressive stress in beam and beam thickness for various roof span values (B). The case of they are (B =7 m) shown using bold line (Hatzor and Benary, 1998).....	23
3.1 Examples of smooth surface prepared in Phu Phan sandstone.....	27
3.2 Sample specimens for three point bending test.....	27
3.3 Joint roughness of rock samples (JRC = 10).....	29
3.4 Examples of prismatic specimens with strain gage position.....	29
4.1 The direct shear machine model EL-77-1030 for direct shear tests.....	31

LIST OF FIGURES (Continued)

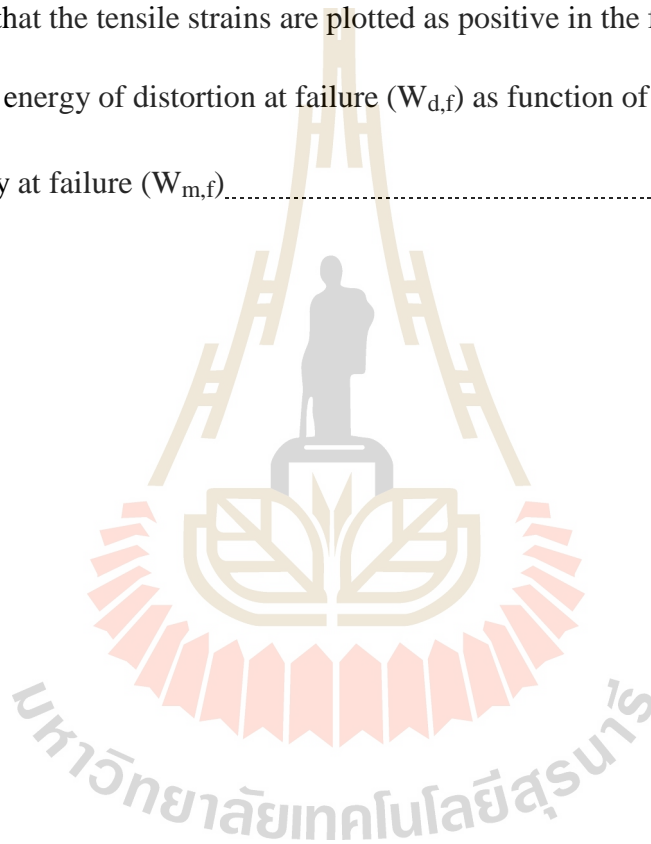
Figure	Page
4.2	Schematic of a three-point beam bending test method (ASTM (C293–02)).....32
4.3	Three-point bending test arrangement.....32
4.4	Shear stresses of Phu Phan sandstone as a function of shear displacement for smooth surface and smooth-slip surface.....33
4.5	Peak shear stresses as a function of normal stress.....34
4.6	Tensile stress-strain curves for loading rate of 1 MPa/min.....38
4.7	Tensile stress-strain curves for loading rate of 0.1 MPa/min.....38
4.8	Tensile stress-strain curves for loading rate of 0.01 MPa/min.....39
4.9	Tensile stress-strain curves for loading rate of 0.001 MPa/min.....39
4.10	Failure most occur in the lowest slab on three-point bending test.....40
4.11	Tensile stress-deflection curves for loading rate of 1 MPa/min.....40
4.12	Tensile stress-deflection curves for loading rate of 0.1 MPa/min.....41
4.13	Tensile stress-deflection curves for loading rate of 0.01 MPa/min.....41
4.14	Tensile stress-deflection curves for loading rate of 0.001 MPa/min.....42
5.1	Tensile strengths ($\sigma_{t, f}$) as a function of various t/L ratios under various of loading rates for smooth surface (a) and smooth-slip surface (b).....45
5.2	Constant α as a function of stress rate (σ_R).....46
5.3	Tensile strengths ($\sigma_{t, f}$) as a function for joint frequencies under various of loading rates for smooth surface (a) and smooth-slip surface (b).....48

LIST OF FIGURES (Continued)

Figure	Page
5.4 Constant α^* as a funtion of stress rate (σ_R).....	50
5.5 Elastic modulus as a function of loading rate ($\dot{\sigma}$) and t/L ratios.....	51
5.6 Constant A and B as a function of the t/L ratios.....	53
5.7 Strain energy density as a function of loading rate for different surfaces.....	57
5.8 Mesh model.....	59
5.9 Stresses in the model simulation.....	60
5.10 Strains in the model simulation.....	61
5.11 Deflections in the model simulation.....	62
5.12 Effect tensile stresses under smooth and smooth-slip surface.....	63
5.13 Effect tensile strains under smooth and smooth-slip surface.....	63
5.14 Effect deflections under smooth and smooth-slip surface.....	645
5.15 Tensile stresses as a function of cohesion.....	66
5.16 Tensile stresses as a function of friction angle.....	67
5.17 Tensile stresses as a function of joint shear stiffness.....	68
6.1 Tensile strains as a function normalized deflections (δ_L).....	74
6.2 ϵ as a function δ_L . The tensile strains are plotted as positive.....	74
6.3 Schematic drawing showing how roof deflection can be obtained from actual underground opening.....	75

LIST OF FIGURES (Continued)

Figure		Page
6.4	Strains as a function normalized deflections (δ_L) for uniform load. Note that the tensile strains are plotted as positive in the figure.....	76
6.5	Strain energy of distortion at failure ($W_{d,f}$) as function of mean strain energy at failure ($W_{m,f}$).....	79



SYMBOLS AND ABBREVIATIONS

$\dot{\varepsilon}$	=	Axial strain rate
ε	=	Strain
ε_e	=	Elastic strain
ε_p	=	Permanent strain
σ	=	Stress
E	=	Elastic modulus
η	=	Viscosity
$\varepsilon(t)$	=	Transient creep strain
$\dot{\varepsilon}(t)$	=	Steady-state creep strain rate
t	=	Time
T	=	Absolute temperature
A'	=	Empirical constant for equation (2.4 and 2.6)
B	=	Empirical constant for equation (2.4 and 2.6)
C	=	Empirical constant for equation (2.4)
B'	=	Empirical constant for equation (2.7)
n	=	Empirical constant for equation (2.7)
a	=	Strength parameters for equation (2.9)
σ_c	=	Uniaxial compressive strength
$\sigma_{c,d}$	=	Uniaxial compressive strength at dilation

SYMBOLS AND ABBREVIATIONS (Continued)

$\sigma_{c,f}$	=	Uniaxial compressive strength at failure
σ_1	=	Axial stress
$\sigma_{1,d}$	=	Axial stress at dilation
$\sigma_{1,f}$	=	Axial stress at failure
σ_3	=	Confining pressure
σ_2	=	Confining pressure
τ	=	Shear stress
S_0	=	Shear strength
μ_i	=	Coefficient of internal friction
q	=	Empirical constant for equation (2.11)
m	=	Strength parameters for equation (5.6)
m_d	=	Strength parameters dilation
m_f	=	Strength parameters failure
s	=	Strength parameters for equation (5.6)
c	=	Cohesion
ϕ	=	Internal friction angle
σ_n	=	Normal stress
α	=	Empirical constant for equation (5.3)
μ	=	Empirical constant to calculate β for equation (5.4 and 5.5)
W_d	=	Distortional strain energy
$W_{d,d}$	=	Distortional strain energy at dilation

SYMBOLS AND ABBREVIATIONS (Continued)

$W_{d,f}$	=	Distortional strain energy at failure
W_m	=	Mean strain energy
τ_{oct}	=	Octahedral shear stress
$\tau_{oct,d}$	=	Octahedral shear stress at dilation
$\tau_{oct,f}$	=	Octahedral shear stress at failure
γ_{oct}	=	Octahedral shear strain
$\gamma_{oct,d}$	=	Octahedral shear strain at dilation
$\gamma_{oct,f}$	=	Octahedral shear strain at failure
ϵ_1	=	Major Principal Strain
ϵ_2	=	Intermediate principal strain
ϵ_3	=	Minor principal strain
ϵ_v	=	Volumetric strain
ν	=	Poisson's ratio
G	=	Shear (rigidity) modulus
λ	=	Lame' constant
σ_m	=	Mean stress
$\sigma_{m,d}$	=	Mean stress at dilation
$\sigma_{m,f}$	=	Mean stress at failure
ϵ^T	=	Total strain
ϵ^e	=	Elastic strain
ϵ^c	=	Time-dependent plastic strain

SYMBOLS AND ABBREVIATIONS (Continued)

ε^{*c}	=	Equivalent creep strain
σ^*	=	Equivalent (effective) stress
κ	=	Material parameter
β	=	Material parameter
γ	=	Material parameter
σ_P	=	Pillar stress
$\sigma_{P,d}$	=	Pillar stress at dilation
$\sigma_{P,f}$	=	Pillar stress at failure
FS.	=	Factor of safety
e	=	Extraction ratio
H	=	Mine depth
ρ	=	In-situ stress gradient of overburden
ε_P	=	Pillar strain
ε_A	=	Axial strain
ε_L	=	Lateral strain

CHAPTER I

INTRODUCTION

1.1 Background and rationale

Tensile strength of rock dictates the stability of the immediate roof in stratified rock mass. The tensile strength can be obtained from the laboratory by various methods, including direct tension test, Brazilian tension test, ring tension test, flexural test and three- and four-point bending test (Phueakphum et al., 2013; Wisetsaen et al., 2014). The bending test is however more preferable than the others for analysis and design of the tunnel roof. This is because the test specimen is subjected to the stress configurations similar to those induced in the roof. For stratified and brittle rocks, such as sandstone, the design considerations for opening roofs should also be placed on the tensile strengths and deflection of the materials.

1.2 Research objectives

The objective of this study is to determine the effect of thinly-stratified sandstone on the roof stability of tunnels. Three-point bending tests are performed on prismatic specimens (50×50×200 mm) prepared from the Phu Phan sandstone. The loading rates are varied to obtain the induced tensile stresses at the crack initiation point from 0.001 to 1.0 MPa per minute. The sandstone beds are artificially made in the specimens by saw-cut surfaces and tension-induced fractures to obtain 2 to 5 rock layers arranged normal to the loading directions. The findings can be used to design

the minimum length of rock bolt needed to maintain the stability of the tunnel roof in the stratified sandstone.

1.3 Scope and Limitations

The scope and limitations of the research include as follows:

- 1) All specimens are prepared from the Phu Phan sandstone.
- 2) The nominal dimensions of prismatic blocks are 50×50×200 mm. The sandstone are cut into thin slabs to obtain predefined thickness (e.g. 10, 12.5, 17 and 25 mm) depending on the required joint frequencies.
- 3) The applied loading rates for the three-point bending testing vary from 0.001 to 1 MPa/min.
- 4) The testing procedures follow the relevant ASTM standard practices.
- 5) The research findings are published in conference paper or journal.
- 6) UDEC is used to determine the maximum tensile stresses in the thinly-stratified roof.

1.4 Research methodology

The research methodology shown in Figure 1.1 comprises 7 steps; including literature review, sample preparation, laboratory testing, analysis and assessment, applications, discussions and conclusions and thesis writing

1.4.1 Literature review

Literature review is carried out to study researches about tensile strength, loading rate and four-point bending tests. The sources of information are from

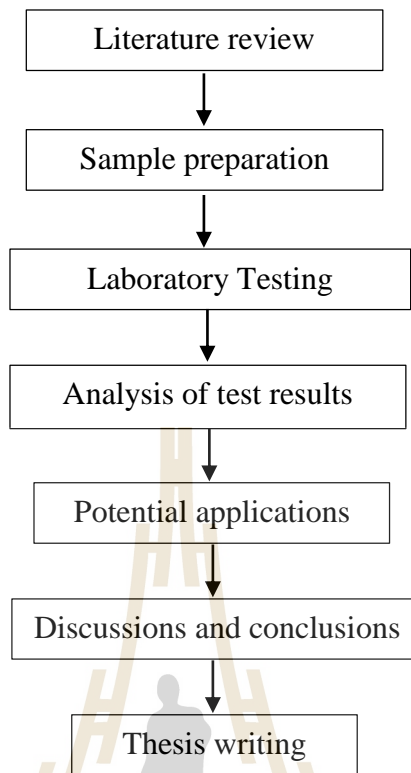


Figure 1.1 Research Methodology.

journals, technical reports and conference papers. A summary of the literature review is given in the thesis.

1.4.2 Sample preparation

The rock specimens used in this study are Phu Phan sandstone which is exposed in the northeast of Thailand. This study makes artificial joints out of saw-cut surfaces using a universal masonry saw (Husqvarna TS 400 F). This saw has a 400-mm diameter blade with a constant rotational speed of 2800 rpm. Water is used as cutting fluid. The saw base has two mutually perpendicular guide rails to provide a precise cutting angle and intervals. Large blocks width (w) is 50 mm., thickness (t) is 50 mm. and length (L) is 200 mm. of the rock specimens are cut into thin slabs to obtain a predefined thickness (t) (e.g. 10, 12.5, 17 and 25 mm). The t/L ratios obtained here

include 0.05, 0.06, 0.08, 0.13 and 0.25. Strain gages are installed in horizontal at the crack initial point. The joint frequencies are 0 (intact rock), 41, 61, 81 and 101 (joint/m)

1.4.3 Laboratory testing

1.4.3.1 Direct shear test

The direct shear tests are performed with the normal stresses of 1, 2, 3 and 4 MPa for the smooth surface and smooth-slip surface. The test method and calculation follow as much as practical the ASTM (D5607-08) standard practice. Each specimen is sheared only once under the predefined constant normal stress using a direct shear machine (EL-77-1030).

1.4.3.2 Three point bending test

The test configurations follow the ASTM (C293-02) standard practice. Figure 8 shows the positions of the loading for the upper and lower bearing plates. A data logger (TC-32K) connected with the switching box (Type B-2760) is used to monitor the induced tensile strains. The loads are applied with constant rates from 0.009 N/s to 9 N/s, which are equivalent to the induced tensile stress rates at the center of the specimen from 2×10^{-5} to 2×10^{-2} MPa/s. The specimen deflection are monitored using dial gage with high precision (± 0.01 mm) which placed at the center of specimen. The load is applied until failure occurs. Specimens containing tension-
induce fracture are also prepared and tested to assess the effect of fracture roughness.

1.4.4 Analysis of test results

The results are presented in forms of the tensile strengths, elastic moduli and strain energy density under various loading rates are presented to describe the mechanical behavior of rock layers. The results are used to develop a set of empirical

equations as a function of loading rate, joint shear stiffness and t/L ratios by SPSS statistical software.

1.4.5 Potential applications

The results can be compared with the strain energy strength criterion developed the criterion can be used to assume the actual stratified roof stability.

1.4.6 Discussions and conclusions

Discussions are made on the reliability and adequacies of the approaches used here. Future research needs are identified. All research activities, methods, and results are documented and complied in the thesis. The research or findings are published in the conference proceedings or journals.

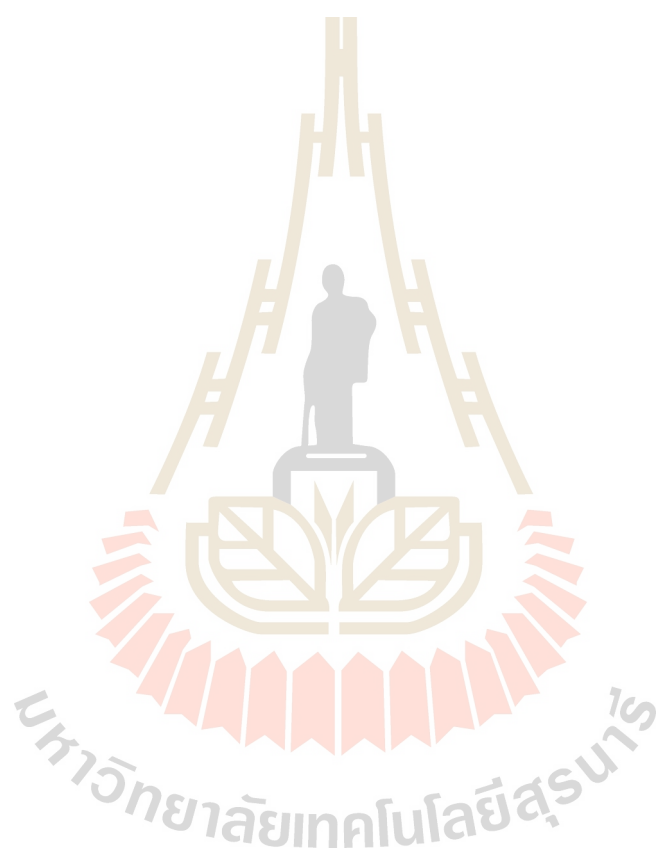
1.4.7 Thesis writing

All study activities, methods, and results are documented and complied in the thesis.

1.5 Thesis content

This research thesis is divided into seven chapters. The first chapter includes background and rationale, research objectives, scope and limitations and research methodology. The second chapter presents results of the literature review about Three-point bending tests, Four-point bending tests, biaxial flexure tensile strength test, stress gradient effect, research on bending test and roof strata stability analysis. The chapter three describes sample preparation. The laboratory testing and test results are described in chapter four. Chapter five presents the results of the test in forms of the tensile strength and elastic moduli under various loading rates and describes the mechanical behavior of rock layers. Chapter six presents the application about tunnel roof in

sandstone to determine maximum supported and chapter seven presents discussions, conclusions and recommendation for future studies.



CHAPTER II

LITERATURE REVIEW

2.1 Introduction

The topic reviewed here include three point bending tests, four-point bending test, biaxial flexure tensile strength test, stress gradient effect, research on bending test and roof strata stability analysis.

2.2 Three-point bending test

The American Society for Testing and Materials (ASTM (C293–02)) specified the methods and sample preparation for the three-point bending test. All forces should be applied perpendicular to the face of the specimen continuously without eccentricity. A diagram of an apparatus that accomplishes this purpose is shown in Figure 2.1. The load shall be applied at a constant rate to the breaking point. The maximum stress on the tension face increases under loading rate between 0.9 and 1.2 MPa/min (125 and 175 psi/min). The loading rate is calculated using the following equation:

$$r = \frac{2Sbd^2}{3L} \quad (2.1)$$

where r is loading rate, N/min (lb/min), S is rate of increase in the maximum stress on the tension face, MPa/min (psi/min), b is average width of the specimen as oriented for testing, mm (in), d is average depth of the specimen as oriented for testing, mm (in.) and L is span length, mm (in).

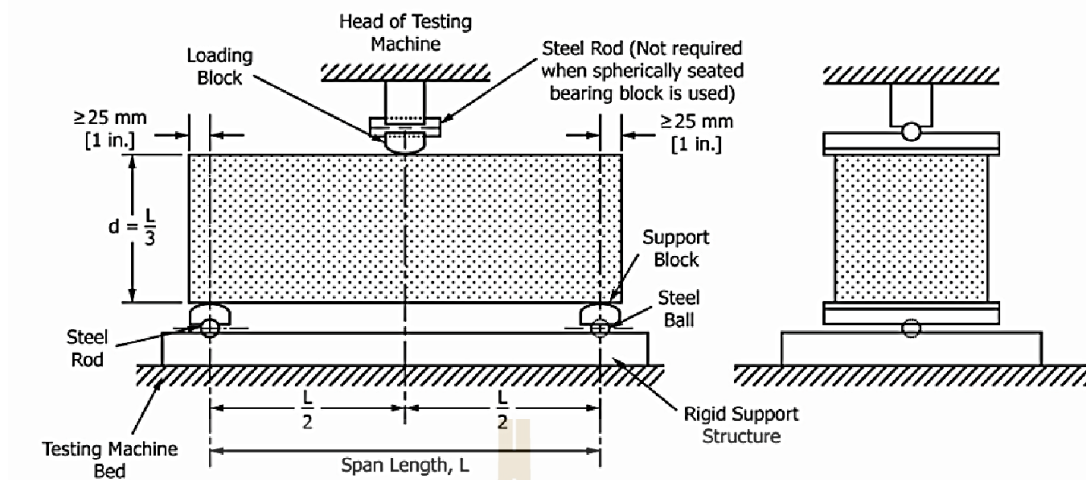


Figure 2.1 Schematic of a suitable apparatus for flexure test by center-point loading method (ASTM (C293-02)).

The modulus of rupture is calculated as follows:

$$R = \frac{3PL}{2bd^2} \quad (2.2)$$

where R is modulus of rupture, MPa (psi), P is maximum applied load indicated by the testing machine, N (lbf), L is span length, mm (in.), b is average width of specimen, at the fracture, mm (in.) and d is average depth of specimen, at the fracture, mm (in.). A bar of rectangular cross section rests on two supports and is loaded at two points or two loading noses. The distance between the loading noses (the load span) is either one third or one half of the support span.

2.3 Four-point bending test

Specifications for standard test method for four-point bending test are given by American Society for Testing and Materials ASTM (D6272-10). The test method is a

bar of rectangular cross section rests on two supports and is loaded at two points or two loading noses, each an equal distance from the adjacent support point. The distance between the loading noses (the load span) is either one third or one half of the support span shown in Figure 2.2. When a beam is loaded in flexure at two central points and supported at two outer points, the maximum stress in the outer fibers occurs between the two central loading points that define the load span. This stress may be calculated for any point on the load deflection curve for relatively small deflections by the following equation for a load span of one third of the support span:

$$S = PL / bd^2 \quad (2.3)$$

For a load span of one half of the support span:

$$S = 3PL / 4bd^2 \quad (2.4)$$

where s is stress in the outer fiber throughout the load span, P is load at a given point on the load-deflection curve, L is support span, b is width of beam and d is depth of beam.

The tangent modulus of elasticity is the ratio, within the elastic limit, of stress to corresponding strain and shall be expressed in MPa. It is calculated by drawing a tangent to the steepest initial straight-line portion of the load-deflection curve and using Equation 5 for a load span of one third the support span and Equation 6 for a load span of one half of the support span, as follows:

$$E_B = 0.21L^3m / bd^3 \quad (2.5)$$

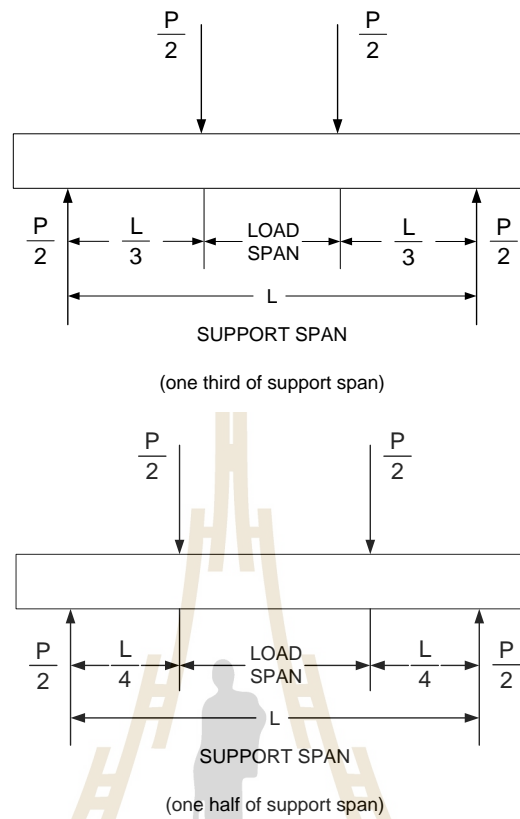


Figure 2.2 Loading diagram (ASTM (D6272–10)).

$$E_B = 0.17L^3m / bd^3 \quad (2.6)$$

where E_B is modulus of elasticity in bending, L is support span, B is width of beam tested, D is depth of beam tested and m is slope of the tangent to the initial straight-line.

2.4 Biaxial flexure tensile strength test

The American Society for Testing and Materials (ASTM (C1550-10)), specifies method for this test. The load is applied to the plate through a ring. Because the support of the specimen is also an annular ring, the stress field is axisymmetric. Mechanical analysis shows that, within the area enclosed by the loading ring, the stress state caused

by the applied load is uniform on every horizontal plane. Consequently, it is easy to consider the statistical randomness of local material strength.

The test has been performed on the circular disks with 100-mm in diameter and 10-mm thick specimens by using ring supported/ring loaded. The biaxial flexural tensile strength test determines the biaxial tensile strengths where $\sigma_1 = 0$ and $\sigma_2 = \sigma_3 < 0$. The circular disk is simply-supported by ring around its outer circumference. The line load (P_c) is applied concentrically to the circular disk through a tube of diameter as shown in Figure 2.3.

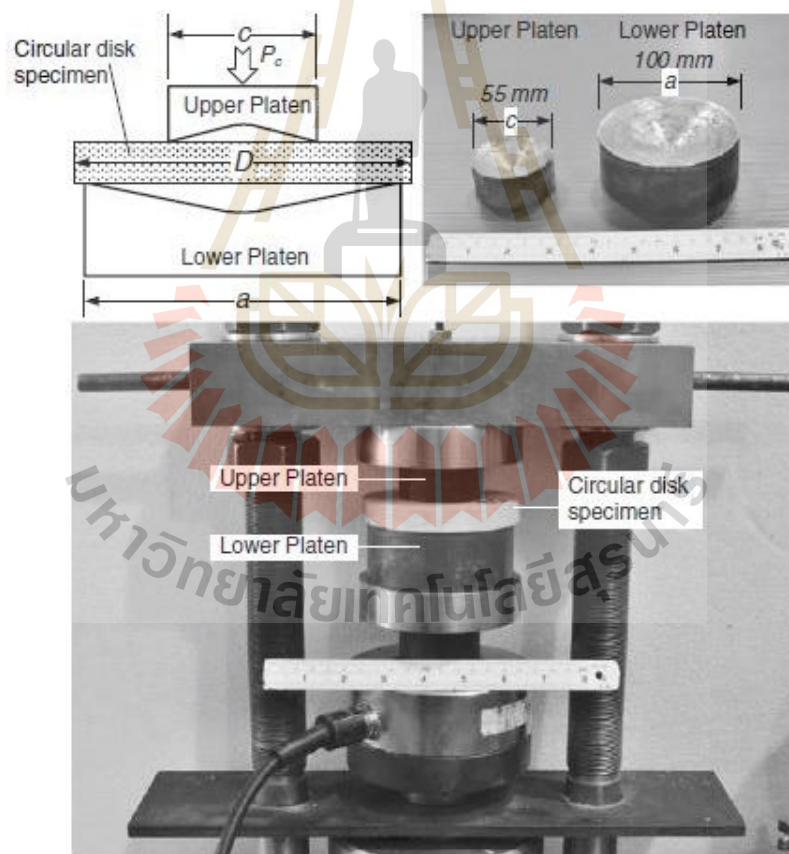


Figure 2.3 Biaxial flexural tensile strength tests arrangement (Phueakphum et al., 2013).

The analytical solution used to determine the biaxial tensile strength of a symmetric isotropic thin circular disk is expressed below (Morrell, 1998; Ugural, 1999) where the tangential and radial tensile strengths (σ_r and σ_t) are equal.

$$\sigma_r = \sigma_t = 3P_c/4\pi t^2 [(1-\nu)(1-c^2/a^2) + 2(1+\nu)\ln(a/c)] \quad (2.7)$$

where P_c is maximum load at failure, t is the thickness of circular rock sample, ν is Poisson's ratio, and a , c are the outside and inside diameters.

2.5 Stress gradient effect

Claesson and Bohloli (2002) state that the tensile strength of rock is among the most important parameters influencing rock deformability, rock crushing and blasting results. To calculate the tensile strength from the indirect tensile (Brazilian) test, one must know the principal tensile stress, in particular at the rock disc center, where a crack initiates. This stress can be assessed by an analytical solution. A study of this solution for anisotropic (transversely isotropic) rock is presented.

Liao et al. (1997) study the tensile behavior of a transversely isotropic rock by a series of direct tensile tests on cylindrical argillite specimens. To study the deformability of argillite under tension, two components of an electrically resistant type of strain gage with a parallel arrangement, or a semiconductor strain gage, are adopted for measuring the small transverse strain observed on specimens during testing. The curves of axial stress and axial strain and average volumetric strain are presented for argillite specimens with differently inclined angles of foliation. Experimental results indicate that the stress-strain behavior depends on the foliation inclination of specimens with respect to the loading direction. The five elastic constants of argillite are

calculated by measuring two cylindrical specimens. Based on theoretical analysis results, the range of the foliation inclination of the specimens tested is investigated for feasibility obtaining the five elastic moduli. A dipping angle of the foliations (ϕ) of 30-60° with respect to the plane normal to the loading direction is recommended. The final failure modes of the specimens are investigated in detail. A saw toothed failure plane occurs for the specimens with a high inclination of foliation with respect to the plane perpendicular to the loading direction. On the other hand, a smooth plane occurs along the foliation for specimens with low inclination of foliation with respect to the plane normal to the loading direction. A conceptual failure criterion of tensile strength is proposed for specimens with a high inclination of foliation.

Klanphumeesri and Fuenkajorn (2010) study the direct tensile strength and deformability from dog-bone shaped specimens of intact sandstone, limestone and marble using a compression-to-tension load converter. The device allows a measurement of the rock elastic modulus and Poisson's ratio under uniaxial tensile and compressive stresses on the same specimen. A series of finite difference analyses is performed to obtain a suitable specimen configuration that provides unidirectional tensile stresses at the mid-section. Results indicate that the direct tensile strengths are clearly lower than the Brazilian and ring tensile strengths. The elastic moduli and Poisson's ratios under uniaxial tension are lower than those under uniaxial compression. The discrepancy probably relates to the amount and distribution of the pore spaces and micro-fissures, and the bond strength of cementing materials. The porous and relatively poor-bonding sandstone shows a greater difference between the tensile and compressive elastic moduli and Poisson's ratios compared to those of the dense and well bonding marble and limestone.

Fuenkajorn and Daemen (1986) conduct the ring tension tests on 229 mm (9 in) diameter disks of Grande basaltic andesite and Pomona basalt with various center hole sizes in order to study the relationship between ring tensile strength and relative hole radius (hole radius/disk radius). The tensile strength (σ_R), decreases as the relative hole radius increases. A power equation represents the coefficients of strength and shape, respectively adequately represents the ring tensile strength as a function of relative hole radius over the range investigated. The equation can be used to distinguish the effect of the hole size from the strength results, to predict the tensile strength of a ring sample containing arbitrary hole sizes, and to approximate the critical relative hole radius of the material tested.

Phueakphum et al. (2013) determine the effects of intermediate principal stresses on the tensile strength of rocks. The results are used to assess the predictive capability of the Coulomb criterion when one or more principal stresses are in tension. Four rock types have been tested. The laboratory testing involves four-point bending test, Brazilian tension tests with axial compression, and biaxial flexural tensile strength tests. Uniaxial, biaxial and triaxial compressive strengths are also determined to correlate their results with those of the tensile testing. Results indicate that the four-point bending and Brazilian tensile strengths with axial compression provide a linear transition with the triaxial extension test results. This is because they are all under the condition where $\sigma_1 = \sigma_2 > \sigma_3$. Based on the Coulomb criterion, the biaxial flexural tensile strength correlates well with the conventional uniaxial and triaxial compressive strengths of the rocks. The compressive and tensile strengths and cohesion obtained from the triaxial extension tests ($\sigma_1 = \sigma_2$) are greater than those from the triaxial compression tests ($\sigma_2 = \sigma_3$). Both stress conditions give similar internal friction angle.

More important the results indicate that the Brazilian tensile strength can not correlate with the two stress conditions. It is recommended that an extension of the Coulomb criterion into the tensile region should be correlated with the tensile strengths obtained from the biaxial flexural tensile strength test rather than the Brazilian tension test.

2.6 Research on bending test

Zhang and Wong (2014) discuss the loading mechanisms associated with different loading rates in the bonded-particle model (BPM) and examine the numerical outputs under these different rates for use in which calibration against the results from Brazilian tensile tests. The specimens in the numerical analysis of the Brazilian tensile tests are subjected to vertical loading applied at six different loading rates: 0.005, 0.01, 0.02, 0.08, 0.2 and 0.6 m/s. The induced tensile stress (σ_t) is calculated as follows:

$$\sigma_t = \frac{F}{\pi R t} \quad (2.8)$$

where F is the compressive force acting on the platens, R and t are the radius and thickness of the Brazilian disk, respectively. The peak value of the induced tensile stress is the Brazilian tensile strength of the test specimen. The results from the Brazilian tensile tests indicate that the Brazilian tensile strength increases as the loading rate increases.

Agioutantis et al. (2015) study the potential of acoustic emissions from three point bending (TPB) tests as rock failure precursors. A simply supported prismatic beam of rectangular cross section with span length (l_s), width (b) and thickness (h), is

subjected to a concentrated and centrally applied force (P). Assuming that the material behaves linearly elastic, this geometry and loading ensures a linear stress state in the center plane of the specimen. According to this distribution, the expected failure mode is the splitting of the specimen in two halves across the plane of loading. For elastic materials, the maximum tensile stress (σ_{\max}) is a measure of the tensile strength as follows:

$$\sigma_{\max} = \frac{3PI_s}{2bh^2} \quad (2.9)$$

Assuming that the material fails in brittle mode after elastic loading, the maximum tensile stress at failure is a material property called bending tensile strength (σ_t) following this equation:

$$\sigma_t = \frac{3P_f I_s}{2bh^2} \quad (2.10)$$

where P_f is the fracture load.

Yokoyama (1988) derives a useful formulation for the stress-strain relation in a four-point bending test. The analysis utilizes the experimental measurements of the axial load (P), the strains at the top and bottom of the beam and the geometry of the device and the beam. This derivations lead to the following values of σ_t and σ_c , the maximum tensile stress and the maximum compressive stress along the beam (fiber stresses)

$$\sigma_t = \frac{dM(\varepsilon_t + \varepsilon_c) + 2M(d\varepsilon_t + d\varepsilon_c)}{bh^2 d\varepsilon_t} \quad \sigma_c = \frac{dM(\varepsilon_t + \varepsilon_c) + 2M(d\varepsilon_t + d\varepsilon_c)}{bh^2 d\varepsilon_c} \quad (2.11)$$

where $M = 0.5P(L_t - L_c)$ is the bending moment of the beam, L_t and L_c are the spacing of pairs of the loading point for the tensile side and for the compressive side, respectively, ε_t and ε_c are the tensile and compressive strains measured at the top and bottom of the deformed beam, respectively (fiber strains), b is the beam width, h is the beam height, dM , $d\varepsilon_t$ and $d\varepsilon_c$ are the increments of the moment and the strain during the experiment (the differentials between two consecutive steps in the experiment).

Obert and Duvall (1967) propose the solution for the maximum stress (σ_{\max}) values at the abutments for compression (bottom of beam) or tension (top of beam). The maximum beam deflection (δ) can be easily calculated using closed form beam equations as follows:

$$\sigma_{\max} = \frac{\gamma S^2}{2T} \quad (2.12)$$

$$\delta = \frac{\gamma S^4}{32ET^2} \quad (2.13)$$

where E is the Young's modulus of the rock, γ is the specific weight, S is joint spacing and T is the thickness. The maximum stress at the mid-span is one half of the maximum stress at the abutments. Therefore, for such a beam with fixed ends and distributed loading, yield is assumed when the maximum tensile stress in the upper part of the beam at the abutments exceeds the tensile strength of the rock. Vertical tensile fractures form at the abutments and the beam becomes simply supported (assuming no slip at the abutments) as shown in Figure 2.4(b) with a maximum tensile stress at the mid span given by

$$\sigma_{\max} = \frac{2\gamma S^2}{3T} \quad (2.14)$$

This stress is higher than the previous abutment stress, and therefore higher than the rock tensile strength. This leads to subsequent fracturing centered about the mid span as shown by Stimpson and Ahmed (1992). Snyder (1983) considers a laminated rock beam an excavation with a horizontal span by the normal thickness of the single layer under analysis. An elastic beam with no joints and with constant cross section, the compression distribution and tension symmetrical about the horizontal centreline of the beam is found across all plane sections within the beam. as shown in Figure 2.4.

Bucky and Taborelli (1938) study the physical models of the creation and extension of wide roof spans. They found that a vertical tension fracture induced at the center of the lower beam. Increasing of the mined span produced a new central fracture, and closed the earlier fracture. This suggested that the central fracture is the dominant transverse discontinuity in the roof bed.

Evans (1941) investigates the roof deformation mechanics at the Royal School of Mines. This work established the notion of a 'Voussoir beam' spanning an excavation, using the analogy with the Voussoir arch considered in masonry structures. This study developed an analytical procedure for assessing roof beam stability, however an error in statics and failure to handle the basic indeterminacy of the problem limited its practical application.

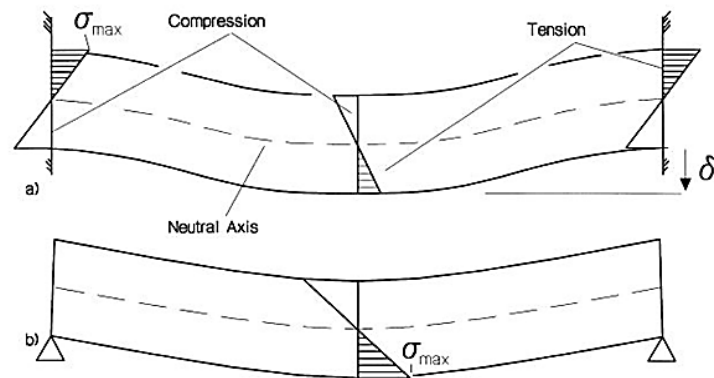


Figure 2.4 Elastic beam with (a) fixed ends and (b) simple (pin) supports (Snyder, 1983).

Sterling (1980) studies the deformation and failure modes of roof rock. A rock beam of typical dimensions 660 mm × 75 mm × 75 mm was constrained between steel end plates linked by strain-gauged tie rods. The beam was loaded transversely by a servo controlled testing machine and a load spreading system. The experiment design provided data on applied transverse load, induced beam deflection, induced lateral thrust, and eccentricity of the lateral thrust.

Lorig and Brady (1983) describe application of a linked boundary element–distinct element (b.e.–d.e.) computational scheme to analysis of roof deformation mechanics. The key results of the analysis are indicated. Slip is observed over the abutments of the excavation, the immediate roof bed detaches from the overlying strata, and tension cracks open in the center of the roof span. The distributions of normal stress and shear stress in the roof bed were generally consistent with the Voussoir beam model proposed.

Exadaktylos et al. (2001) study elastic theory and Voussoir beam analogy. The strain distribution in each section is assumed to be triangular (Figure 2.5(a)), with a

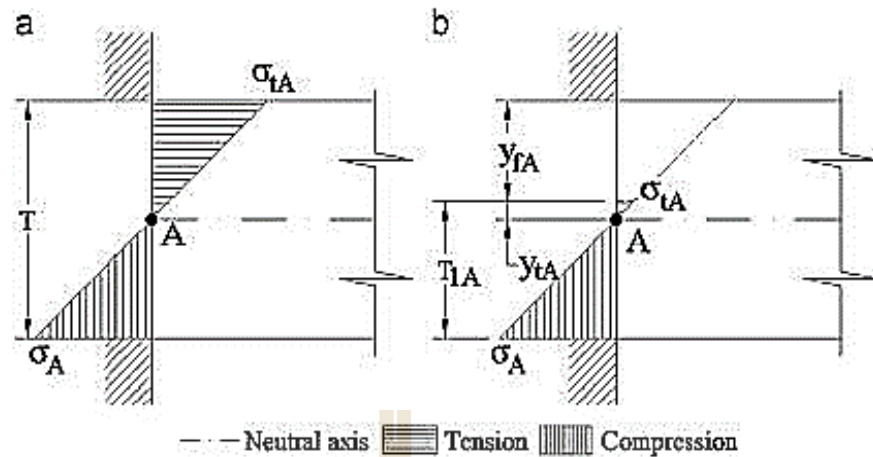


Figure 2.5 Variation of the stresses along the height of a beam (Exadaktylos et al., 2001).

symmetrical distribution of compression and tensile stresses about the horizontal midline. But there are studies that refute the hypothesis of a symmetrical distribution of compression and tensile stresses. In this case, the distribution of stresses adopts a form similar to that depicted in Figure 2.5(b), where the tensile strength of the rock is approximately 10% of its compressive strength. In this work, a non-linear failure criterion for rock mass is proposed, based on the double theory of elasticity, and from it the determination of the maximum span that can support the tensile stresses through the roof. Besides, the behavior of the roof when the tensile stresses increase the tensile strength is analyzed. The method is applied on two real examples: Kampanzar Quarry situated in the municipality of Arrasate in Gipuzkoa (Spain) and Calzada Quarry situated in Villamartín de Vadeorras in Orense (Spain). The numerical results have been compared with those ones obtained from the Stephansson formulation, and the behavior after failure is compared with the compression arch assumed by the Voussoir beam analogy

2.7 Roof strata stability analysis

Shabanimshcool and Li (2015) present two analytical approaches for studying the stability of Voussoir beams by taking into account the horizontal loading condition of the beams: with and without horizontal in-situ stresses. For beams without being subjected to horizontal stresses, a bilinear truss represents the compression arch formed in the Voussoir beam. The stability of the compression arch is analyzed by the energy method. An iteration algorithm was proposed for the solution. The results of the approach are verified with UDEC simulations as well as experimental results. For beam is subjected to horizontal in-situ stresses, the classic beam theory was employed to study their behavior.

The assumptions for the analytical approaches are verified by numerical simulations. The study shows that increasing of the Young's modulus improves the stability of the beams against buckling. However, it elevates the stresses in the horizontal direction within the compression arch, which may result in crushing failure in the beam abutments and the mid-span. Low horizontal in-situ stress reduces the risk of beam buckling but increases the risk of sliding at the abutments. However, high horizontal in-situ stress may cause either beam buckling or crushing failure in the abutments. The developed analytical approaches would be applicable for roof stability analysis in stratified rocks.

Yan et al. (2016) suggest that bedding separation in roof strata (BSRS) overlying roadways within thick coal seams (RTCS) is an important factor leading to surrounding instability in underground coal mines, and especially to roof failures such as convergence, and even caving-in. In this research, the theoretical analysis is combined with the test results to predict the locations which BSRS occurred. Based on

standard monitoring methods widely used in exploring roof behavior in underground coal roadways, a typical roadway excavated within 12.87 m, in an average thickness coal seam, in Jinggonger coal mine, Pingshuo Coalfield, Shanxi province, China, that was chosen to explore the mechanism underpinning BSRS, and a set of monitoring designs, mainly including five groups of stations and 16 instruments, is determined and applied to this research. Results showed that the predicted locations of BSRS overlying RTCS were in accordance with field monitoring results. This proved the validity of the theoretical model. Besides, the working face played an important role in BSRS and 75% of the BSRS events were generated within the 50 m between the monitoring station and the working face. When the distance was decreased to 5 m, the BSRS was up to 90.9 mm and 86 mm at depths of 6.8 m and 3.8 m, respectively. Meanwhile, three stages were considered, step-by-step, as opposed to mining activity dependent upon the extent of its influence on BSRS: a pink value (indicative of an alarm status) prevailed during the third stage.

Hatzor and Benary (1998) found that the normal stress increases with increasing beam span and decreases with increasing beam thickness. The calculated results, however, are only valid for a beam consisting of a single layer. Their cases are shown in the heavy line in Figure 2.6 for a beam span of 7 m. The value of σ_n obtained for an individual layer thickness of 0.25 m, is 2.45 MPa. For a single layer beam with thickness of 2.5 m, σ_n is 0.244 MPa. The average of bed thickness is 0.5 m. Assuming that each bed transmits axial thrust independently from the neighboring layers above and below, σ_n within a single layer should be 1.22 MPa. These values are significantly lower than the unconfined compressive strength of the rock which is about 7 MPa. The beam should be considered safe against failure by local crushing at hinge zones.

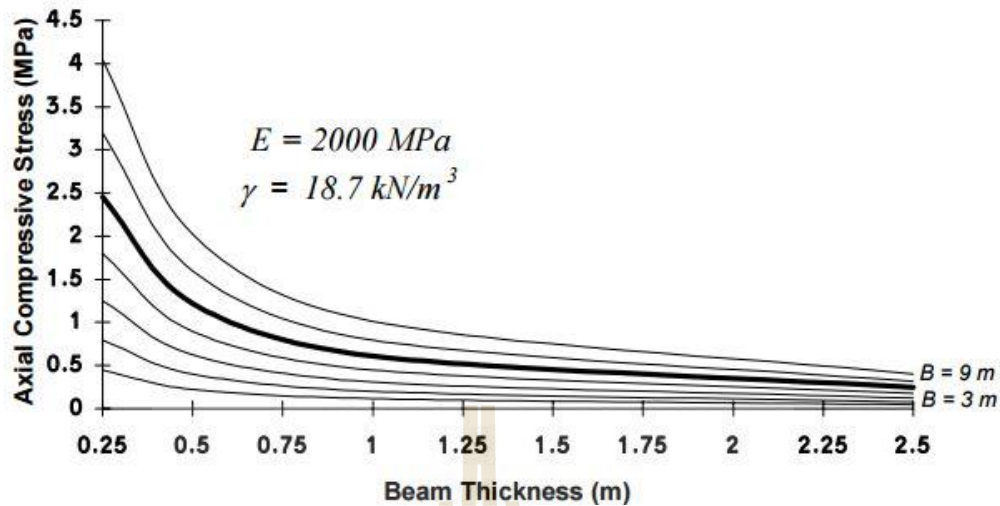


Figure 2.6 The relationship between maximum horizontal compressive stress in beam and beam thickness for various roof span values (B). The case of they are (B =7 m) shown using bold line (Hatzor and Benary, 1998).

Yeung and Goodman (1995) study the effect of friction angle on various rock bolting schemes in rock mass. A block fracturing algorithm is implemented in discontinuous deformation analysis (DDA) using a three parameter Mohr-Coulomb criterion (cohesion, friction and tensile strength) where fracturing can be either in shear or in tension. Furthermore, a sub-blocking capability was which allows better analysis of stress and strain distributions within otherwise simply deformable DDA blocks. Validation of DDA using real case studies, however, has rarely been attempted. The study indicates that can be qualitatively rationalized as follows: with increasing joint spacing the moment arm length in individual blocks increases and the arching mechanism by which axial thrust is transmitted through the blocks to the abutments is enhanced. However, above a limiting value of block length, found here to be represented by a layer consisting of four blocks, the weight of the overlying blocks

becomes more dominant, and the stabilizing effect of greater axial thrust is weakened by the destabilizing effect of dead load transfer from the weight of overlying blocks. Finally, when a single layer consists of a single block which is not clamped at the ends arching deformation is unlikely, due to the relatively high stiffness of individual layers.

Yang et al. (2013) use the finite difference method to model tunnel excavation construction in stratified rock mass. To demonstrate the sensitivity of stratified rock mass structure on numerical modeling results, the influence of the side-pressure coefficient K on stratified rock mass stability is explored in their research. Moreover, displacement distribution and stress are studied as well.

Agapito and Gilbride (2002) present case histories illustrating the practical usage of roof stress determination for help assess stability, not only in case of high horizontal stresses but also of low stresses. They conclude with a comparative evaluation on the effect of various stress fields on ground support requirements.

Maleki and Owens (1998) study the mechanics of strata deformation as influenced by geologic conditions, pillar extraction methods, and MRS load-bearing capabilities. To provide a better understanding of the mechanics of strata deformation, the authors have collected and reviewed measurements of convergence and stress in one western U.S. mine and have completed pseudo-three-dimensional, boundary-element modeling for two typical pillar-pulling plans. Stress distribution in the mine roof above pairs of MRS's was calculated to demonstrate how MRS's contributed to the control of roof block movements.

Shen and Zhang (2016) suggest that the tunnel and stratum deformation are big when the thickness of the weathered sandstone above tunnel is thin, and surrounding rock before tunnel face has produced a certain deformation after tunnel excavation. The

position of the maximum horizontal displacement is related to the interface position above the tunnel. When the interface is close to the tunnel vault, the position occurs in the interface location rather than the arch waist, and the surface settlement trough is deeper. At the same time, the actual deformation of the vault settlement can be calculated by the monitoring data and the numerical calculation results. In order to ensure the safety of the tunnel construction, series of auxiliary measures are adopted in this project. These research result can provide reference to the similar engineering.



CHAPTER III

SAMPLE PREPARATION

3.1 Introduction

This chapter describes the procedure and methods for rock specimen preparation in the laboratory. The rock specimens used in this study are Phu Phan sandstone which exposed in the northeast of Thailand. A total of 36 specimens has been prepared for fractures made by saw-cut surface. A total of 4 specimens are prepared for tension-induced fractures.

3.2 Sample preparation

3.2.1 Direct shear test

The Phu Phan sandstone are prepared to obtain rectangular block specimens with nominal dimensions of $100 \times 90 \times 150 \text{ mm}^3$. The fractures are artificially made in the laboratory by saw-cut methods with nominal area of $100 \times 90 \text{ mm}^2$ (Figure 3.1). A total of 2 specimens are made.

3.2.2 Three-point bending test

3.2.2.1 Saw-cut surface

The specimens used for the three-point bending tests are prepared as rectangular blocks with nominal dimensions of 50 mm thickness (t), 50 width (w) and 200 mm length (L). This study makes artificial joints out of saw-cut surfaces using a universal masonry saw (Husqvarna TS 400 F). This saw has a 400-mm diameter blade with a constant rotational speed of 2800 rpm. Water is used as cutting fluid.

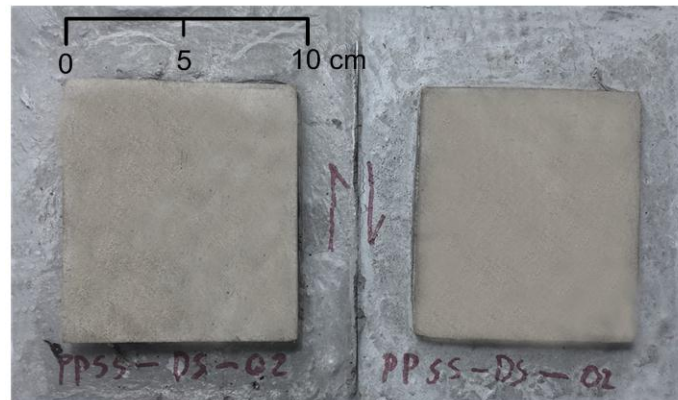


Figure 3.1 Examples of smooth surface prepared in Phu Phan sandstone.

The saw base has two mutually perpendicular guide rails to provide a precise cutting angle and intervals. Large blocks of the rock specimens are cut into thin slabs to obtain a predefined thickness (Figure 3.2). The t/L ratios obtained here are 0.25, 0.13, 0.08, 0.06 and 0.05 (mm/mm). The joint frequencies are 0 (intact rock), 41, 61, 81 and 101 (joint/m) (Table 3.1). Total of 36 rock samples are prepared here.

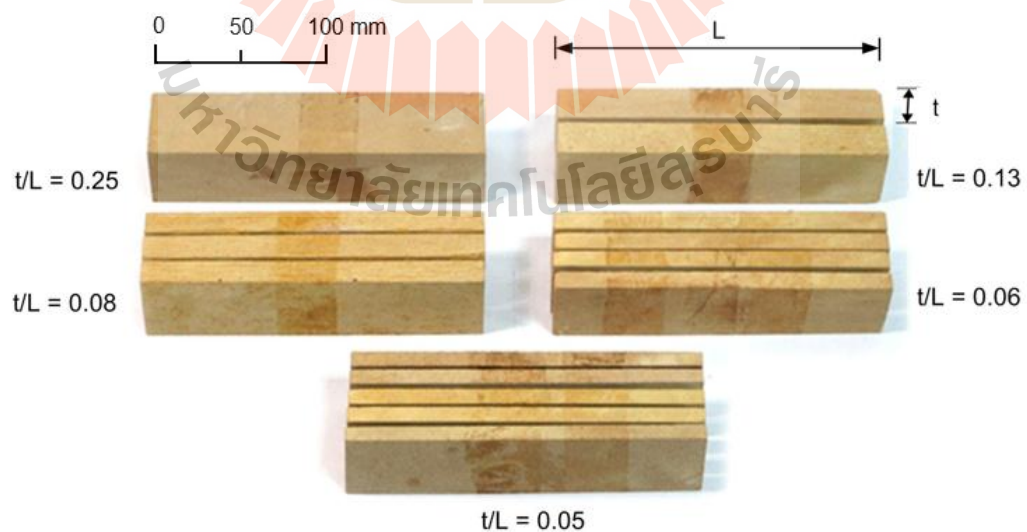


Figure 3.2 Sample specimens for three point bending test.

Table 3.1 Rock sample dimensions with various t/L ratios.

Samples	Thickness (t) mm	Length (L) mm	t/L ratios	Joint frequencies (joints/m)
Intact rock 	50.0	200	0.25	0
2 layers 	25.0		0.13	41
3 layers 	17.0		0.08	61
4 layers 	12.5		0.06	81
5 layers 	10.0		0.05	101

3.2.2.2 Roughness surface

The fractures are artificially made in the laboratory by tension inducing method for 50×50×200 mm prismatic blocks by line-loading to induce tensile fracture in the mid-length of the block. Their roughness is observed and classified by comparing with a reference profiles given by Barton (joint roughness coefficient-JRC, Barton, 1973). Figure 3.3 shows the joint roughness of the rock samples.

3.2.3 Strain gage installation

A strain gage (TML, PFL-20-11-1L, 20 mm) is installed to measure tensile strains at the center of the specimen in horizontal and the main axis of the

specimen which is parallel to the bedding planes (Figure 3.4). Gage length used here is 20 mm. Gage factor is $2.13 \pm 1\%$.

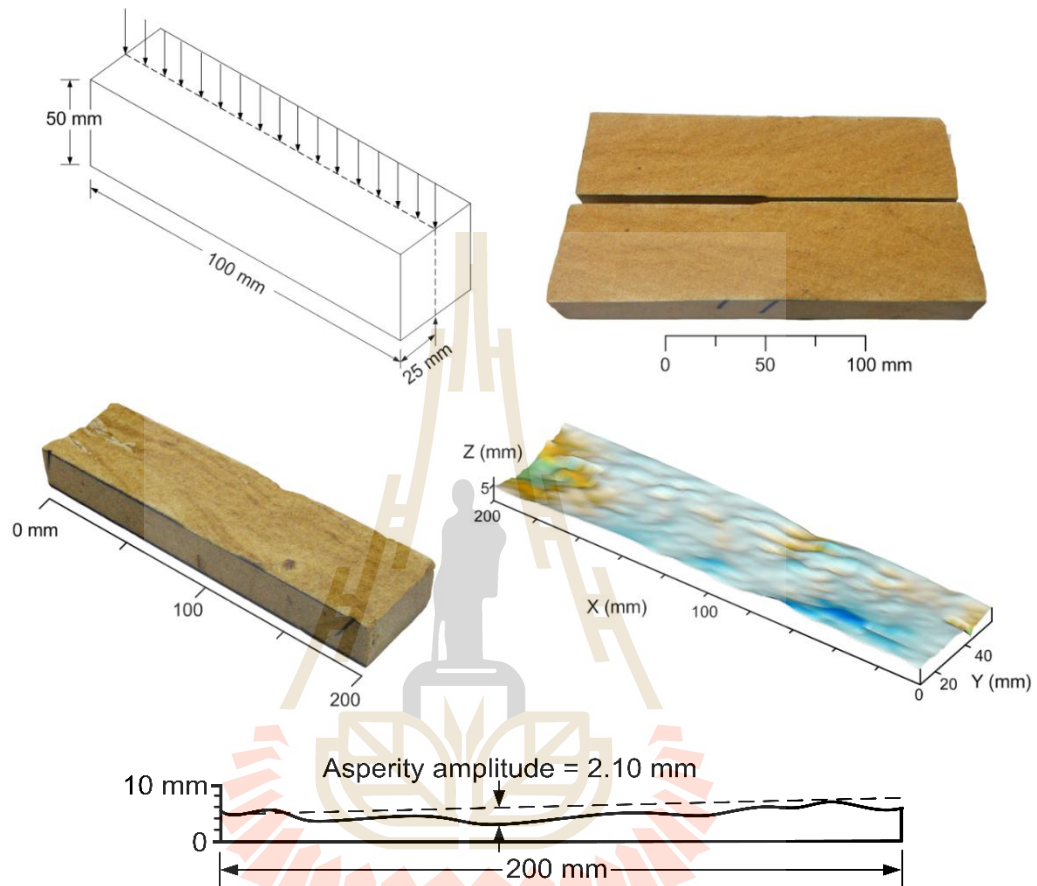


Figure 3.3 Joint roughness of rock samples (JRC = 10).

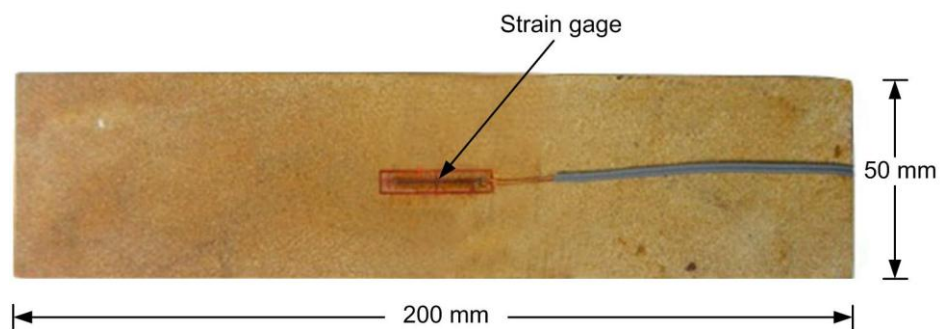


Figure 3.4 Examples of prismatic specimens with strain gage position.

CHAPTER IV

LABORATORY TESTING AND RESULTS

4.1 Introduction

The objective of this chapter is to describe the test methods and results of the direct shear and bending tensile strength tests. The results have been used to determine the effects of thickness and loading rates on the tensile strengths of the Phu Phan sandstone specimens. All proposed testing procedures and equipment are also described.

4.2 Direct shear tests

The direct shear tests are performed to determine the maximum shear stress of Phu Phan sandstone. Laboratory arrangement for the direct shear test equipment is shown in Figure 4.1. The constant normal stresses used are 1, 2, 3 and 4 MPa for the smooth surfaces and the smooth-slip surfaces. Vaseline is used to make smooth-slip surfaces to assess the effect of friction on the results. The rates of shear displacement are maintained constant at 0.01-0.02 mm/s. The maximum shear displacement is 5 mm. The test method and calculation follow as much as practical the ASTM (D5607-08) standard practice. The failure modes are recorded. The test results are presented in the forms of the shear strength as a function of normal stress

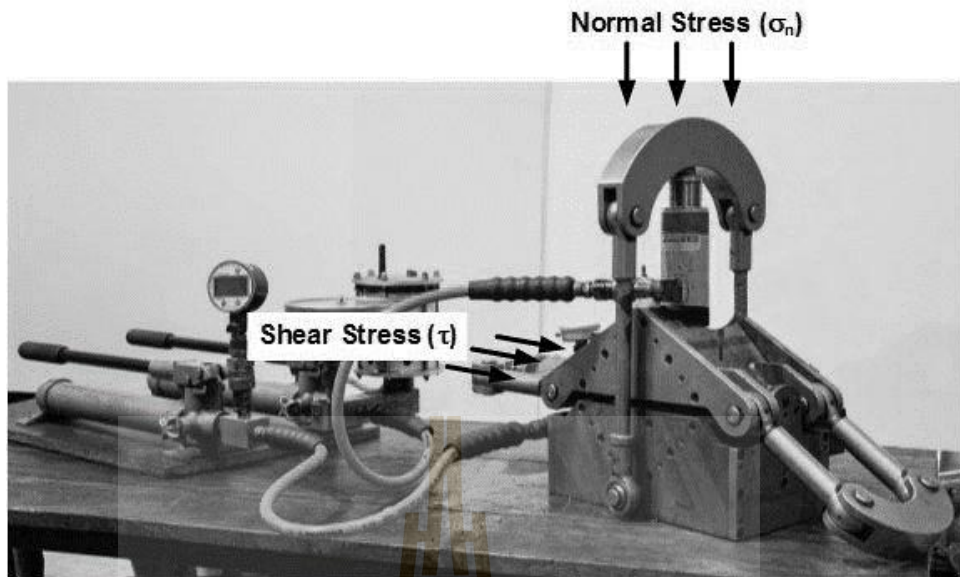


Figure 4.1 The direct shear machine model EL-77-1030 for direct shear tests.

4.3 Three-point bending test

The test configurations for the three-point bending test follow the ASTM (C293-02) standard practice. Figure 4.2 shows the loading positions for the upper and lower bearing plates. A data logger (TC-32K) connected with the switching box (Type B-2760) is used to monitor the induced tensile strains from the strain gage installed across the incipient crack (Figure 4.3). The loads are applied with constant rates from 0.009 N/s to 9 N/s, which are equivalent to the induced tensile stress rates at the center of the specimen from 2×10^{-5} to 2×10^{-2} MPa/s. The specimen deflections are monitored by dial gage with high precision (± 0.01 mm) which placed in vertical at the center of specimen. The load is applied until failure occurs. The induced tensile stress can be calculated by:

$$\sigma_t = 3PL / 2bd^2 \quad (4.1)$$

where σ_t is tensile stresses, P is applied load, L is support span (150 mm), b is specimen width (50 mm), and d is specimen thickness (50 mm). The tensile stress is defined here as positive values for a convenience of presentation.

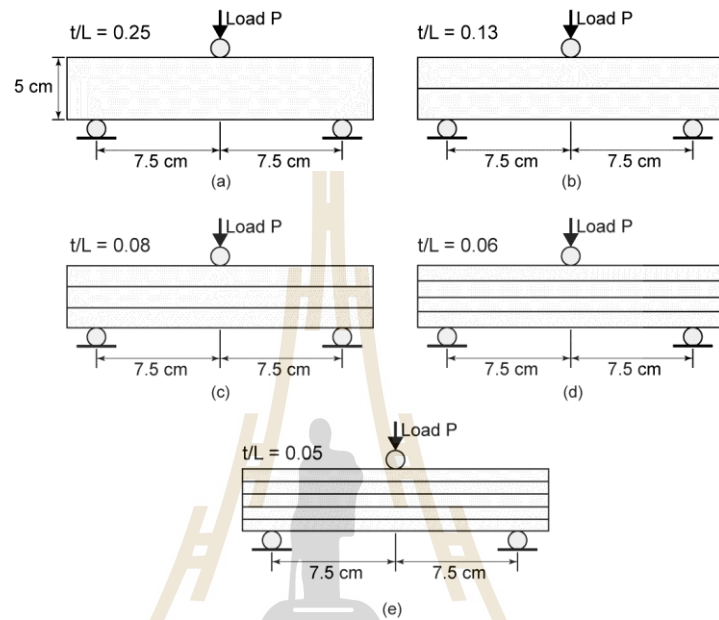


Figure 4.2 Schematic of a three-point beam bending test method (ASTM (C293-02)).

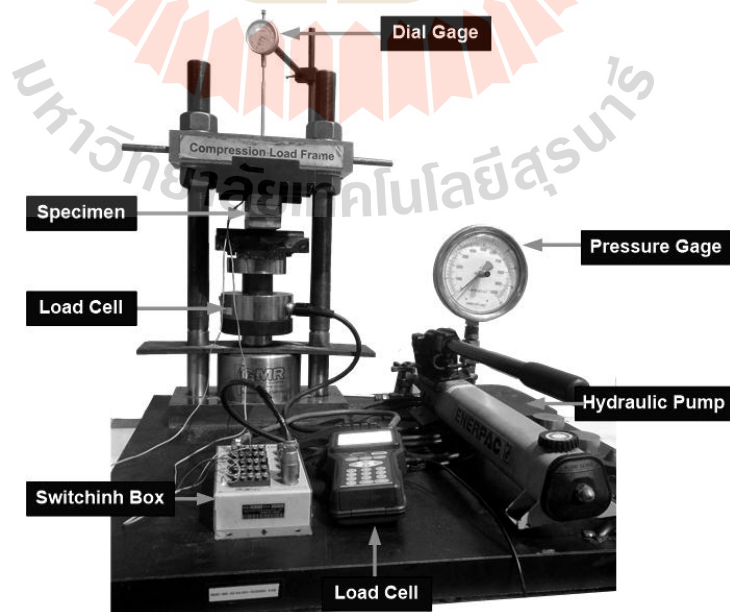


Figure 4.3 Three-point bending test arrangement.

4.4 Test results

4.4.1 Direct shear test results

The shear stresses are calculated and presented as a function of shear displacement for each constant normal stress. Figure 4.4 shows shear stress-displacement curves under 1 MPa (minimum) to 4 MPa (maximum) normal stresses. The joint shear stiffness (K_s) is calculated from the linear slope of the shear stress-displacement curves (Figure 4.4). The joint shear stiffness (K_s) of the smooth and smooth-slip surface is 1,300 MPa/m and 100 MPa/m, respectively. The direct shear test results are presented in the form of the Coulomb's criterion. The line tangent to each of these circles defines the Coulomb's criterion and can be expressed by:

$$\tau = c + \sigma_n \tan \phi \quad (4.2)$$

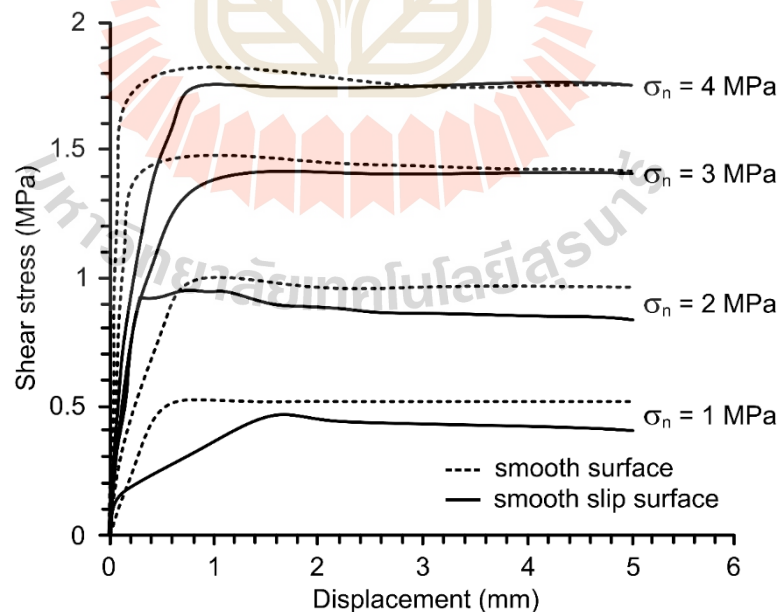


Figure 4.4 Shear stresses of Phu Phan sandstone as a function of shear displacement for smooth surface and smooth-slip surface.

where τ and σ_n are the shear stress and normal stress, ϕ is the friction angle and c is cohesion. Figure 4.5 shows the peak shear stresses of the Phu Phan sandstones as a function of normal stress. The friction angle of the smooth and smooth-slip surface (ϕ) are 25° and 24° and the cohesions are 0.13 and 0.09 MPa, respectively. The cohesion, friction angle and K_s of all specimens are summarized in Table 4.1. Note that application of vaseline on the smooth saw-cut surface slightly reduces the frictional resistance of the surface.

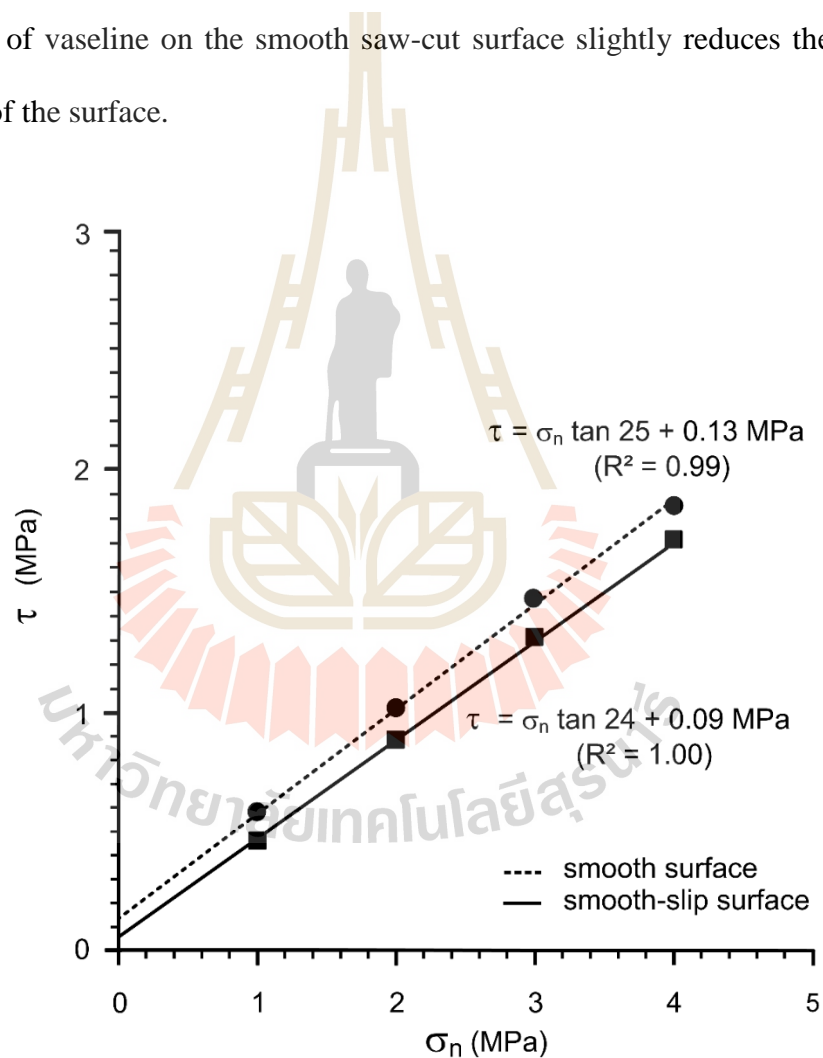


Figure 4.5 Peak shear stresses as a function of normal stress.

Table 4.1 Summary of test results of smooth surface and smooth-slip surface.

σ_n (MPa)	Smooth surface				Smooth-slip surface			
	τ_{peak} (MPa)	ϕ (Degree)	c (MPa)	K_s (MPa/m)	τ_{peak} (MPa)	ϕ (Degree)	c (MPa)	K_s (MPa/m)
1	0.46	25	0.13	1,300	0.51	24	0.09	100
2	0.95				0.98			
3	1.47				1.41			
4	1.82				1.82			

4.4.2 Three point bending test results

Table 4.2 shows some post-test specimens from the three-point bending test under the t/L ratios of 0.25, 0.13, 0.08, 0.06 and 0.05 (mm/mm) with loading rates of 0.001, 0.01, 0.1 and 1 MPa/m. The results show that the fractures occur at the center of specimen for all testing this is because this point is under maximum tensile stresses. From observation during testing it is found that the fracture sudden failure from lowest slab to the upper ones. There is no shear stress observed between the rough surfaces of slab. This probably because there is not movement between the rough surfaces of slab.

The tensile stress-strains curves for various rates of 0.001 to 1 MPa/m can be plotted from the test results, as shown in Figures 4.6 through 4.9. The stress-strain and stress-deflection relations are nonlinear, particularly under the low loading rates. Higher loading rates applied result in higher stresses and lower strains at failure. It is obvious that the specimens with high t/L ratio (0.25) show higher tensile strengths at failure than those with lower t/L ratio (0.05) due to the effect of the joint spacing of the specimens. Under the same t/L ratio the smooth surfaces show higher tensile strengths and lower tensile strains at failure than those with smooth-slip surfaces because effect

the properties for joint spacing. This holds true for all loading rates. Higher loading rates yield higher tensile strengths.

Figure 4.10 shows the failure which most occurs in the lowest slab for the three-point bending test due to it is under maximum tensile stresses. The crack always appears bottom slab. Figures 4.11 through 4.14 show the tensile stress-deflections for various rates of 0.001 to 1 MPa/m. The higher deflection occurs for lower rate. It is found that the specimens with lower t/L ratio (0.05) and lower rate (0.001 MPa/m) show higher deflections at failure than those with high t/L ratio (0.25). Tables 4.2 and 4.3 summarize the tensile strengths, strains and deflections of three-point bending test on the intact rock, tension-induced fractures, smooth and smooth-slip surface, respectively.

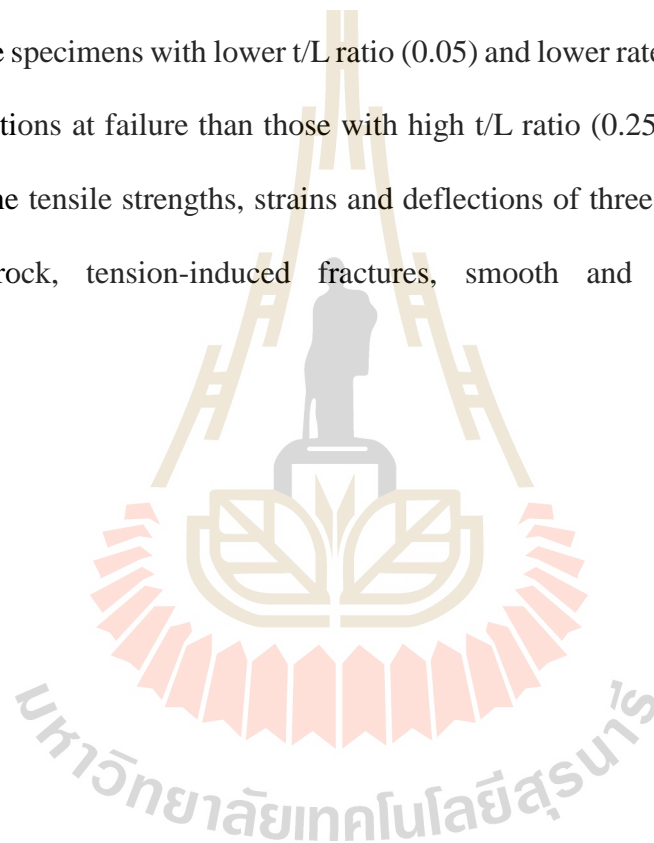


Table 4.2 Some post-test specimens from three point bending testing.

t/L ratios	Surface conditions	Loading rate (MPa/min)			
		1	0.1	0.01	0.001
0.25	Intact rock				
0.13	Roughness				
	Smooth				
	Smooth-Slip				
0.08	Smooth				
	Smooth-Slip				
0.06	Smooth				
	Smooth-Slip				
0.05	Smooth				
	Smooth-Slip				

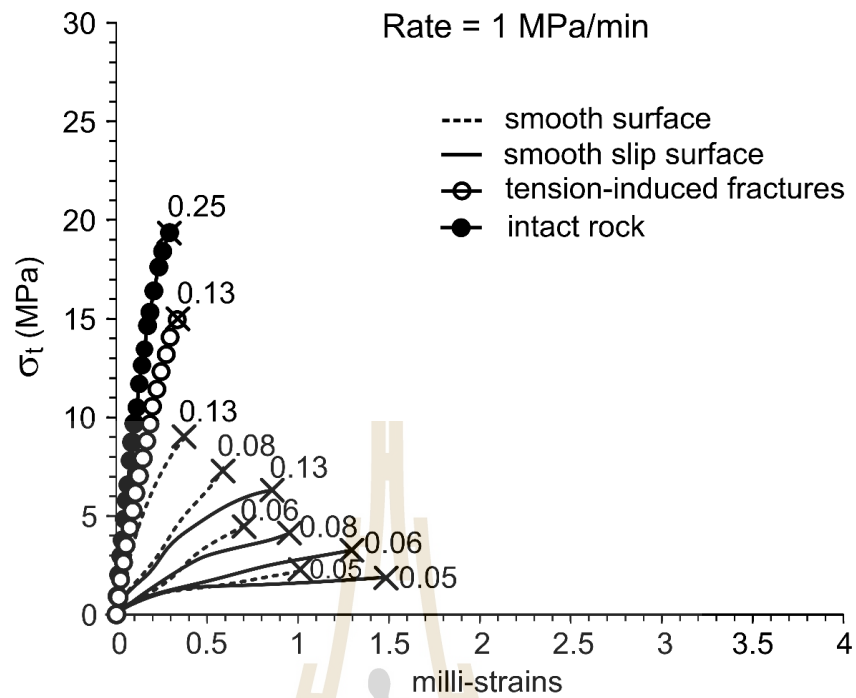


Figure 4.6 Tensile stress-strain curves for loading rate of 1 MPa/min.

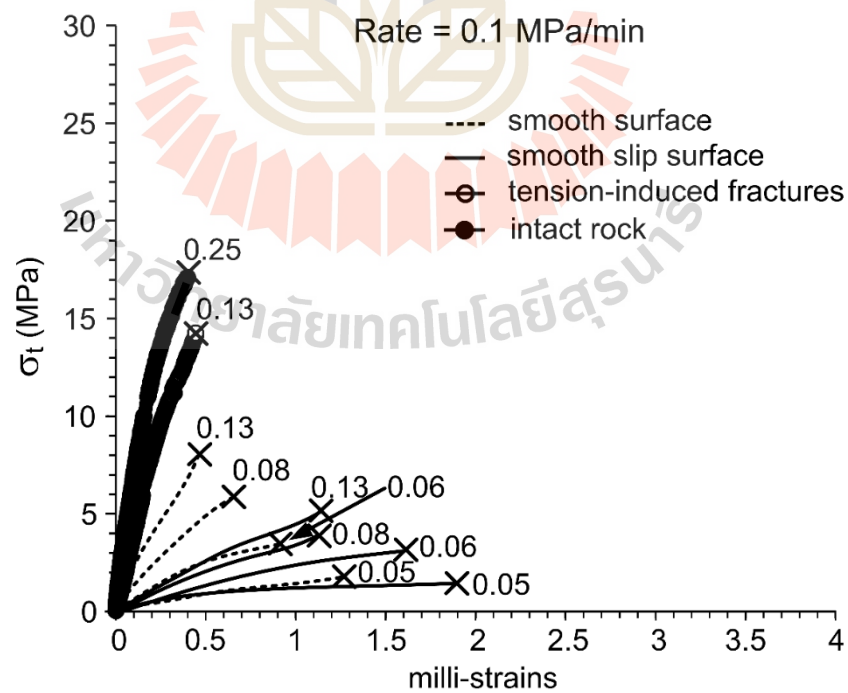


Figure 4.7 Tensile stress-strain curves for loading rate of 0.1 MPa/min.

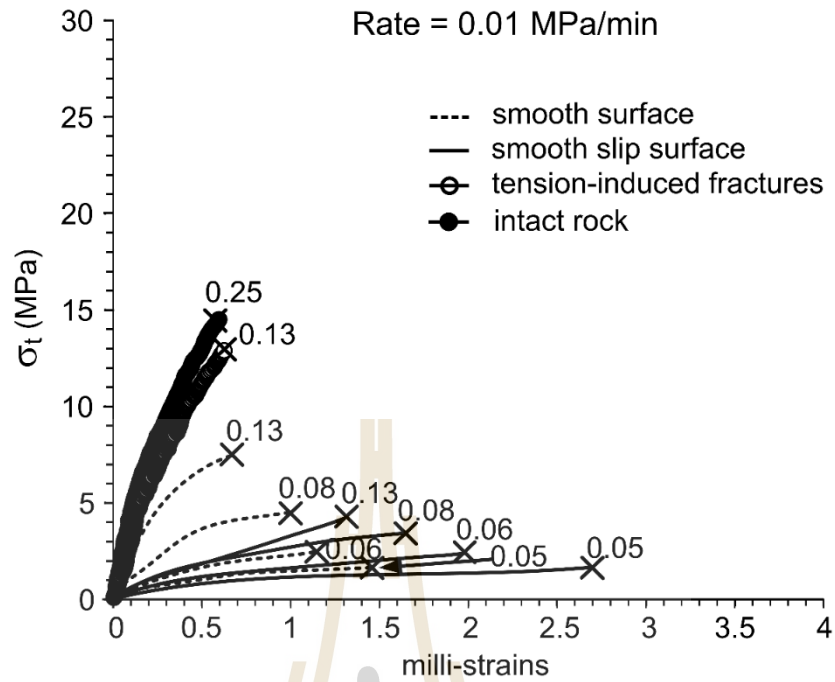


Figure 4.8 Tensile stress-strain curves for loading rate of 0.01 MPa/min.

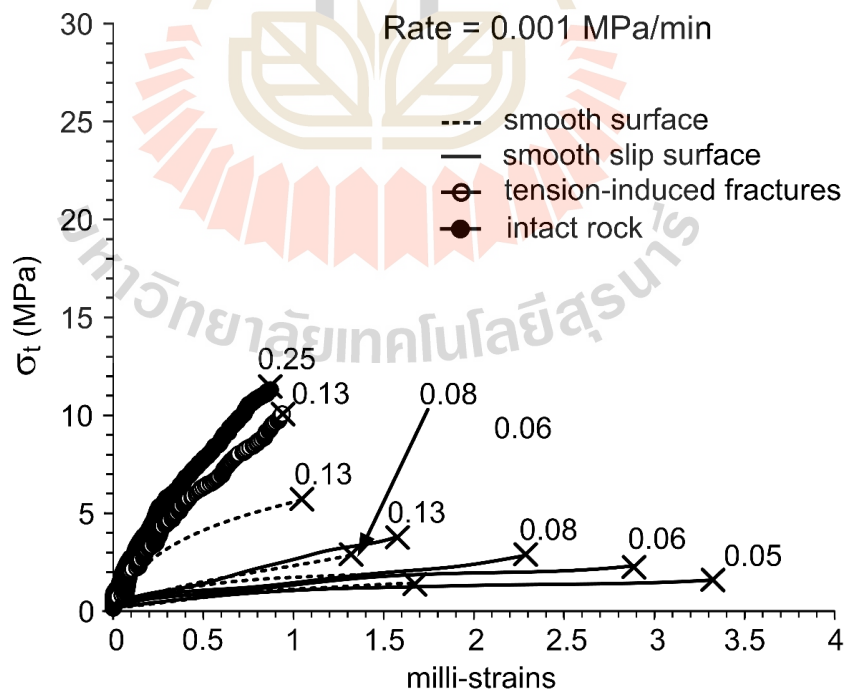


Figure 4.9 Tensile stress-strain curves for loading rate of 0.001 MPa/min.



Figure 4.10 Failure most occur in the lowest slab on three-point bending test.

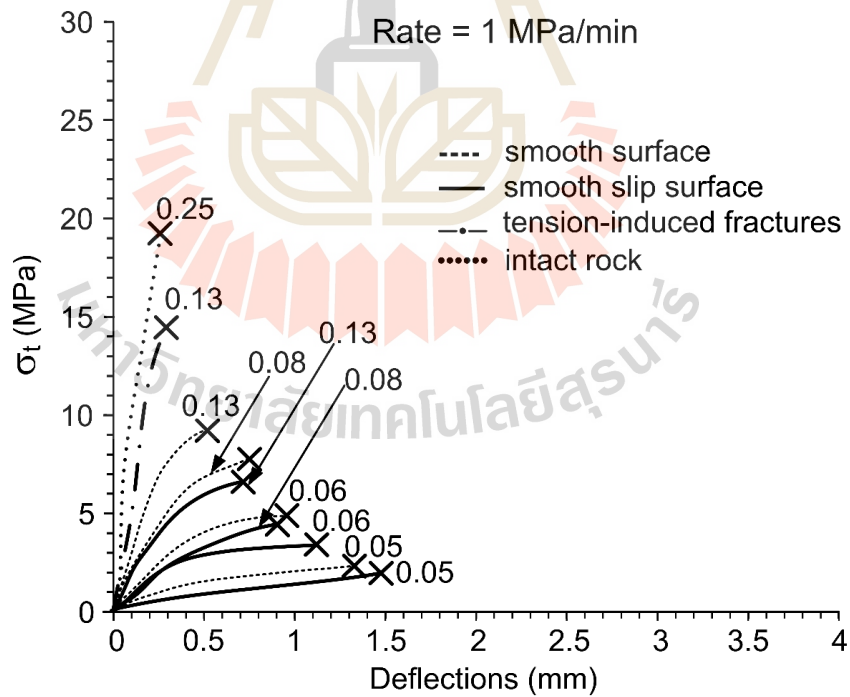


Figure 4.11 Tensile stress-deflection curves for loading rate of 1 MPa/min.

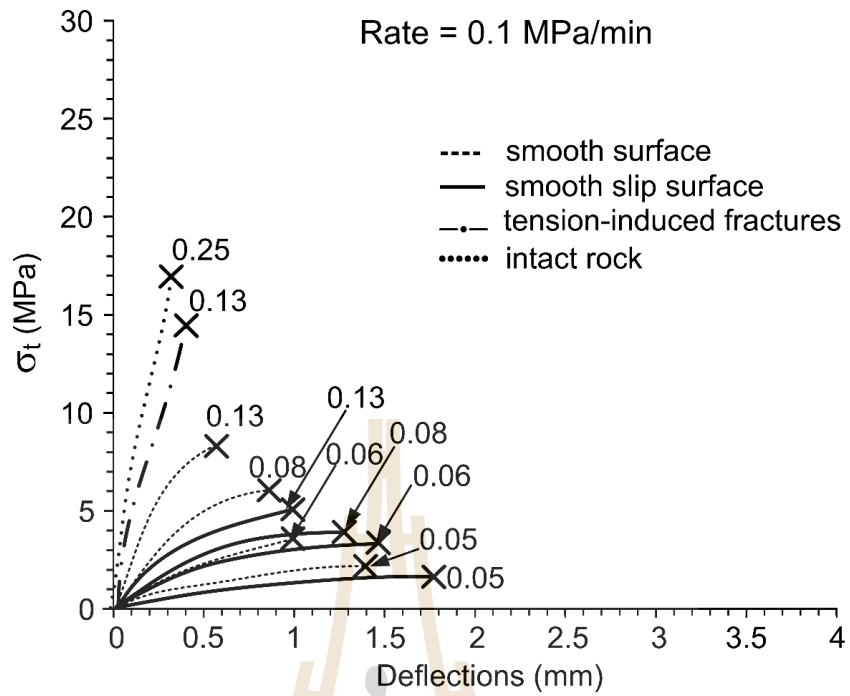


Figure 4.12 Tensile stress-deflection curves for loading rate of 0.1 MPa/min.

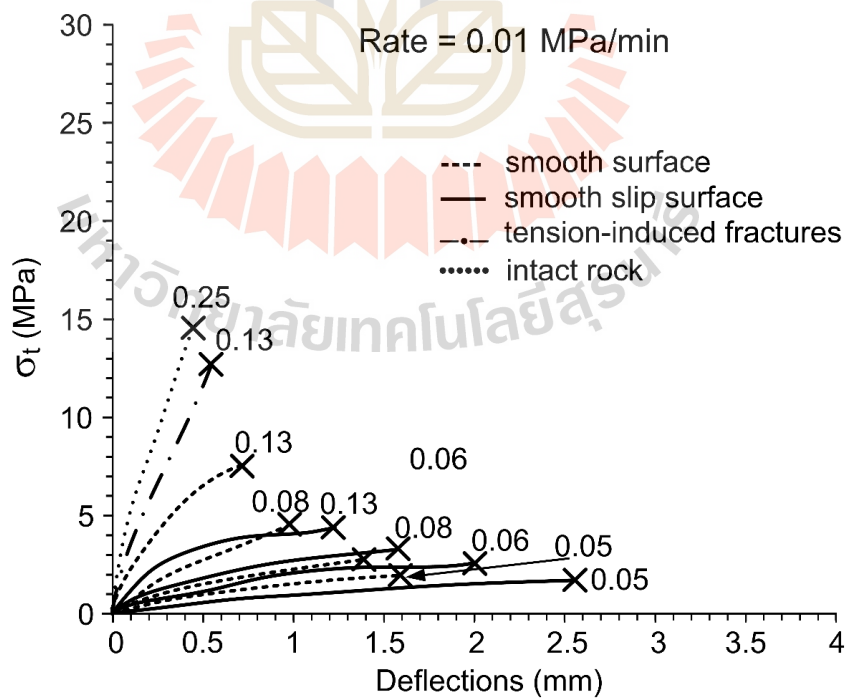


Figure 4.13 Tensile stress-deflection curves for loading rate of 0.01 MPa/min.

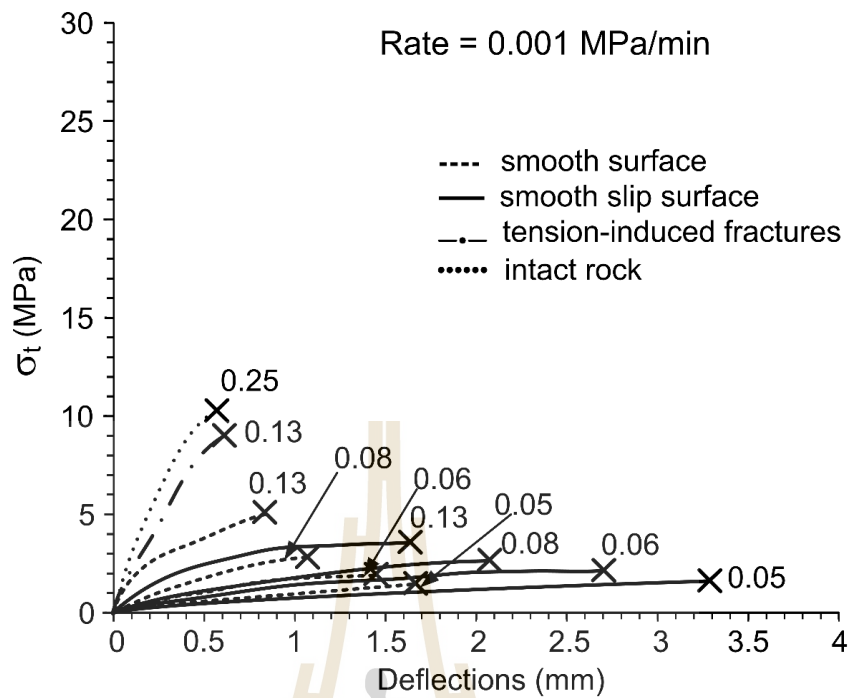


Figure 4.14 Tensile stress-deflection curves for loading rate of 0.001 MPa/min.

Table 4.3 Test results of three-point bending test on intact rock ($t/L=0.25$) and tension-induced fractures ($t/L=0.13$).

Loading rate (MPa/min)	t/L ratios	σ_t (MPa)	ϵ (milli-strains)	Deflections (mm)
1	0.25	19.36	0.29	0.22
0.1		17.05	0.39	0.32
0.01		14.37	0.59	0.41
0.001		11.03	0.87	0.45
1	0.13	14.90	0.33	0.29
0.1		14.20	0.44	0.39
0.01		12.74	0.62	0.51
0.001		11.82	0.94	0.61

Table 4.4 Test results of three-point bending test on smooth and smooth-slip surface.

Loading rate (MPa/min)	t/L ratios	Smooth surface			Smooth-slip surface		
		σ_t (MPa)	ε (10^{-3})	Deflections (mm)	σ_t (MPa)	ε (10^{-3})	Deflections (mm)
1	0.13	8.90	0.38	0.56	6.31	0.87	0.70
	0.08	7.51	0.58	0.74	4.07	0.98	0.90
	0.06	4.64	0.70	0.94	3.14	1.30	1.12
	0.05	2.08	1.00	1.31	1.78	1.49	1.47
0.1	0.13	8.08	0.58	0.68	5.05	1.12	0.98
	0.08	5.77	0.75	0.84	3.82	1.25	1.25
	0.06	3.34	0.89	1.10	2.97	1.58	1.47
	0.05	1.93	1.21	1.39	1.59	1.87	1.79
0.01	0.13	7.23	0.75	0.72	3.99	1.30	1.12
	0.08	4.29	0.98	0.92	3.22	1.65	1.45
	0.06	2.46	1.12	1.24	2.29	1.98	1.84
	0.05	1.65	1.44	1.46	1.35	2.46	2.35
0.001	0.13	5.36	1.04	0.81	3.55	1.60	1.51
	0.08	2.78	1.25	0.98	2.54	2.28	1.87
	0.06	1.83	1.46	1.31	2.03	2.89	2.45
	0.05	1.35	1.66	1.51	1.47	3.31	2.98

CHAPTER V

ANALYSIS OF TEST RESULTS

5.1 Introduction

The purpose of this chapter is to determine the effect of loading rates and t/L ratios on the tensile elastic and strength parameters of the specimens. This is to gain an understanding of the behavior of the roof strata immediately above the openings. The strain energy density criterion is also applied here to describe both rock strength and deformation. The results obtained from the smooth surface, smooth-slip surface and roughness surface specimens are compared.

5.2 Tensile strength criterion

The tensile strengths ($\sigma_{t,f}$) are plotted as a function of t/L ratios in Figure 5.1. The tensile strengths under different t/L ratios for both smooth and smooth slip surfaces can be represented by a power equation (Figure 5.1):

$$\sigma_{t,f} = \alpha(t/L)^\beta \quad (5.1)$$

where α and β are empirical constants. Their numerical values are given in Figure 5.1. Regressions analysis by using SPSS software is performed to determine the above empirical constants from the test data. Figure 5.1 compares the test data with the predictions from Eq. (5.1). Good correlations are obtained ($R^2 > 0.9$). Note that the exponent β for the smooth and smooth-slip surfaces tend to be independent of stress rate.

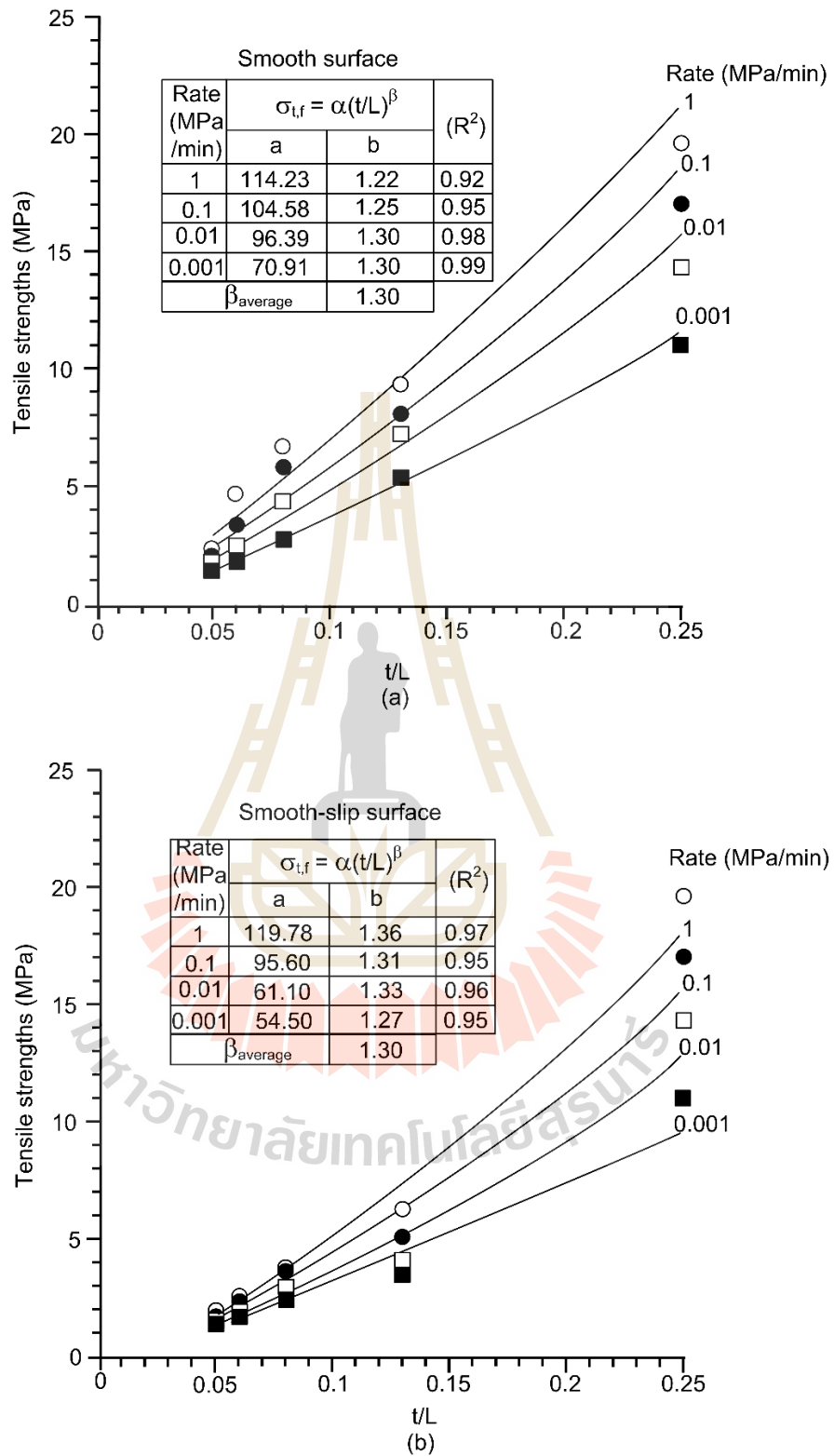


Figure 5.1 Tensile strengths ($\sigma_{t,f}$) as a function of various t/L ratios under various of loading rates for smooth surface (a) and smooth-slip surface (b).

The multiplier α decreases with the stress rate (σ_R), which can be described by a logarithmic equation (Figure 5.2):

$$\alpha = \kappa \ln(\sigma_R) + \omega \quad (5.2)$$

where κ and ω are empirical constants. Substituting Eq. (5.2) into (5.1) the tensile strength under different stress rates and t/L ratios can be represented by:

$$\sigma_{t,f} = [\kappa \ln(\sigma_R) + \omega](t/L)^\beta \quad (5.3)$$

The constant κ is equals to 6 MPa for the smooth surfaces, and 10 MPa for the smooth-slip surfaces. The constants ω and β are 117 and 1.3 MPa, respectively.

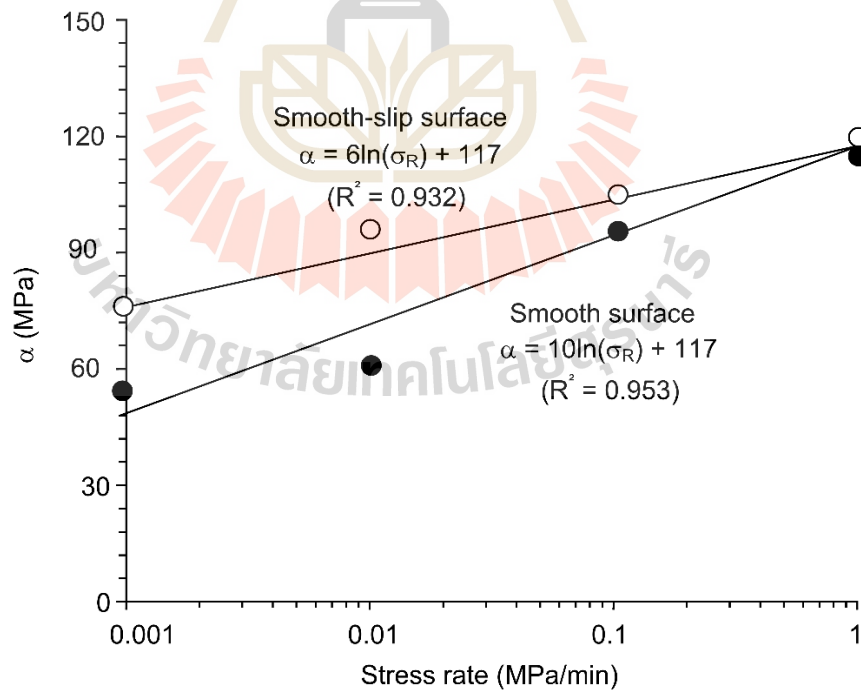


Figure 5.2 Constant α as a function of stress rate (σ_R).

The tensile strengths are plotted as a function of joint frequencies (J.F joints/m), as shown in Figure 5.3. They can be represented by an exponential equation (Figure 5.3):

$$\sigma_{t,f} = \alpha^* e^{-\beta^*(J.F)} \quad (5.4)$$

where α^* and β^* are empirical constants. Regressions analysis is performed to determine these constants from the test data. Figure 5.3 shows the predicted tensile strengths under various loading rates. Good correlations are obtained ($R^2 > 0.9$). The constant β^* for smooth and smooth-slip surfaces tends to be independent of the stress rates, which equals to 0.022 MPa.

The constant α^* represents the tensile strengths at failure when the constant β is zero. It can be described by a logarithmic equation (Figure 5.4):

$$\alpha^* = \kappa^* \ln(\sigma_R) + \omega^* \quad (5.5)$$

where κ^* and ω^* are empirical constants. Substituting Eqs. (5.5) into (5.4) the tensile strength under different stress rates (σ_R) and joint frequencies (joints/m) can be obtained, as follows:

$$\sigma_{t,f} = (\kappa^* \ln(\sigma_R) + \omega^*) (e^{-\beta^*(J.F)}) \quad (5.6)$$

The κ^* and ω^* equal to 1.04 and 21.13 MPa for the smooth surfaces, and 1.23 and 18.1 MPa for smooth-slip surfaces.

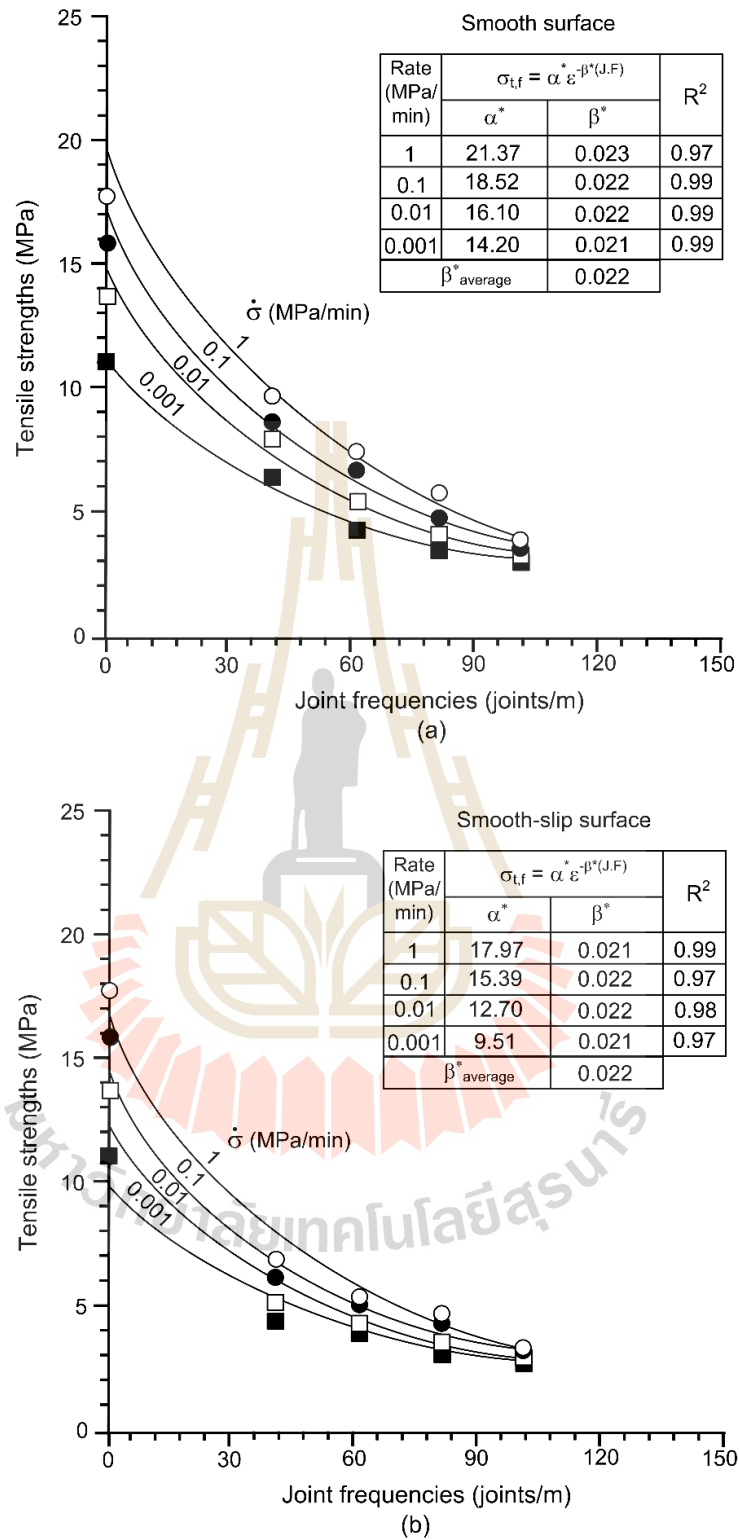


Figure 5.3 Tensile strengths ($\sigma_{t,f}$) as a function for joint frequencies under various of loading rates for smooth surface (a) and smooth-slip surface (b).

5.3 Tensile elastic modulus

The tensile elastic moduli of the specimens are determined from the tangent of the stress-strain curves at about 50% of the failure stress. In this study, assuming that the sandstone specimen is isotropic, and that the point where the crack is induced is under uniaxial stress condition, the elastic modulus (E) can be calculated from the slope of linear relation of the curves. The calculated elastic modulus tends to be dependent of the t/L ratios and loading rates, as shown in Figure 5.5. The results indicate that the elastic moduli increase with increasing t/L ratios and loading rate. This is true for both surface conditions. The results obtained from tension-induced fractures show the higher elastic modulus than those of the smooth and smooth-slip surfaces. This is probably due to the difference of the friction at the interfaces. The intact rock specimen shows the highest elastic moduli. The increase of the elastic modulus with the loading rates ($\dot{\sigma}$) can be represented by:

$$E_t = A \ln(\dot{\sigma}) + B \quad (5.7)$$

where A and B are empirical constants which can be obtained from the regression analysis, as shown as Table 5.1.

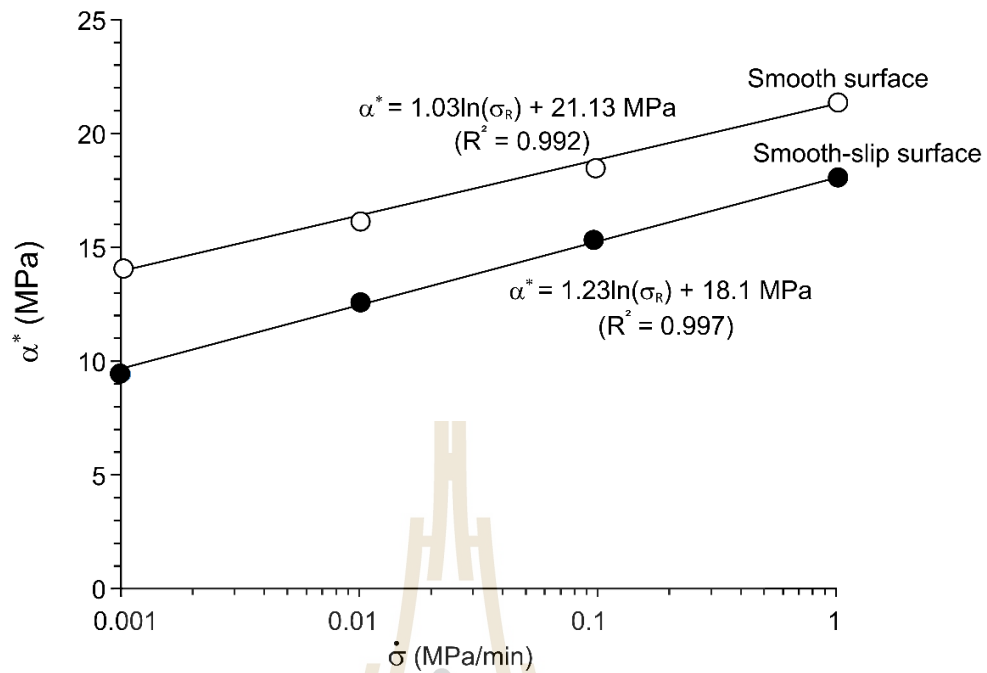


Figure 5.4 Constant α^* as a function of stress rate (σ_R).

Figure 5.5 shows that the elastic moduli are sensitive to the loading rates, particularly where t/L ratios are greater than 0.05. This agrees with the test results obtained from Shabanimshcool and Li (2015) who find that the Young's modulus of rock beam increases with the beam thickness. The loading rates have smaller effect on the elastic modulus when t/L ratio are less than 0.08. This maybe because there are more free surfaces, and hence the specimens can deform more easily.

The constants A and B with different t/L ratios can be described by a logarithmic equation:

$$A = \rho \ln(t/L) + \psi \quad (5.8)$$

$$B = \gamma \ln(t/L) + \eta \quad (5.9)$$

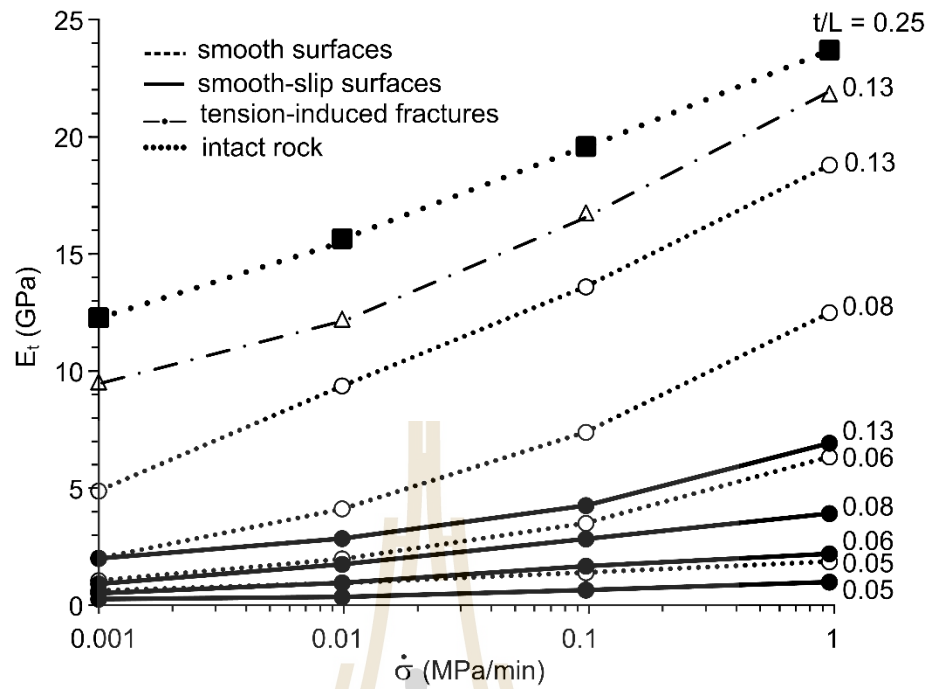


Figure 5.5 Elastic modulus as a function of loading rate ($\dot{\sigma}$) and t/L ratios.

Table 5.1 Empirical constants A and B.

$E_t = A \ln(\dot{\sigma}) + B$				
t/L ratios	surface conditions	A	B	R^2
0.25	Intact rock	1.69	24.13	0.99
0.13	tension-induced fractures	1.83	21.85	0.98
0.13	smooth	2.03	19.06	1
	smooth-slip	0.72	6.72	0.93
0.08	smooth	1.53	12.09	0.96
	smooth-slip	0.45	4.11	1
0.06	smooth	0.77	6.11	0.94
	smooth-slip	0.26	2.42	0.99
0.05	smooth	0.18	2.04	0.99
	smooth-slip	0.11	1.14	0.95

where ρ , ψ , γ and η are empirical constants for the smooth surfaces. They equals to 1.89, 6.04, 17.69 and 55.70 MPa, and for the smooth-slip surfaces equal to 0.63, 2.02, 5.78 and 18.59 MPa. Good correlations are obtained ($R^2 > 0.9$)

Substituting Eqs. (5.8) and (5.9) into Eq. (5.7) the elastic moduli (E_t) as a function of t/L ratios for the smooth and smooth-slip surfaces can be obtained, as shown in Figure 5.6.

$$E_t = [\alpha' (t/L) + \beta'] \ln(\sigma_R) + [\kappa' \ln(t/L) + \omega'] \quad (5.10)$$

where α' , β' , κ' and ω' are empirical constants. For the smooth surface they equals to 1.89, 6.04, 17.69 and 55.70 MPa, and for the smooth-slip surfaces, equal to 0.63, 2.02, 5.78 and 18.59 MPa. Good correlations are obtained ($R^2 > 0.90$). Table 5.2 summarizes the elastic moduli, loading rate, and t/L ratios for different tested surfaces.

5.4 Strain energy density criterion

The strain energy density principle is applied here to describe the rock strength and deformability under different t/L ratios and loading rates. The strain energy at failure (W) can be calculated from the tensile strength and elastic modulus for each rock specimen using the following equation (Jaeger, et al., 2007):

$$W = 1/2(\varepsilon_{t,f} \cdot \sigma_{t,f}) \quad (5.11)$$

where $\varepsilon_{t,f}$ is the maximum tensile strain, and $\sigma_{t,f}$ is the tensile strength.

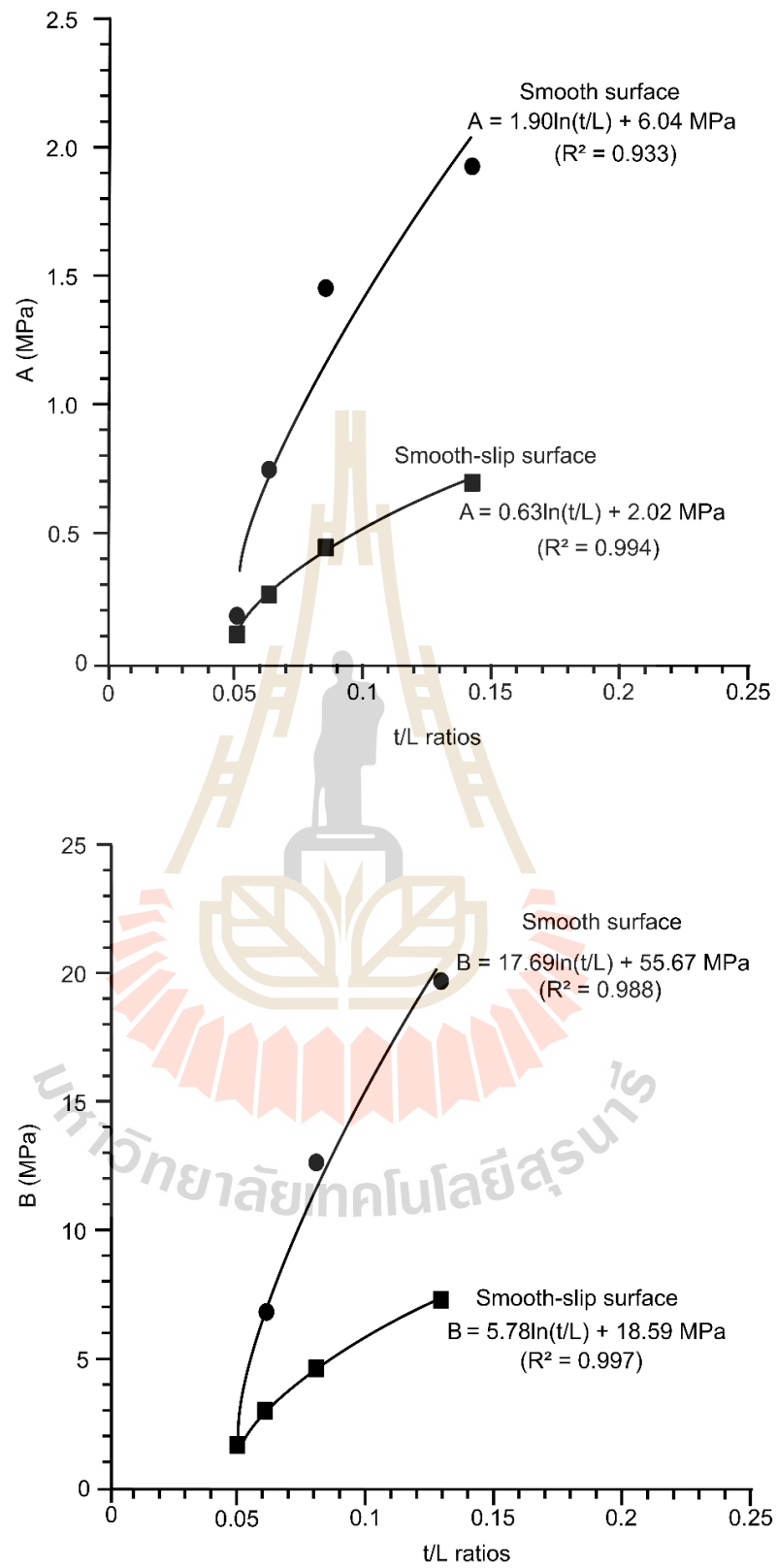


Figure 5.6 Constant A and B as a function of the t/L ratios.

Table 5.2 Elastic moduli, loading rate and t/L ratios for different friction conditions.

t/L ratios	Conditions	($\dot{\sigma}$) (MPa/min)	E_t (GPa)
0.25	Intact rock	1	24.30
		0.1	20.13
		0.01	16.16
		0.001	12.67
0.13	Roughness surface	1	14.96
		0.1	14.20
		0.01	12.74
		0.001	11.82
0.13	Smooth surface	1	19.30
		0.1	14.01
		0.01	9.71
		0.001	5.14
	Smooth-slip surface	1	7.22
		0.1	4.51
		0.01	3.08
		0.001	2.22
0.08	Smooth surface	1	12.89
		0.1	7.70
		0.01	4.36
		0.001	2.23
	Smooth-slip surface	1	4.16
		0.1	3.07
		0.01	1.96
		0.001	1.12
0.06	Smooth surface	1	6.63
		0.1	3.74
		0.01	2.19
		0.001	1.26
	Smooth-slip surface	1	2.42
		0.1	1.88
		0.01	1.16
		0.001	0.70
0.05	Smooth surface	1	2.07
		0.1	1.60
		0.01	1.15
		0.001	0.81
	Smooth-slip surface	1	1.20
		0.1	0.85
		0.01	0.55
		0.001	0.44

Table 5.3 summarizes the tensile strengths, maximum strains and total strain energy density for all specimens. From Figure 5.7, it can be concluded that the maximum strain energy density at which the tensile failure occurs tends to be constant regardless the t/L ratios, loading rates and surface conditions.

Table 5.3 Tensile strengths, maximum strains and total strain energy density for all specimens.

t/L ratios	Conditions	Loading rate (MPa/min)	$\sigma_{t,f}$ (MPa)	$\epsilon_{t,f}$ (milli-strains)	W (kPa)
0.25	Intact rock	1	19.4	0.3	2.32
		0.1	17.1	0.4	2.42
		0.01	14.4	0.6	2.39
		0.001	11.0	0.9	2.33
Average \pm SD					2.37 \pm 0.05
0.13	Roughness surface	1	14.90	0.33	2.41
		0.1	14.20	0.44	2.38
		0.01	12.74	0.62	2.38
		0.001	11.82	0.94	2.3
Average \pm SD					2.37 \pm 0.05
0.13	Smooth surface	1	8.90	0.38	2.38
		0.1	8.08	0.58	2.37
		0.01	7.23	0.75	2.36
		0.001	5.36	1.04	2.35
	Smooth-slip surface	1	6.31	0.87	2.36
		0.1	5.05	1.12	2.36
		0.01	3.99	1.30	2.35
		0.001	3.55	1.60	2.35
Average \pm SD					2.36 \pm 0.06

Table 5.3 Tensile strengths and maximum strains, total strain energy density for all specimens (cont.).

t/L ratios	Conditions	Loading rate (MPa/min)	$\sigma_{t,f}$ (MPa)	$\epsilon_{t,f}$ (milli-strains)	W (kPa)
0.08	Smooth surface	1	7.51	0.58	2.41
		0.1	5.77	0.75	2.39
		0.01	4.29	0.98	2.30
		0.001	2.78	1.25	2.24
	Smooth-slip surface	1	4.07	0.98	2.28
		0.1	3.82	1.25	2.28
		0.01	3.22	1.65	2.27
		0.001	2.54	2.28	2.28
Average \pm SD					2.31 \pm 0.06
0.06	Smooth surface	1	4.64	0.70	2.40
		0.1	3.34	0.89	2.38
		0.01	2.46	1.12	2.30
		0.001	1.83	1.46	2.24
	Smooth-slip surface	1	3.14	1.30	2.35
		0.1	2.97	1.58	2.29
		0.01	2.29	1.98	2.26
		0.001	2.03	2.89	2.25
Average \pm SD					2.31 \pm 0.06
0.05	Smooth surface	1	2.08	1.00	2.40
		0.1	1.93	1.21	2.38
		0.01	1.65	1.44	2.29
		0.001	1.35	1.66	2.24
	Smooth-slip surface	1	1.78	1.49	2.34
		0.1	1.59	1.87	2.28
		0.01	1.35	2.46	2.25
		0.001	1.47	3.31	2.25
Average \pm SD					2.30 \pm 0.06

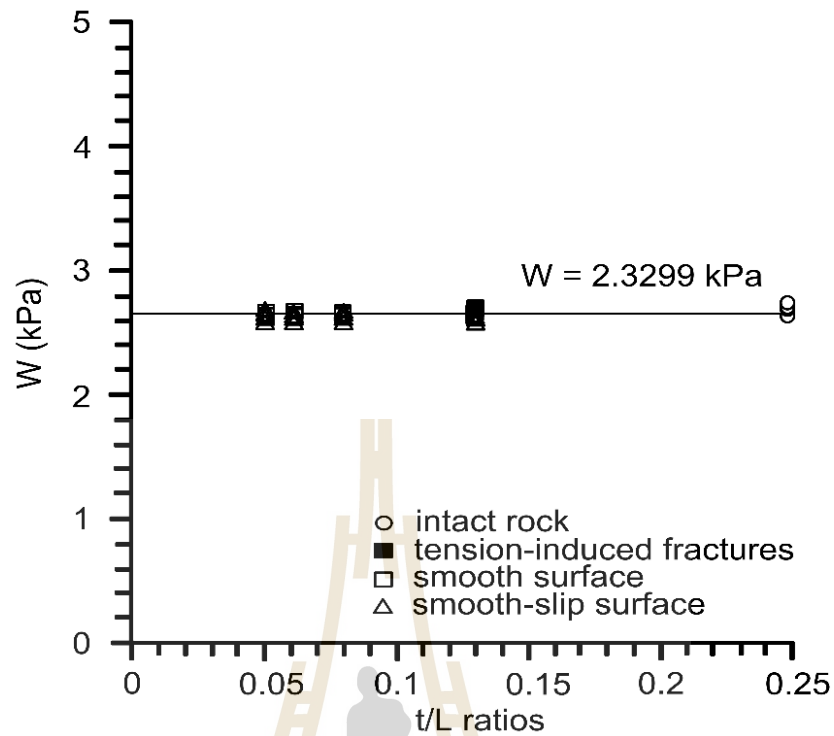


Figure 5.7 Strain energy density as a function of loading rate for different surfaces.

5.5 Numerical analysis

5.5.1 Rock properties for computer modeling

Before performing the computer analysis, physical and mechanical properties of rock samples are specified in the calculation. The major and significant constants in the models are friction angle, cohesion, normal stiffness and shear stiffness of the discontinuities. They are obtained from the direct shear test (in Chapter IV). The discrete element models are constructed to represent various samples and joint spacing as used in the laboratory testing. They are obtained from the shear testing. All computer simulations assume plane stress condition. The corner rounding and the minimum edge length are taken here as 0.001% and 0.002% because the tested Phu

Phan sandstone blocks is rectangular blocks with sharp corners and flat surfaces. Table 5.4 gives summary of the parameters used in numerical simulation.

5.5.2 Numerical Analysis of t/L ratios effects under different surface conditions

The mesh model are shown in Figure 5.8. The model widths is 20 cm. The overall thickness is 5 cm. The applying load (P) of 1 N. UDEC is used in the stratified rock specimens to determine the tensile stresses (Figure 5.9), tensile strains (Figure 5.10) and deflections (Figure 5.11) for t/L ratios from 0.25, 0.13, 0.08, 0.06, and 0.05 at the crack initiation point. Figures 5.12 to 5.14 shown the numerical results indicate that the surface condition have however slightly effect on tensile strengths ($\sigma_{t,1N}$), tensile strains ($\epsilon_{t,1N}$) and deflections (δ) where t/L ratios less than 0.13.

Table 5.4 Summary of the basic joint properties.

Basic the joint properties	Smooth surface	Smooth-slip surface	Tension-induced fractures	Source
Friction angle (Degrees)	25	24	45	This study, Chokchai (2013)
Cohesion (MPa)	0.13	0.09	0.17	This study, Chokchai (2013)
Joint Normal stiffness (GPa/m)	10	10	6.94	Suanprom (2009)
Joint shear stiffness (MPa/m)	1,300	100	9.45	This study, Suanprom (2009)
Density (g/cc)	2,270	2,270	2,270	This study
Elastic modulus (E_t) (GPa)	6.73	6.73	6.73	Klanphumeesri (2010)
Poisson's ratio (ν)	0.05	0.05	0.05	Klanphumeesri (2010)

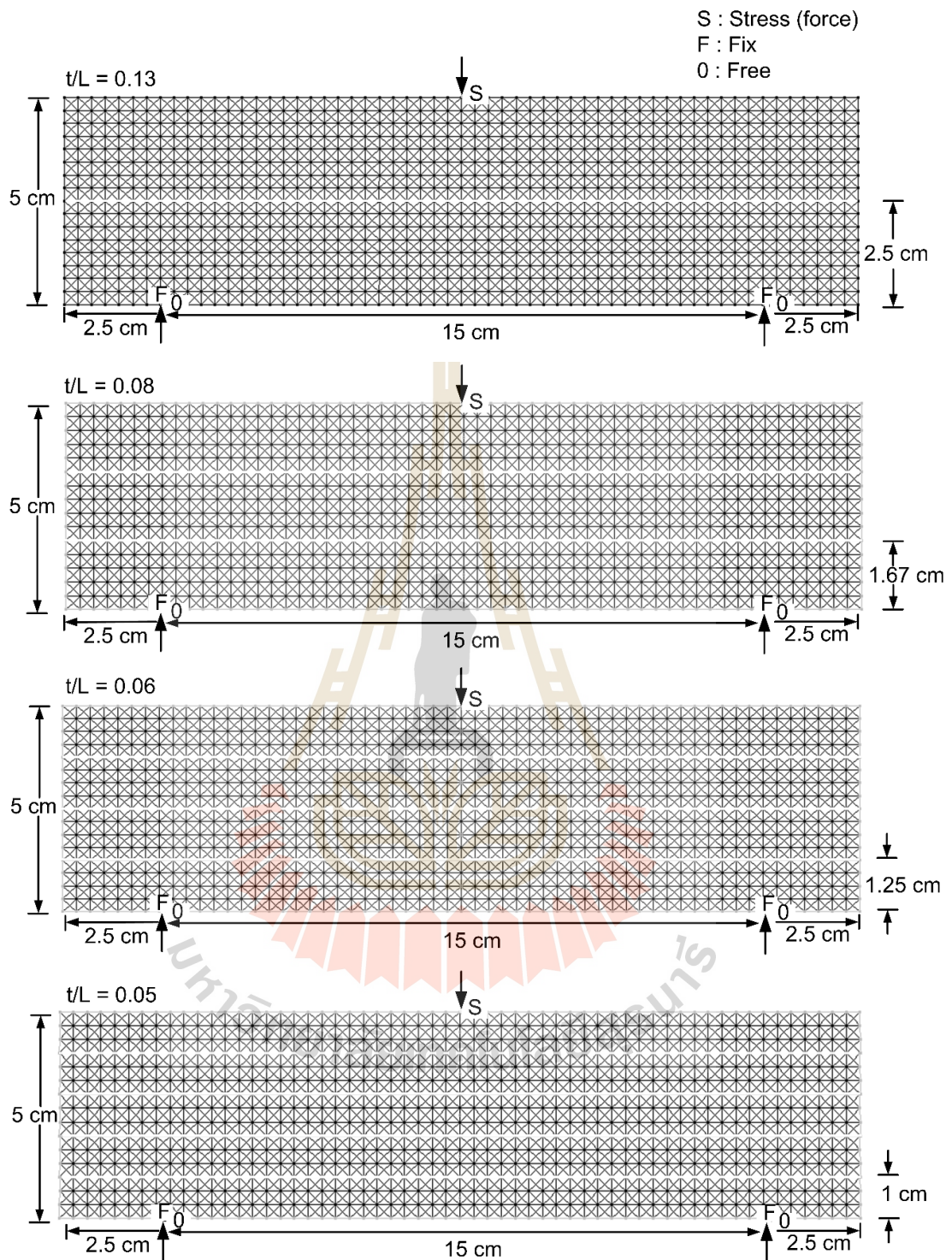


Figure 5.8 Mesh model.

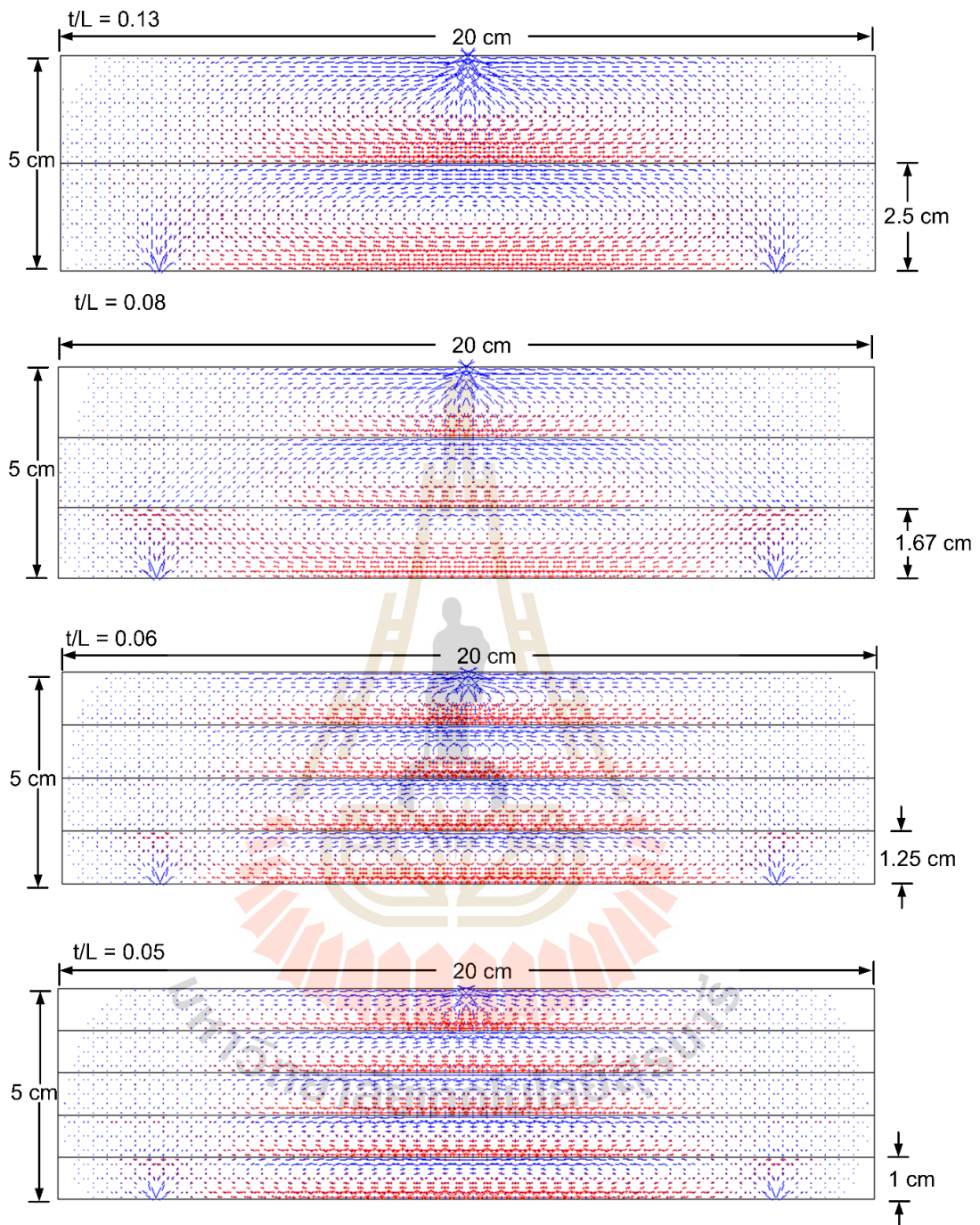


Figure 5.9 Stresses in the model simulation.

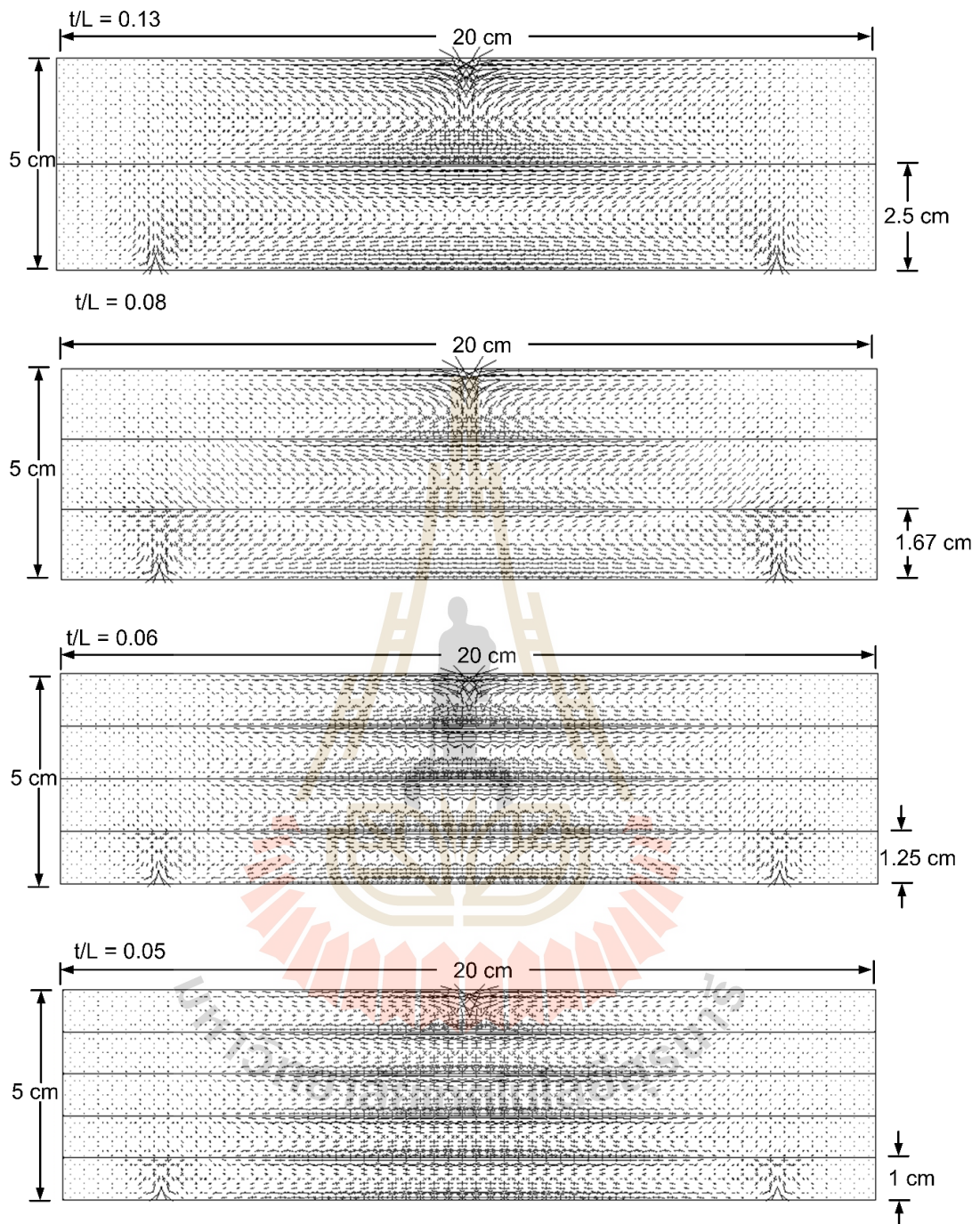


Figure 5.10 Strains in the model simulation.

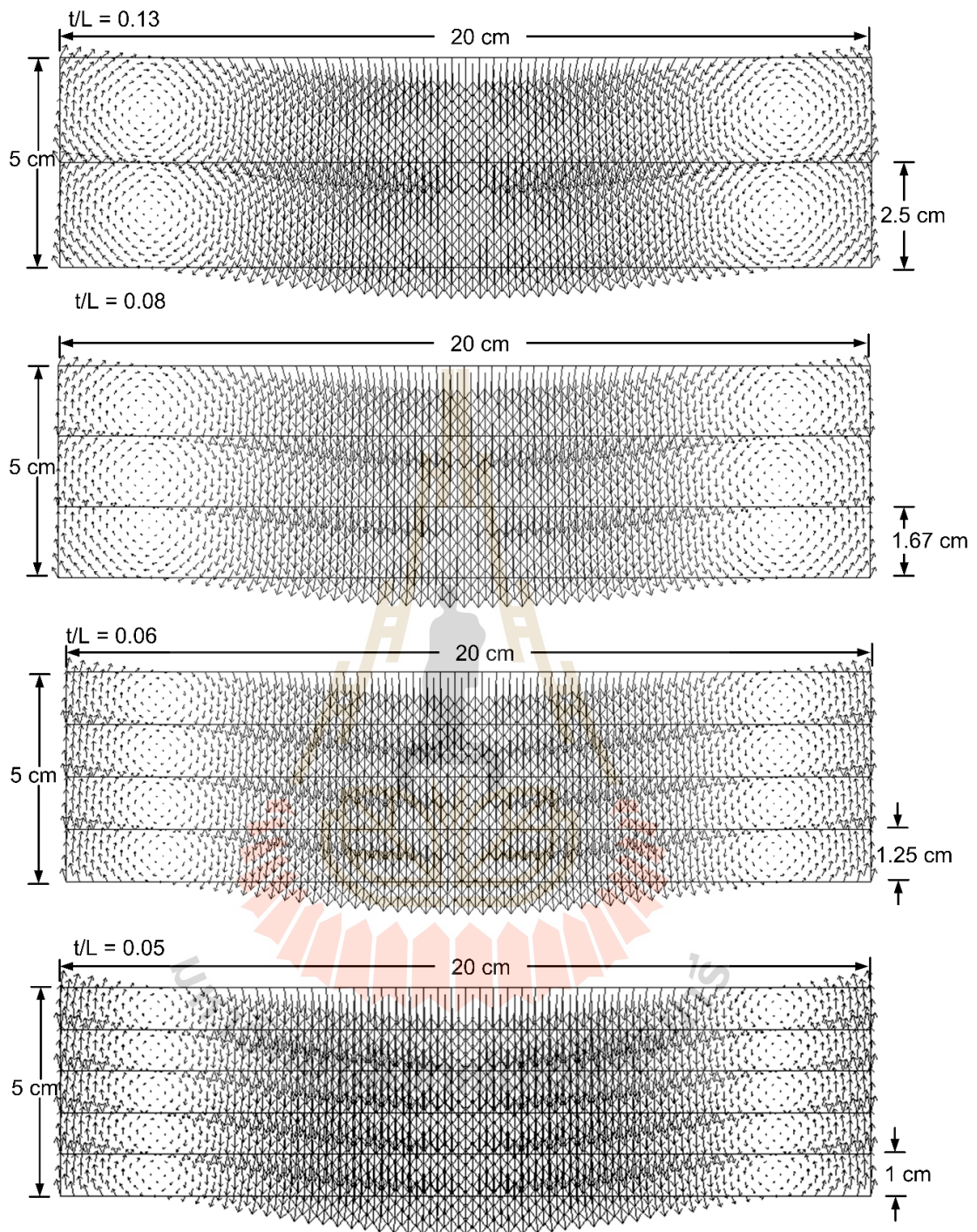


Figure 5.11 Deflections in the model simulation.

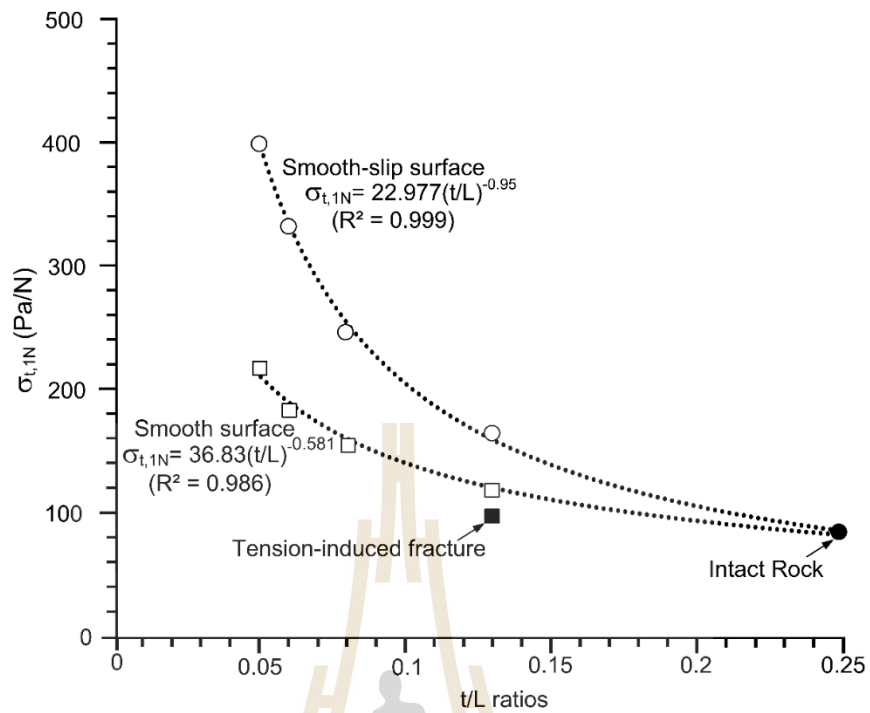


Figure 5.12 Effect tensile stresses under smooth and smooth-slip surface.

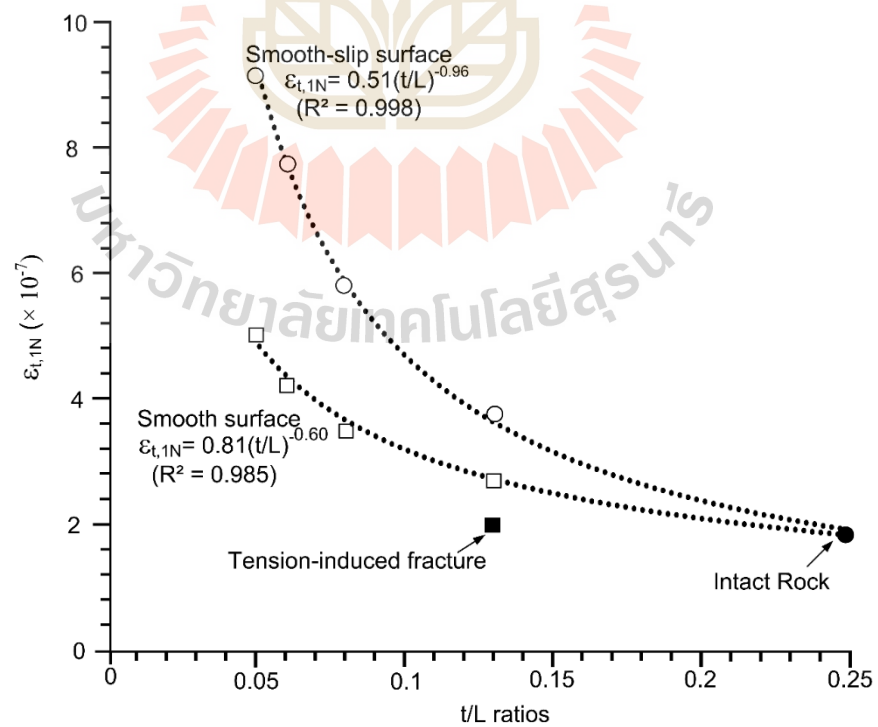


Figure 5.13 Effect tensile strains under smooth and smooth-slip surface.

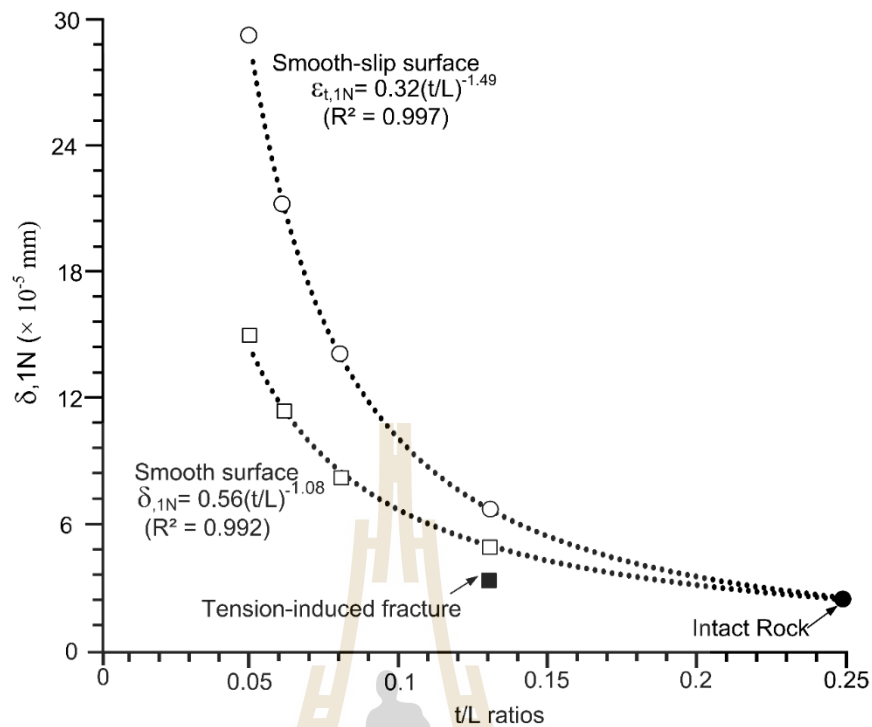


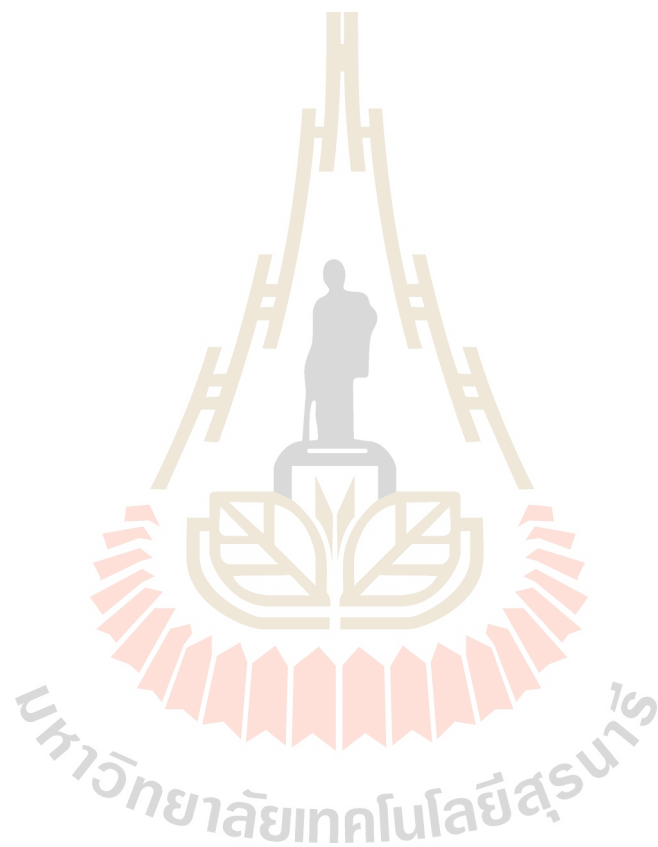
Figure 5.14 Effect deflections under smooth and smooth-slip surface.

5.5.3 Modelling results

The rock block model uses a density of $2,270 \text{ kg/m}^3$. The normal joint stiffness values (K_n) is 10 GPa/m . Figure 5.15 shows the tensile stresses as a function of cohesion, the applying load 1 N (Figure 5.15(a)) and $10,000 \text{ N}$ (Figure 5.15(b)). The results indicate that under same t/L ratios the specimen tensile stresses are independent of the cohesion and Figure 5.16(a) and Figure 5.16(b) the tensile stresses are independent of the friction angle.

Figure 5.17(a) shows the tensile stresses as a function of joint shear stiffness. The joint shear stiffness (K_s) effects become insignificant when its values are below 100 MPa/m . When K_s exceeds $5,000 \text{ MPa/m}$, the stresses of the specimens approach that of the intact specimen regardless the number of layers. The applying load

10,000 N. The joint shear stiffness (K_s) effects become significant when stratified rock specimens as show as Figure 5.17(b). The joint shear stiffness is however the main factor governing the stresses, strains and deflections of the specimens. This holds true for all specimens even with different numbers of rock layers in Table 5.5.



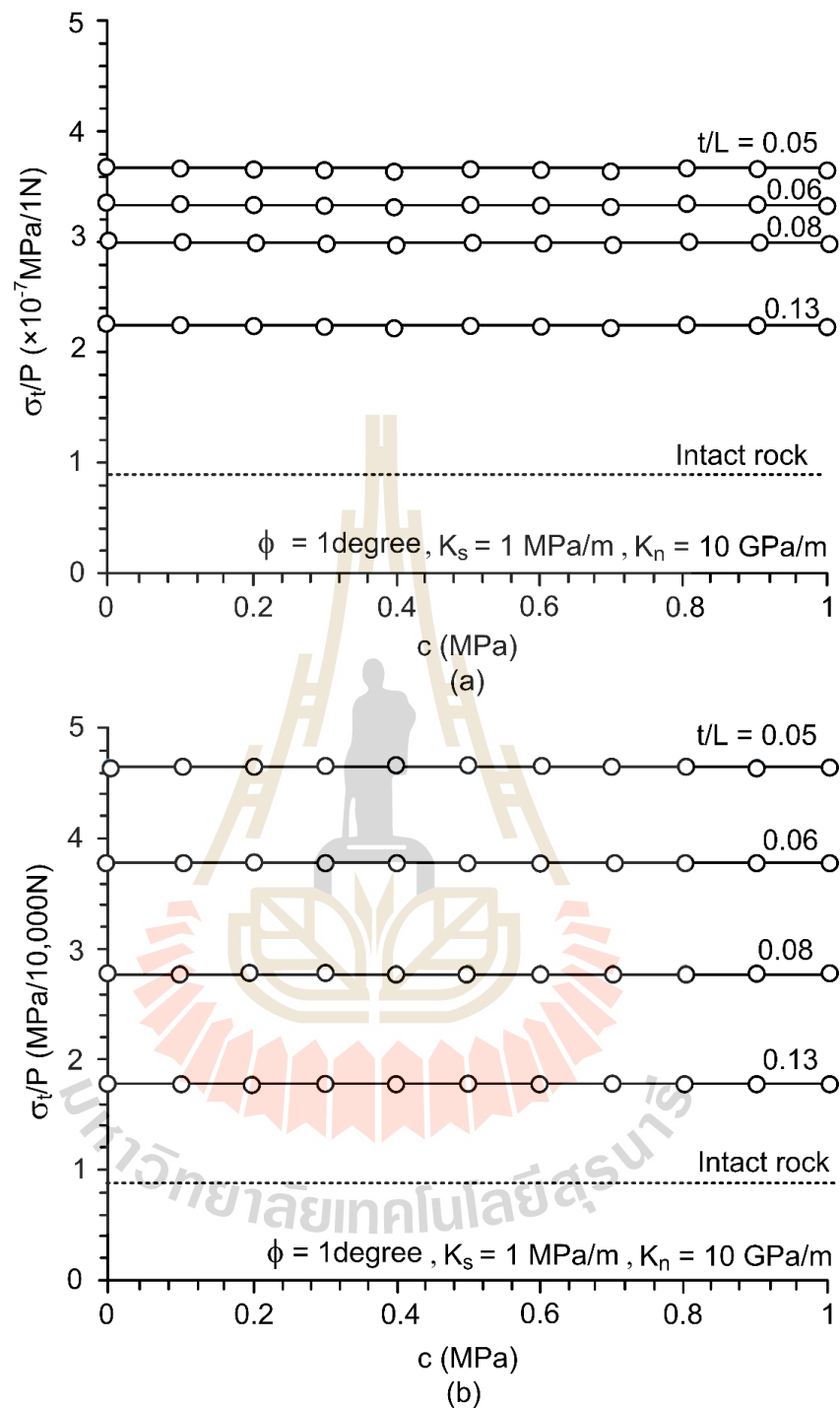


Figure 5.15 Tensile stresses as a function of cohesion.

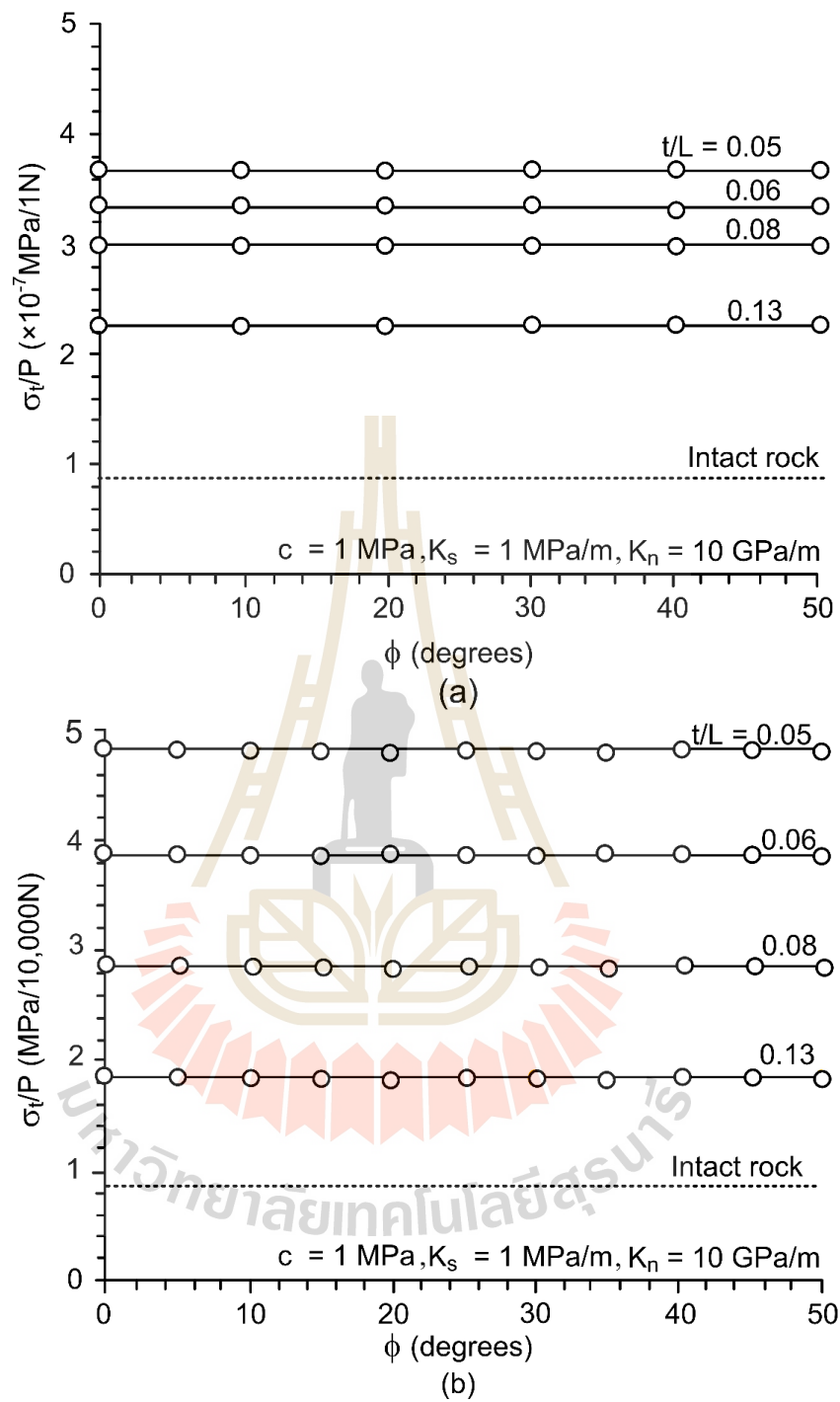


Figure 5.16 Tensile stresses as a function of friction angle.

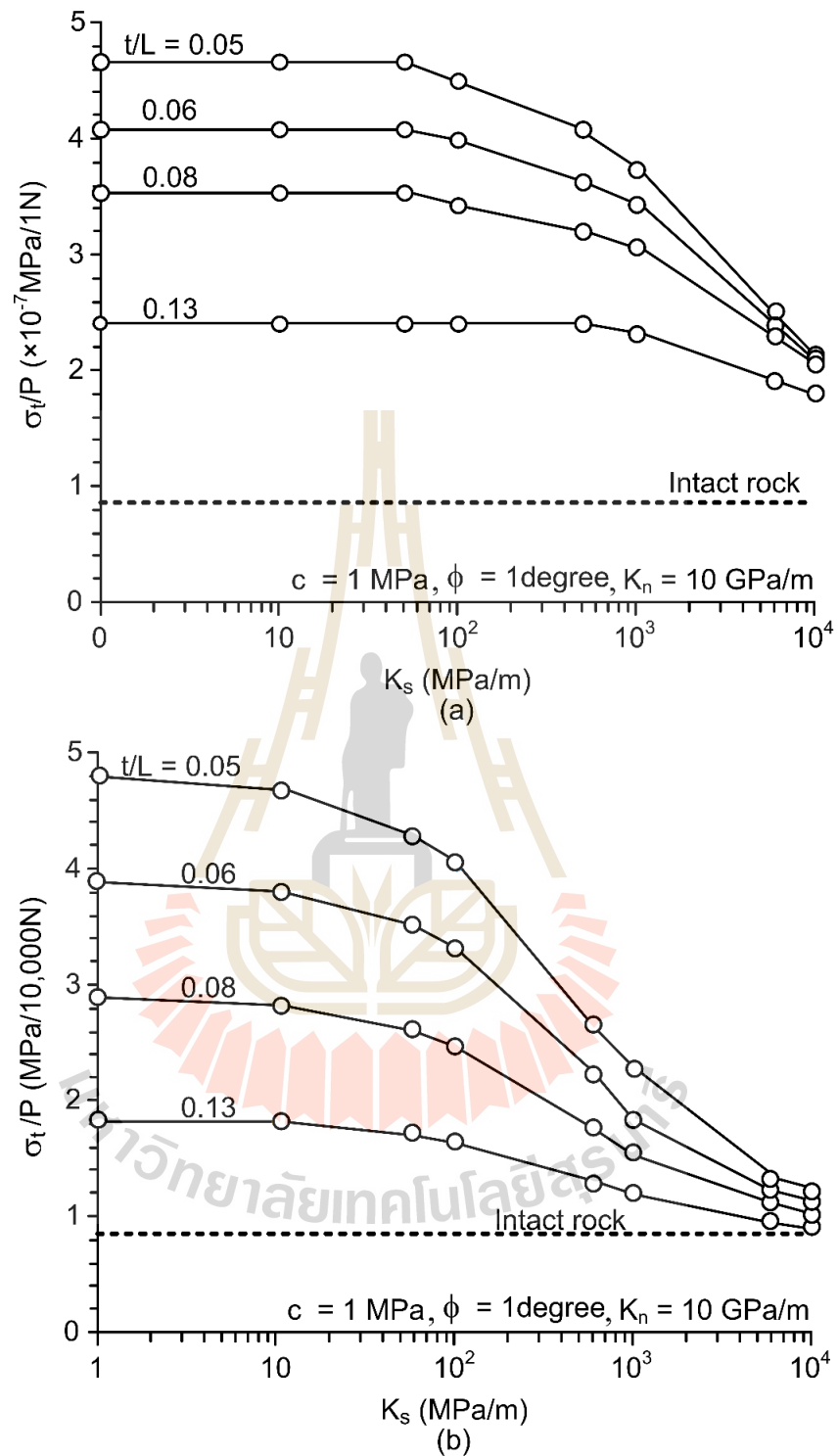


Figure 5.17 Tensile stresses as a function of joint shear stiffness.

Table 5.5 Summary of model results for joint shear stiffness conditions.

t/L ratios	K_s (MPa/m)	σ_t (MPa)	ε_t (10⁻²)	δ (mm)
0.05	1	4.782	1.10	3.609
	10	4.683	1.08	3.52
	50	4.324	1.00	3.189
	100	4.026	0.93	2.92
	500	2.786	0.64	1.908
	1000	2.235	0.52	1.512
	5000	1.346	0.31	0.7794
	10000	1.17	0.27	0.5979
0.06	1	3.886	0.89	2.487
	10	3.8	0.87	2.43
	50	3.546	0.82	2.242
	100	3.287	0.76	2.055
	500	2.285	0.53	1.39
	1000	1.799	0.42	1.111
	5000	1.236	0.28	0.6423
	10000	1.126	0.26	0.516
0.08	1	2.867	0.66	1.494
	10	2.814	0.65	1.463
	50	2.626	0.60	1.363
	100	2.451	0.56	1.269
	500	1.783	0.41	0.9452
	1000	1.509	0.35	0.7893
	5000	1.131	0.26	0.5181
	10000	1.017	0.23	0.4427

Table 5.5 Summary of model results for joint shear stiffness conditions. (cont.)

t/L ratios	K_s (MPa/m)	σ_t (MPa)	ε_t (10⁻²)	δ (mm)
0.13	1	1.838	0.42	0.7378
	10	1.814	0.42	0.7299
	50	1.728	0.40	0.702
	100	1.648	0.38	0.6764
	500	1.301	0.30	0.555
	1000	1.199	0.27	0.494
	5000	0.9748	0.23	0.38
	10000	0.9065	0.21	0.207
0.25	1	0.8493	0.20	0.2
	10	0.8493	0.20	0.2
	50	0.8493	0.20	0.2
	100	0.8493	0.20	0.2
	500	0.8493	0.20	0.2
	1000	0.8493	0.20	0.2
	5000	0.8493	0.20	0.2
	10000	0.8493	0.20	0.2

CHAPTER VI

POTENTIAL APPLICATIONS

6.1 Introduction

The objective of this chapter is to describe potential applications of the test results and the strength criterion presented in the previous chapter. The approach involves the derivation of the relationship between the rock beam deflection and the induced tensile strain at the middle of the underground openings, as well as the comparison of the induced strain energy against the strain energy strength criterion. It is desirable that the beam deflection can be correlated with the test results because it can be measured in the actual opening more easily than the tensile strain at the center of the roof.

6.2 Deflection vs tensile strain

The maximum deflections (δ) at the middle of the specimens can be calculated for 3 different loading configurations based on Pytel and Kiusalaas (2010) as follows:

3-Point Bending:

$$\delta_{\max} = FL^3/48EI \quad (6.1)$$

4-Point Bending:

$$\delta_{\max} = FL^3/28EI \quad (6.2)$$

Uniform Load:

$$\delta_{\max} = WL^4/8EI \quad (6.3)$$

where δ_{\max} is the maximum deflection at the middle of the room. F is load (N), $W=F/L$ (N/m) and E is the elastic modulus of the specimens. The moment of inertia (m^4) and E is the tensile elastic modulus (Pa). The moment of inertia can be determined as:

$$I = bt^3/12 \quad (6.4)$$

where b and t are width and overall thickness of specimens (m). A bending moment is applied to the intact rock. It can be calculated by:

$$M=FL/4 \quad (6.5)$$

where F is load (N), and L is length of the specimens (m). From Equations (6.1) – (6.3) the maximum deflections per length of the specimens ($\delta/L =$ normalized deflections (δ_L)) and the tensile strain (ϵ) can be calculated from:

$$\epsilon = \sigma/E \quad (6.6)$$

$$\sigma = Mc/I \quad (6.7)$$

where I is moment of inertia, M is bending moment and c is half thickness ($t/2$).

The ratios of the stress-to-the normalized deflection can be determined for different loading configurations, as follows:

3-Point Bending:

$$\varepsilon/\delta_L = 6(t/L) \quad (6.8)$$

4-Point Bending:

$$\varepsilon/\delta_L = 3.5(t/L) \quad (6.9)$$

Uniform Load:

$$\varepsilon/\delta_L = t/L \quad (6.10)$$

From Equations (6.8)–(6.10), it can be concluded that the strains-to-normalized deflection ratio is independent of the beam properties. The ratio depends only on the beam dimensions, as shown in Figure 6.1.

Figure 6.1 plots the ε/δ_L ratio for the three loading configurations for $t/L = 0.25$. Figure 6.2 shows the results of the t/L ratio equal to 0.25. Figure 6.2 compares the test results with the analytical solution derived above. For intact rock beam the ε/δ_L ratio agrees well with the analytical solution. The ε/δ_L ratios decrease as the t/L decreases. For the actual in-situ opening underneath the stratified roof the load over the roof applied by the overburden is likely to be uniform rather than three-point or four-point loading. As a result in this application a uniform load is assumed on the roof rock. Figure 6.3 shows how the roof deflection can be determined in the field.

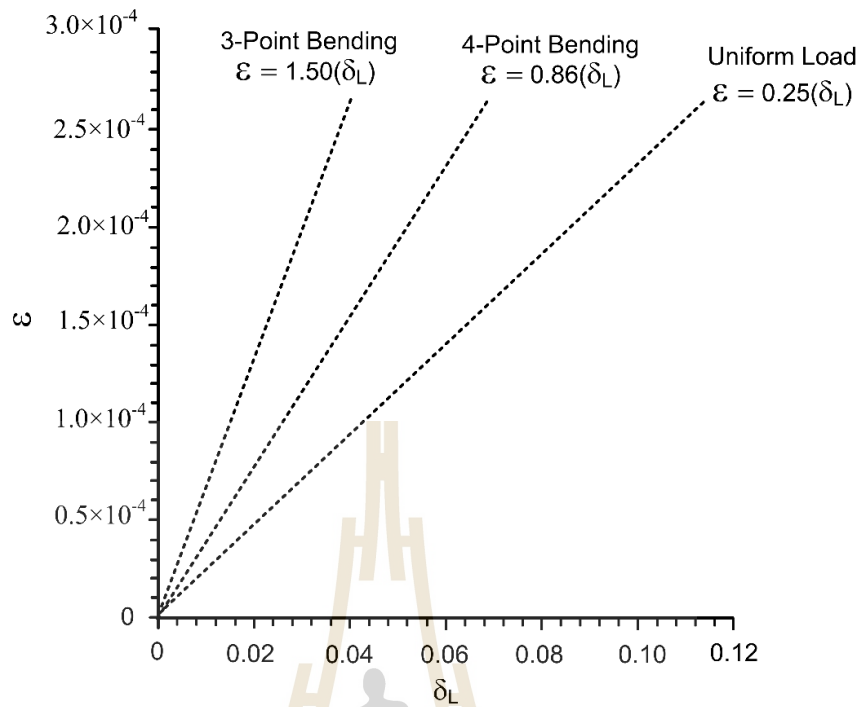


Figure 6.1 Tensile strains as a function normalized deflections (δ_L)

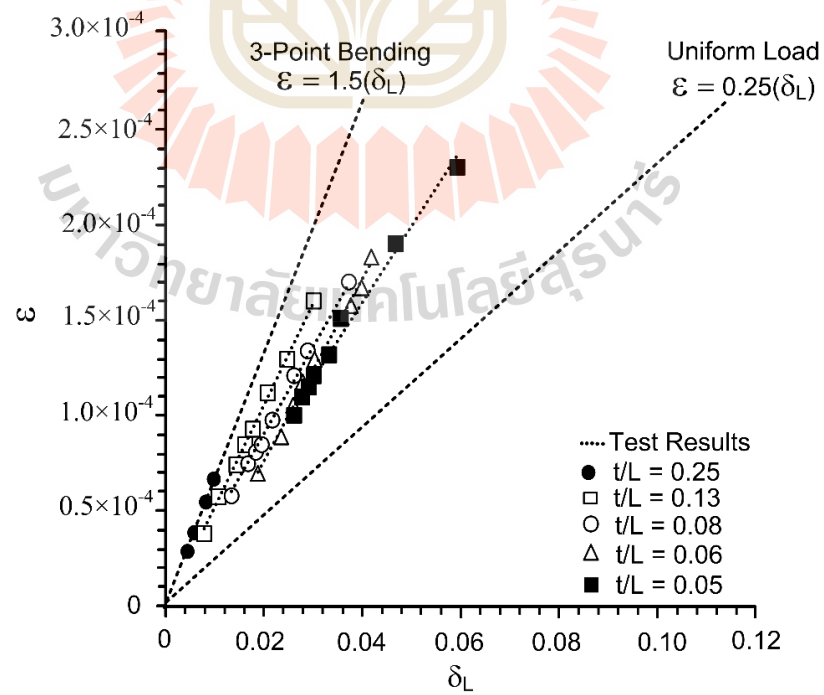


Figure 6.2 ε as a function δ_L . The tensile strains are plotted as positive.

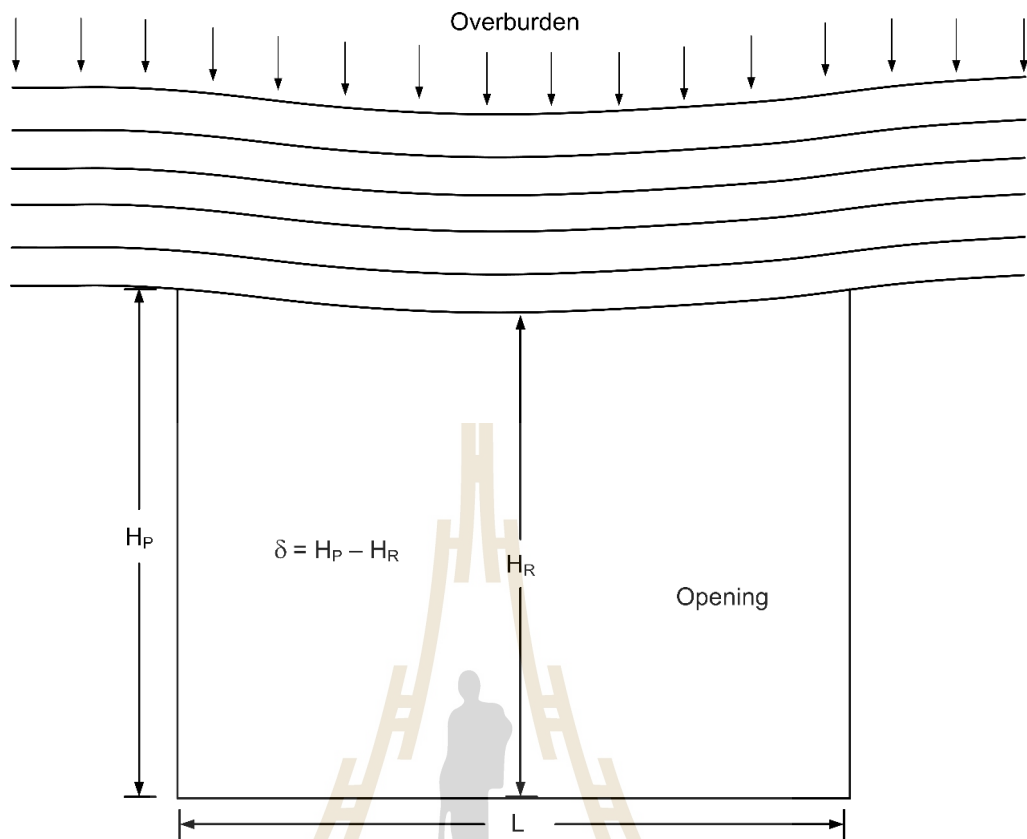


Figure 6.3 Schematic drawing showing how roof deflection can be obtained from actual underground opening.

Figure 6.4 shows the tensile strains as a function of normalized deflection for uniform loading from the overburden. Once the deflection can be measured from the field the tensile strains can be determined from Figure 6.4. The obtained strains and the applied stresses can be used to calculate the strains energy induced at the maximum deflection point. The results can be compared with the strain energy strength criterion developed in the previous chapter.

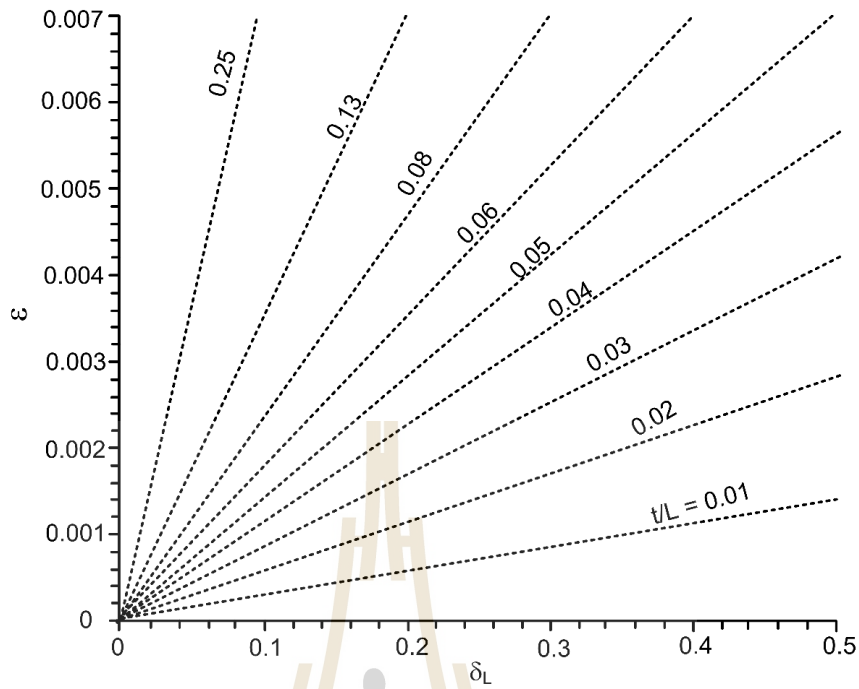


Figure 6.4 Strains as a function normalized deflections (δ_L) for uniform load. Note that the tensile strains are plotted as positive in the figure.

6.3 Distortional strain energy density vs mean strain energy

The strain energy density principle is applied here to describe the tensile strength and deformability under different t/L ratios, loading rates and surface conditions. The distortional strain energy density at failure ($W_{d,f}$) can be calculated from the principal stress deviations and principal strain deviations for each specimen using the following relations (Jaeger et al., 2007):

$$W_{d,f} = (1/2) \cdot (s_1 e_1 + s_2 e_2 + s_3 e_3) \quad (6.11)$$

$$s_1 = \sigma_x - S, \quad s_2 = \sigma_y - S, \quad s_3 = \sigma_z - S \quad (6.12)$$

$$e_1 = \varepsilon_z - e, \quad e_2 = \varepsilon_y - e, \quad e_3 = \varepsilon_z - e \quad (6.13)$$

where s_1, s_2, s_3 and e_1, e_2, e_3 are the principle stress deviations and principle strain deviations at fatigue strengths. Table 6.1 Summary of the principal stress deviations and principal strain deviations. The relation under uniaxial condition; $\sigma_x \neq 0, \sigma_y = 0, \sigma_z$. The distortional strain energy density ($W_{d,f}$) can also be derived as a function of the mean strain energy at failure ($W_{m,f}$) as follows:

$$W_{m,f} = (\sigma_{t,f}^2) / (2 \cdot [E/3(1-2\nu)]) \quad (6.14)$$

$$s = \sigma_x / 3 \quad (6.15)$$

$$e = (\varepsilon_x + \varepsilon_z) / 3 \quad (6.16)$$

$$\varepsilon_z = -\nu \cdot (\varepsilon_x) \quad (6.17)$$

where s is the mean normal stress at dilation at fatigue strengths, e is the mean normal strain, ε_x is the strain and ν is Poisson's ratio under uniaxial tension condition. The Poisson's ratios obtained from direct tensile strength from dog-bone shaped specimens of intact sandstone as those performed by Klanphumeesri and Fuenkajorn (2010).

Figure 6.5 shows as a linear trend of the test data in the $W_d - W_m$ relation which can be best represented by:

$$W_{d,f} = 2.158W_{m,f} \quad (\text{kPa}) \quad (6.18)$$

Table 6.1 Summary of the principal stress deviations and principal strain deviations.

Surface Conditions	t/L	s ₁ (MPa)	s ₂ (MPa)	s ₃ (MPa)	e ₁ (MPa)	e ₃ (MPa)	e ₂ (MPa)
Intact rock	0.25	12.93	-6.47	-6.47	0.20	-0.11	-0.09
		11.40	-5.70	-5.70	0.27	-0.14	-0.12
		9.60	-4.80	-4.80	0.40	-0.22	-0.19
		7.33	-3.67	-3.67	0.59	-0.32	-0.28
Rough	0.13	9.93	-4.97	-4.97	0.23	-0.12	-0.10
		9.47	-4.73	-4.73	0.30	-0.16	-0.14
		8.49	-4.25	-4.25	0.42	-0.23	-0.20
		7.88	-3.94	-3.94	0.64	-0.34	-0.30
Smooth	0.13	5.93	-2.97	-2.97	0.26	-0.14	-0.12
		5.39	-2.69	-2.69	0.40	-0.21	-0.18
		4.82	-2.41	-2.41	0.48	-0.26	-0.22
		3.57	-1.79	-1.79	0.69	-0.37	-0.32
	0.08	5.01	-2.50	-2.50	0.39	-0.21	-0.18
		3.85	-1.92	-1.92	0.51	-0.28	-0.24
		2.86	-1.43	-1.43	0.61	-0.33	-0.28
		1.85	-0.93	-0.93	0.82	-0.44	-0.38
	0.06	3.09	-1.55	-1.55	0.51	-0.27	-0.24
		2.23	-1.11	-1.11	0.67	-0.36	-0.31
		1.64	-0.82	-0.82	0.77	-0.41	-0.36
		1.22	-0.61	-0.61	0.98	-0.53	-0.46
	0.05	1.39	-0.69	-0.69	0.71	-0.38	-0.33
		1.29	-0.64	-0.64	0.85	-0.46	-0.39
		1.10	-0.55	-0.55	0.99	-0.53	-0.46
		0.90	-0.45	-0.45	1.13	-0.61	-0.52
Smooth-slip	0.13	4.21	-2.10	-2.10	0.60	-0.32	-0.28
		3.37	-1.68	-1.68	0.67	-0.36	-0.31
		2.66	-1.33	-1.33	0.89	-0.48	-0.41
		2.37	-1.18	-1.18	1.02	-0.55	-0.47
	0.08	2.71	-1.36	-1.36	0.77	-0.41	-0.35
		2.55	-1.27	-1.27	0.85	-0.46	-0.39
		2.15	-1.07	-1.07	1.08	-0.58	-0.50
		1.69	-0.85	-0.85	1.28	-0.69	-0.59
	0.06	2.09	-1.05	-1.05	0.89	-0.48	-0.41
		1.98	-0.99	-0.99	1.13	-0.60	-0.52
		1.53	-0.76	-0.76	1.35	-0.73	-0.63
		1.35	-0.68	-0.68	1.68	-0.90	-0.78
	0.05	1.19	-0.59	-0.59	1.09	-0.59	-0.51
		1.06	-0.53	-0.53	1.56	-0.84	-0.72
		0.90	-0.45	-0.45	1.98	-1.06	-0.92
		0.98	-0.49	-0.49	2.27	-1.22	-1.05

The $W_{d,f}$ - $W_{m,f}$ criterion explicitly considers both octahedral shear, elastic modulus, Poisson's ratios and stresses at failure, and hence isolate the effect of t/L ratios, stress rates and surface conditions.

Table 6.2 Summary of the distortional strain energy density ($W_{d,f}$) and the mean strain energy at failure ($W_{m,f}$). The criterion can be used to assume the actual stratified roof stability. Rock bolts may be installed to increase the t/L ratios, and hence increase the stability of the roof beams.

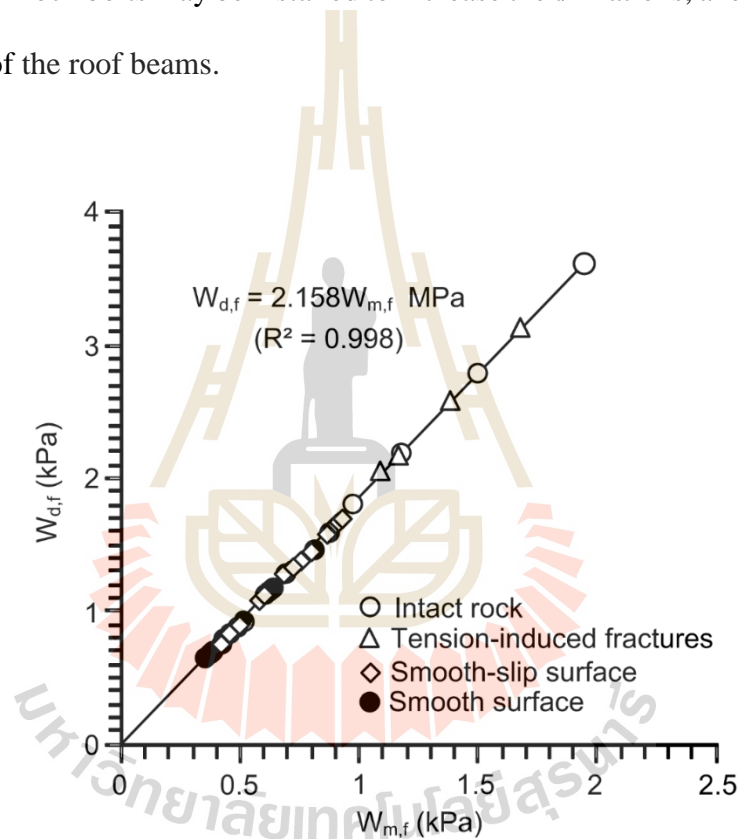


Figure 6.5 Strain energy of distortion at failure ($W_{d,f}$) as function of mean strain energy at failure ($W_{m,f}$).

Table 6.2 Summary of the distortional and mean strain energy density at failure.

Surface Conditions	t/L	ϵ (milli-strains)	σ_x (MPa)	ϵ_z (MPa)	s (MPa)	e (MPa)	$W_{d,f}$ (kPa)	$W_{m,f}$ (kPa)
Intact rock	0.25	0.29	19.40	0.01	6.47	0.09	1.92	0.89
		0.39	17.10	0.02	5.70	0.12	2.28	1.06
		0.59	14.40	0.03	4.80	0.19	2.90	1.35
		0.87	11.00	0.04	3.67	0.28	3.27	1.52
Rough	0.13	0.33	14.90	0.02	4.97	0.10	1.68	0.78
		0.44	14.20	0.02	4.73	0.14	2.13	0.99
		0.62	12.74	0.03	4.25	0.20	2.70	1.25
		0.94	11.82	0.05	3.94	0.30	3.80	1.76
Smooth	0.13	0.38	8.90	0.02	2.97	0.12	1.17	0.54
		0.58	8.08	0.03	2.69	0.18	1.61	0.75
		0.70	7.23	0.04	2.41	0.22	1.73	0.80
		1.00	5.36	0.05	1.79	0.32	1.84	0.85
	0.08	0.58	7.51	0.03	2.50	0.18	1.48	0.69
		0.75	5.77	0.04	1.92	0.24	1.48	0.69
		0.89	4.29	0.04	1.43	0.28	1.31	0.61
		1.21	2.78	0.06	0.93	0.38	1.14	0.53
	0.06	0.75	4.64	0.04	1.55	0.24	1.18	0.55
		0.98	3.34	0.05	1.11	0.31	1.12	0.52
		1.12	2.46	0.06	0.82	0.36	0.94	0.44
		1.44	1.83	0.07	0.61	0.46	0.90	0.42
	0.05	1.04	2.08	0.05	0.69	0.33	0.74	0.34
		1.25	1.93	0.06	0.64	0.39	0.82	0.38
		1.46	1.65	0.07	0.55	0.46	0.82	0.38
		1.66	1.35	0.08	0.45	0.52	0.76	0.35
Smooth-slip	0.13	0.87	6.31	0.04	2.10	0.28	1.88	0.87
		0.98	5.05	0.05	1.68	0.31	1.69	0.78
		1.30	3.99	0.06	1.33	0.41	1.77	0.82
		1.49	3.55	0.07	1.18	0.47	1.81	0.84
	0.08	1.12	4.07	0.06	1.36	0.35	1.56	0.72
		1.25	3.82	0.06	1.27	0.39	1.62	0.75
		1.58	3.22	0.08	1.07	0.50	1.74	0.80
		1.87	2.54	0.09	0.85	0.59	1.63	0.75
	0.06	1.30	3.14	0.06	1.05	0.41	1.39	0.64
		1.65	2.97	0.08	0.99	0.52	1.67	0.77
		1.98	2.29	0.10	0.76	0.63	1.55	0.72
		2.46	2.03	0.12	0.68	0.78	1.71	0.79
	0.05	1.60	1.78	0.08	0.59	0.51	0.97	0.45
		2.28	1.59	0.11	0.53	0.72	1.24	0.57
		2.89	1.35	0.14	0.45	0.92	1.33	0.62
		3.31	1.47	0.17	0.49	1.05	1.66	0.77

CHAPTER VII

DISCUSSIONS AND CONCLUSIONS

7.1 Discussions

This section discusses the key issues relevant to the reliability of the test schemes and the adequacies of the test results. Comparisons of the results and findings from this study with those obtained elsewhere under similar test conditions have also been made.

- A total of 36 specimens have been applied perpendicular to the face of the specimen continuously without eccentricity. The results are believed to be reliable as evidenced by the good correlation coefficients obtained from all proposed equations.
- The post-test specimens obtained from the three-point bending test show that the fractures occur at the center of specimen for all testing. This is because this point is under maximum tensile stresses. This agrees with the experimental results conducted by Obert and Duvall (1967) who propose the solution for the maximum stress (σ_{\max}) values indicating the compression (bottom of beam) or tension (top of beam). This stress is higher than the previous abutment stress, and therefore higher than the rock tensile strength. This leads to subsequent fracturing centered about the mid span as shown by Stimpson and Ahmed (1992). Snyder (1983) considers a laminated rock beam an excavation with a horizontal span by the normal thickness of the single layer under analysis. An elastic beam with no joints and with constant cross section, the compression and tension distributions are symmetrical about the horizontal centre line of the beam.

- For all Phu Phan sandstone specimens the tensile strength (σ_t) and tensile elastic modulus (E_t) is lower than the compressive tensile strength (σ_c) and compressive elastic modulus (E_c). The results indicate that the direct tensile strengths are clearly lower than the Brazilian, ring tensile strengths and 3-point bending. This is suggested by the experimental results by Klanphumeesri and Fuenkajorn (2010)
- The specimens size used in this study are relatively small. Recognizing the size effects on the rock strengths (Jaeger et al., 2007), larger specimens should be used. The strengths obtained here under all test schemes would overestimate the strength of the sandstone under in-situ condition due to the scale effect. Nevertheless, the issue of the size effect would not change the main conclusions drawn here that the tensile strengths decrease when the t/L ratios decrease and tensile strength increases with loading rate.
- The test results in terms of the tensile strength and loading rate agree reasonably well with the related test results on the ring tensile strength test obtained by Wisetsaen et al. (2015) that the tensile strengths of rock increase with the loading rate

7.2 Conclusions

All objectives and requirements of this study have been met. The results of the laboratory testing and analyses can be concluded as follows:

- The friction angle of the smooth and smooth-slip surface (ϕ) are 25° and 24° and the cohesions are 0.13 and 0.09 MPa, respectively. The cohesion, friction angle and K_s of all specimens are summarized in Table 4.1. Note that application of vaseline on the smooth saw-cut surface slightly reduces the frictional resistance of the surface.

- The results show that the three-point bending tensile strengths decrease when the t/L ratios decrease, and tensile strength increases with increasing loading rate. The tensile strains decrease with increasing loading rate. The stresses-strains and stresses-deflections relations are nonlinear, particularly under the low loading rates. The specimens with high t/L ratio (0.25) show higher tensile strengths at failure than those with lower t/L ratio (0.05) due to the effect of the joint spacing and joint properties (roughness, K_s) This holds true for all loading rates.

- The elastic moduli increase with increasing t/L ratios and loading rate. This is true for both surface conditions. The results obtained from tension-induced fractures show the higher elastic modulus than those of the smooth and smooth-slip surfaces. This is probably due to the difference of the friction at the interfaces. The intact rock specimen shows the highest elastic moduli.

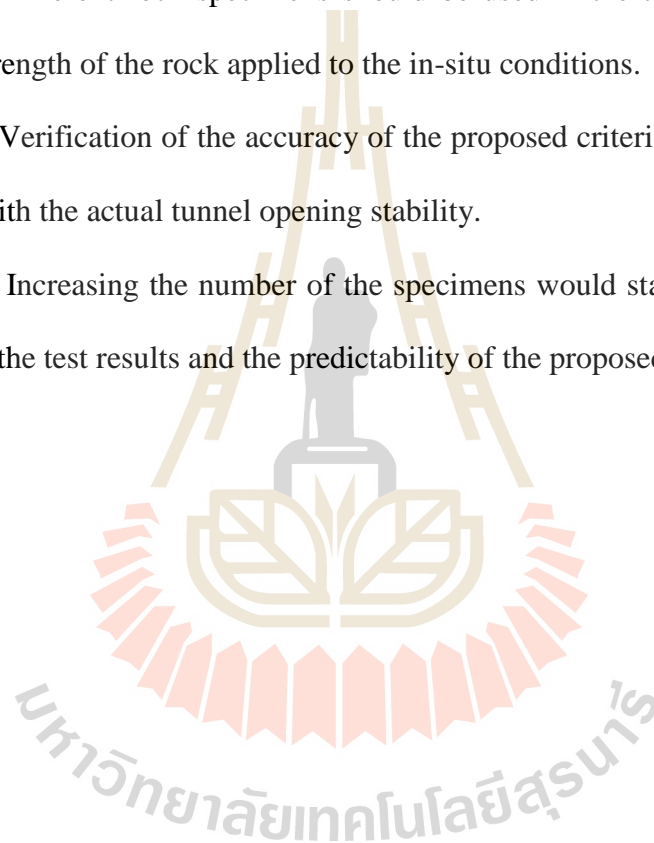
- The beam deflection can be correlated with the test results. It can be measured in the actual opening more easily than the tensile strain at the center of the roof.

- The strain energy criterion can be used to assess the actual stratified roof stability. Rock bolts may be installed to increase the t/L , and hence increases the stability of the roof beams.

7.3 Recommendations for future studies

Recognizing that the numbers of the specimens and the test parameters used here are limited, more testing and measurements are recommended, as follows:

- (1) Larger specimen size should be used to enhance the representativeness of the test results.
- (2) Different rock specimens should be used in the test to assess the rate-dependent strength of the rock applied to the in-situ conditions.
- (3) Verification of the accuracy of the proposed criterion should be made by comparing with the actual tunnel opening stability.
- (4) Increasing the number of the specimens would statistically enhance the reliability of the test results and the predictability of the proposed strength criterion.



REFERENCES

- Agapito, J.F.T. and Gilbride, L.J. (2002). Horizontal stresses as indicators of roof stability. **SME Annual Meeting**, Phoenix, Arizona.
- Agioutantis, Z., Kaklis, K., Mavrigiannakis, S., Verigakis, M., Vallianatos, F. and Saltas, V. (2015). Potential of acoustic emissions from three point bending tests as rock failure precursors. **International Journal of Mining Science and Technology**, 26: 155–160.
- ASTM C1550–10. Standard test method for flexural toughness of fiber reinforced concrete (using centrally loaded round panel). **Annual Book of ASTM Standards**, American Society for Testing and Materials, West Conshohocken, P.A., Vol. 04.08.
- ASTM C293–02. Standard test method for flexural strength of concrete (Using simple beam with center-point loading). **Annual Book of ASTM Standards**, American Society for Testing and Materials, West Conshohocken, P.A., Vol. 04.08.
- ASTM D5607-08. Standard test method for performing laboratory direct shear strength tests of rock specimens under constant normal force. **Annual Book of ASTM Standards**, Vol. 04.08. West Conshohocken, PA: American Society for Testing and Materials.
- ASTM D6272–10. Standard test method for flexural properties of unreinforced and reinforced plastics and electrical insulating materials by four-point bending. **Annual Book of ASTM Standards**, American Society for Testing and

Materials, West Conshohocken, P.A., Vol. 04.08.

Barton, N.R. (1973). Review of a new shear strength criterion for rock joint deformation. **Engineering Geology** 7: 287-332.

Bucky, P.B. and Taborelli, R.V. (1938). Effects of immediate roof thickness in long wall mining as determined by barodynamic experiments. **Transactions of the American Institute of Mining and Metallurgical Engineers**, 130: 314–32.

Chokchai, B. and Fuenkajorn, K. (2013). Effects of loading rate on joint shear strength in sandstones. **Proceedings of the Fourth Thailand Symposium on Rock Mechanics**, 24-25 January, Nakhon Ratchasima, Thailand, pp. 203–212.

Claesson, J. and Bohloli, B. (2002). Brazilian test: stress field and tensile strength of anisotropic rocks using an analytical solution. **International Journal of Rock Mechanics and Mining Sciences**, 39: 991–1004.

Evans, W.H. (1941). The strength of undermined strata. **Transactions of the Institution of Mining and Metallurgy**, 50: 475–532.

Exadaktylos, G.E., Vardoulakis, I. and Kourkoulis, S.K. (2001). Influence of nonlinearity and double elasticity on flexure of rock beams — II. Characterization of Dionysos marble. **International Journal of Solids and Structures**, 38: 4119–4145.

Fuenkajorn, K. and Daemen, J.J.K. (1986). Shape effect on ring test tensile strength. **Proceedings of the 27th U.S. Symposium on Rock Mechanics**, June 23-25, Tuscaloosa, Alabama, pp. 155–163.

Hatzor, Y.H. and Benary, R. (1998). The stability of a laminated Voussoir beam: back analysis of a historic roof collapse using DDA. **International Journal of Rock Mechanics and Mining Sciences**, 165–181.

- Jaeger, J.C., Cook, N.G.W. and Zimmerman, R.W. (2007). **Fundamentals of Rock Mechanics**, 4th edition, Blackwell publishing, Oxford.
- Klanphumeesri, S. and Fuenkajorn, K. (2010). Laboratory determination of direct tensile strength and deformability of intact rocks. **ASTM Geotechnical Testing Journal**, 34(1): 1–6.
- Liao, J.J., Yang, M.T. and Hsieh, H.Y. (1997). Direct tensile behavior of a transversely isotropic rock. **International Journal of Rock Mechanics and Mining Sciences**, 34(5): 831–849.
- Lorig, L.J. and Brady, B.H.G. (1983). An improved procedure for excavation design in stratified rock. **Proceedings of the 24th U.S. Symposium on Rock Mechanics**, 20-23 June, College Station, Texas, pp. 577–85.
- Maleki, H. and Owens, J. (1998). Analysis of interaction between mobile roof supports and mine strata. **Proceedings of the Fifth South American Congress on Rock Mechanics and Second Brazilian Conference in Rock Mechanics-SAR Rocks**, pp. 287–393.
- Morrell, R. (1998). Biaxial flexural strength testing of ceramic materials. **A natural measurement good practice guide No. 12**. Department for Innovation, Universities and Skills, UK.
- Obert, L. and Duvall, W.I. (1967). **Rock Mechanics and the Design of Structures in Rock**. John Wiley and Sons, pp. 649.
- Phueakphum, D., Fuenkajorn, K. and Walsri, C. (2013). Effects of intermediate principle stress on tensile strength of rocks. **International Journal of Fracture**, 181: 163–175.

- Pytel, A. and Kiusalass, J. (2001). **Mechanics of Materials**. 2nd edition, Cengage Learning EMEA, United States of America.
- Shabanimshcool, M. and Li, C.C. (2015). Analytical approaches for studying the stability of laminated roof strata. **International Journal of Rock mechanics and Mining Sciences**, 79: 99–108.
- Shen, G. and Zhang, D. (2016). Analysis of tunnel deformation under highly weathered sandstone strata by shallow tunneling method. **The Electronic Journal of Geotechnical Engineering**, 21: 3773–3783.
- Snyder, V.W. (1983). Analysis of beam building using fully grouted roof bolts. **Proceedings of the International Symposium on Rock Bolting**, Abisko, Sweden, pp. 187–194.
- Sterling, R.L. (1980). The ultimate load behaviour of laterally constrained rock beams. The State of the Art in Rock Mechanics. **Proceedings of the 21st U.S. Symposium on Rock Mechanics**, Rolla (ed. D. A. Summers), University of Missouri: Rolla, pp. 533–542.
- Stimpson, B. and Ahmed, M. (1992). Failure of a linear Voussoir arch: a laboratory and numerical study. **Canadian Geotechnical Journal**, 29: 188–194.
- Suanprom, P., Obcheoy, J. and Fuenkajorn, K. (2009). Permeability of rock fractures under shear stresses. **EIT-JSCE Joint International Symposium Geotechnical Infrastructure Asset Management**, Bangkok. Thailand.
- Ugural, A.C. (1999). **Stresses in Plates and Shells**, 2nd edition, WCB/McGraw Hill, Boston.

- Wisetsaen, S., Walsri, C. and Fuenkajorn, K. (2015). Effects of loading rate and temperature on tensile strength and deformation of rock salt. **International Journal of Rock Mechanics and Mining Sciences**, 73: 10–14.
- Yan, H., He, F., Yang, T., Li, L., Zhang, S. and Zhang, J. (2016). The mechanism of bedding separation in roof strata overlying a roadway within a thick coal seam: A case study from the Pingshuo Coalfield, China. **Engineering Failure Analysis**, 62: 75–92.
- Yang, H., Jiang, X., Wen, C. and Yin, J. (2013). Modeling the deformation of tunnel excavations in layered rock masses. **The Electronic Journal of Geotechnical Engineering**, 18: 723–734.
- Yeung, M.R. and Goodman, R.E. (1995). Multi-block stability analysis using the DDA method. **Proceedings of the Conference on Fractures and Jointed Rock Masses**, Lake Tahoe, CA, pp. 701–707.
- Yokoyama, T.A. (1988). A microcomputer-aided four-point test system for determining uniaxial stress-strain curves. **Journal of Testing and Evaluation**, 16: 198–204.
- Zhang, X. and Wong, L.N.Y. (2014). Choosing a proper loading rate for bonded-particle model of intact rock. **International Journal of Fracture**, 189(2): 163–179.

BIOGRAPHY

Mr. Surasak Chanpen was born on August 31, 1992 in Bangkok, Thailand. He received his Bachelor's Degree in Engineering (Geological Engineering) from Suranaree University of Technology in 2016. For he post-graduate, she continued to study with a Master's degree in the Geological Engineering Program, Institute of Engineering, Suranaree university of Technology. During graduation, 2016-2018, He was a part time worker in position of research assistant at the Geomechanics Research Unit, Institute of Engineering, Suranaree University of Technology.

